UC Irvine
UC Irvine Electronic Theses and Dissertations

Title

Development of an ultrafast integrated IVUS-OCT system and catheter for in vivo applications

Permalink

https://escholarship.org/uc/item/5tq238ch

Author

Li, Jiawen

Publication Date

2015

Peer reviewed|Thesis/dissertation

UNIVERSITY OF CALIFORNIA

IRVINE

Development of an ultrafast integrated IVUS-OCT system and catheter for in vivo

applications

Dissertation

Submitted in partial satisfaction of the requirements

for the degree of

DOCTOR OF PHILOSOPHY

in Biomedical Engineering

by

Jiawen Li

Dissertation Committee:

Professor Zhongping Chen, Chair

Professor William C. Tang

Professor Matthew Brenner

2015

TABLE OF CONTENTS

LIST OF FIGURES

LIST OF TABLES

TABLE OF ABBREVIATION

OCT	Optical coherence tomography
US	Ultrasound
TCFA	Thin cap fibroatheroma
CT	Computed tomography
MRI	Magnetic resonance imaging
IVUS	Intravascular ultrasound
TDOCT	Time domain optical coherence tomography
FDOCT	Fourier domain optical coherence tomography
SSOCT	Swept source optical coherence tomography
OFDI	Optical frequency-domain imaging
SDOCT	Spectrometer based optical coherence tomography
ID	Inner diameter
FFT	Fast Fourier Transform
2-D	Two-dimensional
3-D	Three-dimensional
MZI	Mach-Zehnder interferometer
GRIN	Gradient refractive index
PFC	Perfluorodecarbon
FWHM	Full width at half maximum
VSCEL	Vertical-cavity surface-emitting laser
FFPI	Fiber Fabry-Perot filter
SNR	Signal to noise ratio
ATR-FTIR	Attenuated Total Reflection Fourier transform infrared spectroscopy
NURD	Nonuniform rotational distortion
LDPE	Low Density Polyethylene

HDPE	High density Polyethylene
VV	Vasa vasorum
fps	frames per second
ERCP	endoscopic retrograde cholangiopancreatography
CCA	cholangiocarcinoma

ACKNOWLEDGEMENTS

I would like to express my deepest gratitude to my advisor Dr. Zhongping Chen. He gave me the great opportunity to join his world-famous lab when I was just a novice in OCT field. He trusted me and gave me the chance to work on the amazing project of integrating OCT with IVUS. He taught me to think outside of the box. He always encourages me to push the limit and never give up. Several designs described in this dissertation were first thought to be impossible, but Dr. Chen inspired me to keep trying and helped me find outside resources. Apart from guidance in engineering designs, he also supported me to bravely submit the FDA application and publish my results in high-profile medical journals to make this work more impactful. All in all, this work could not have been possible without his visionary guidance and constant support.

I would also like to thank my committee members, Professor William Tang and Professor Matthew Brenner for their insightful guidance through my PhD. Annual meetings with Prof. Tang directed me to work efficiently and keep on top of my projects. Medical and chemical suggestions from Prof. Brenner are always very informative and useful.

I thank Professor Bruce Tromberg for constantly encouraging me and challenging me to be even better in my research and also on the basketball court. I thank my collaborators Professor Pranav Patel and Dr. Dilbahar Mohar from the Cardiology division for their precious time and support. They have been very patient and dedicated in animal and diagnostic accuracy experiments. I thank Mr. Earl Steward for being so helpful and supportive. Dr. Jun Zhang deserves my thanks for his valuable guidance and discussion. I thank my collaborators Dr. Xiang Li and Dr. Teng Ma from the University of Southern California. It has been a great pleasure working with them. I

thank Dr. Youxin Mao from National Research Council, Canada, for her guidance in making ball lenses.

I appreciate the help and continuous encouragement of Mr. Michael Dhuy in the willed body program. He helped me collect artery samples and tried his best to find samples with vulnerable plaques for me. He has been a great collaborator and friend.

I thank Dr. Sari Mahon, Ms. Laurie Newman, Mr. David Mukai, Ms. Tanya Burney and Mr. David Yoon for their help with rabbit experiments. I thank Ms. Leacky Liaw and Ms. Linda Li for their kindness and help with histology.

I enjoy working in the amazing OCT lab. I enjoy discussing with and learning from my supportive colleagues. I thank Danny and Emon for teaching me mechanical design and Solidworks. I thank Joe and Youmin for their help in C++ coding. I thank Dr. Jiang Zhu, Dr. Yongzhao Du and Dr. Shenghai Huang for their discussions of Doppler OCT and medical applications of OCT. I thank my supportive friends, Dr. Shanshan Liang, Dr. Wenjuan Qi, Dr. Rui Li, Dr. Yongzhao Du, Rachel Qu and Zhonglie, Dr.Zhuqing Zhu, Dr. Xiangqun Xu, Dr. Cuixia Dai in the OCT lab.

Finally, I would like to give my thanks to my selfless parents and caring friends. They supported me in being ambitious and optimistic, and kept me from being a workaholic.

CURRICULUM VITAE

Jiawen Li

2010   B.S., Optical Engineering, Zhejiang University, Hangzhou, China

2012   M.S., Biomedical Engineering, University of California, Irvine, U.S.A.

2015   Ph.D., Biomedical Engineering, University of California, Irvine, U.S.A.

FIELD OF STUDY

Biophotonics and Biomedical Imaging

JOURNAL PUBLICATIONS

1. **Jiawen Li**, Teng Ma, Dilbahar Mohar, et al. Ultra-fast optical-ultrasonic system and miniaturized endoscopy for volumetric imaging and characterizing atherosclerotic plaques in vivo. 2015. (Under review).

2. **Jiawen Li**, Hataka Minami, Earl Steward, et al. Optimal flushing agents for integrated optical acoustic imaging systems. Journal of Biomedical Optics. 2015, 20(5): 56005.

3. **Jiawen Li**, Xiang Li, Dilbahar Mohar, et al. Integrated IVUS-OCT for real-time imaging of coronary atherosclerosis. Journal of the American college of cardiology Imaging, 2014, 7(1): 101-103. (Impact factor: 6.986)

4. **Jiawen Li**, Teng Ma, Joseph Jing, et al. Miniature optical coherence tomography-ultrasound probe for automatically co-registered three-dimensional intracoronary imaging with real-time display, 2013, 18(10): 100502. (A featured paper reported by OCT news)

5. **Co-first author paper:** Xiang Li, **Jiawen Li**, Joe Jing, Teng Ma, Shanshan Liang, et al. Integrated IVUS-OCT Imaging for Atherosclerotic Plaque Characterization. IEEE Journal of Selected Topics in Quantum Electronic. 2014, 20(2): 7100108.

6. **Co-first author paper:** Teng Ma, **Jiawen Li**, Adrian Correa, Dilbahar Mohar, Hataka Minami, et al. Diagnostic Accuracy of an Integrated Intravascular Ultrasound and Optical Coherence Tomography (IVUS-OCT) System for Human Coronary Plaque Characterization. 2015. (Under review)

7. Zhonglie Piao, Teng Ma, **Jiawen Li**, et al, High speed intravascular photoacoustic imaging with fast OPO laser at 1.7 μm, Applied Physics Letters. 2015. (Accepted)

8. Teng Ma, Mingyue Yu, **Jiawen Li**, Chelsea E. Munding, Zeyu Chen, et al, Multi-Frequency Intravascular Ultrasound (IVUS) Imaging, IEEE Transactions on Ultrasonics, Ferroelectrics, and Frequency Control. 2015, 62(1): 97-107.

9. Shanshan Liang, Teng Ma, Joseph Jing, Xiang Li, **Jiawen Li**, et al. Trimodality imaging system and intravascular endoscopic probe: combined optical coherence tomography, fluorescence imaging and ultrasound imaging, Optics Letter. 2014, 39(23): 6652-6655.

10. Wenjuan Qi, Rui Li, Teng Ma, **Jiawen Li**, Kirk K. Shung et al. Resonant Acoustic Radiation Force Optical Coherence Elastography, Applied Physics Letters. 2013, 103(10): 103704. (A featured paper reported by OSA news)

11. Shanshan Liang, Arya Saidi, Joe Jing, Gangjun Liu, **Jiawen Li**, et al. Intravascular atherosclerotic imaging with a combined fluorescence and OCT probe based on a DCF combiner. Journal of Biomedical Optics. 2012, 17(7): 070501.

12. Jiechen Yin, Xiang Li, Joe Jing, **Jiawen Li**, David Mukai, et al. Novel miniature optical coherence tomography (OCT) - ultrasound (US) probe and integrated imaging system. Journal of Biomedical Optics letter. 2011, 16(6):060505.

13. Jie Meng, Zhihua Ding, **Jiawen Li**, Kai Wang, Tong Wu. Transit-time analysis based on delay-encoded beam shape for velocity vector quantification by spectral-domain Doppler optical coherence tomography. Optics Express. 2010, 18(2).

ABSTRACT OF THE DISSERTATION

Development of an ultrafast integrated IVUS-OCT system and catheter for in vivo

applications

by

Jiawen Li

Doctor of Philosophy in Biomedical Engineering

University of California, Irvine, 2015

Professor Zhongping Chen, Chair

This research focuses on the development and use of an ultrafast integrated IVUS-OCT system to image and identify vulnerable atherosclerotic plaque in vivo. By providing ultrafast imaging of arteries with high resolution and deep penetration depth simultaneously, this hybrid IVUS-OCT technology opens new and safe opportunities to evaluate in real-time the risk of plaques, identify vulnerable plaques, and optimize treatment decisions.

A system to simultaneously provide IVUS and OCT functions at an imaging speed of over 30 frames per second was thought to be impossible. In this dissertation, we overcame the speed limit of integrated IVUS-OCT system, the fundamental barrier hindering the clinical application of the integrated IVUS-OCT technique. We demonstrated the ability to perform simultaneous IVUS-OCT imaging at 72 frames per second safely in vivo. By using this ultrafast system, the risk of catheter-induced spasm and a great amount of toxic contrast agent is significantly reduced. This breakthrough enables the translation of this technology into clinical practice.

Nine atherosclerotic-model rabbits and four swine were imaged to validate the design of our imaging system and catheters. Images were obtained in these animals without complications. For the first time, this study shows that an integrated intracoronary IVUS-OCT system is feasible and safe to use in vivo to detect atherosclerotic plaques. To avoid severe side effects of contrast agents, alternative IVUS-OCT flushing agents were investigated. Ex vivo imaging of over 300 human coronary artery regions of interest was also performed to quantitatively evaluate the diagnostic accuracy of the integrated system. The in vivo animal imaging and ex vivo human cadaver diagnostic accuracy test elucidated that this technique can facilitate a more powerful tool to explore the development of plaques and holds great hope for a more accurate assessment of vulnerable plaque in patients.

In addition, other applications of the integrated IVUS-OCT system were also explored. Ex vivo studies were performed to image stent and bile duct cancer.

Last but not least, a new probe design for tracking the trajectory of the imaging catheter while perform imaging, was developed and tested in porcine trachea ex vivo.

Chapter 1

Introduction

1.1 Atherosclerosis and its imaging

Heart attack is a major cause of death in developed countries. In the United States alone, 1.2 million individuals suffer from heart attacks every year. A quarter of them die before reaching a hospital. With an aging population, these numbers are still increasing. Heart attacks are mainly due to rupturing of a vulnerable atherosclerotic plaque (86%) in a coronary artery (1).

Atherosclerosis is a condition where fatty streaks (plaques) develop in the inner layer of an artery wall, narrowing the lumen of an artery. When these plaques rupture, they may block the blood vessel. When this happens to the coronary artery, heart attack will take place. Atherosclerosis does not only affect coronary artery: the entire artery tree is vulnerable to atherosclerotic plaque. When the same process happens in cerebral arteries, it may lead to stroke. And if plaques are built in peripheral arteries, it is called Peripheral Artery Diseases (PAD).

Pathologists revealed the etiology of acute coronary syndromes (ACS) (2). It was found that 55%-60% of thrombi were caused by plaque rupture, 30%-35% by plaque erosion and 2%-7% by calcified nodules. Interestingly, the influence of age and gender was very significant: Plaque erosion happened mostly in patients younger than 50 years and in premenopausal women; whereas plaque rupture happened mostly in women older than 50 years and in men at all ages, though with their relative decreasing incidence with age. Figure 1 shows the progression of atherosclerotic plaque, where plaque rupture is shown in stage 5, erosion in stage 7 and calcification in stage 6.
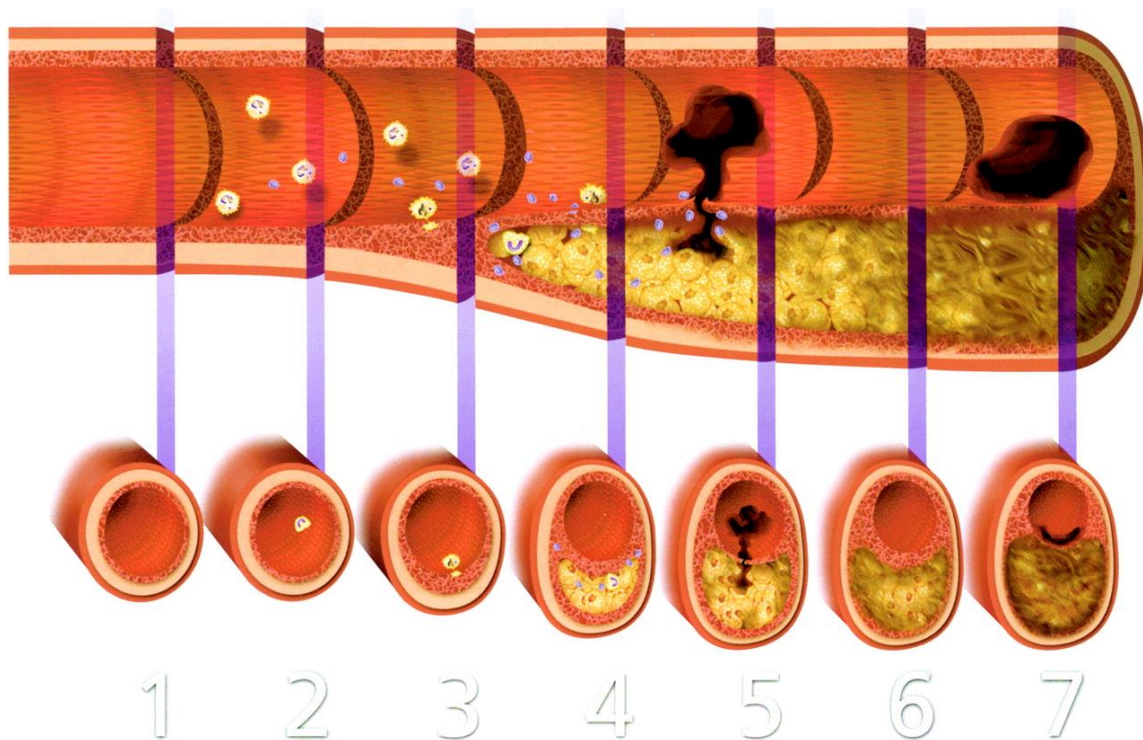
Figure 1 The progression of atherosclerosis. Top, longitudinal section of artery demonstrating the natural history of atherosclerosis, from normal artery to one with advanced atherosclerotic plaque. Bottom, cross section of artery at each stage of atherosclerosis evolution. 1. Normal artery. 2. initial stage of atherosclerosis, staring with a lesion in endothelial cells and accumulating extracellular lipid in intima. 3. Lipid in intima initializes the recruitment of monocytes became macrophages. Lipid-rich foam cells and cholesterol clefts can be seen. 4. Cap of the plaque becomes thinner and thinner as the lesion progress and tissue factor expresses. 5. At one point, plaque ruptures, causing thrombi. 6. Thrombin and mediator release and healing process starts. More collagen and smooth muscle cell grows inside plaque. Lipid plaque transform to fibrous and often calcified plaque. 7. Superficial erosion of endothelium can also cause occlusive thrombi. (3)

Advanced atherosclerosis patients, with secondary changes in the structure or function of the heart, can be simply diagnosed by "cardiac stress testing" or more accurately diagnosed by Magnetic Resonance Imaging (MRI) (4). However, early diagnosis can rely on non-invasive imaging and physiologic tests (blood pressure or chemical indicator in blood).

The intima-media thickness of carotid arteries (Ultrasound, US) and the calcium score of coronary arteries (Computed Tomography, CT) are the two commonly used non-invasive

imaging indicators applied to early detection of atherosclerosis in a large population. First, carotid arteries are located close to the skin. US imaging, with 1-10 cm penetration depth, is well-suited to image these superficial arteries. Also, the sub-mm resolution ability of ultrasound enables the differentiation between intima and media layers. Plaques grow in and thicken intima layers. The intima-media thickness is an indicator of atherosclerosis risk (5). Second, CT technology, with its high penetration depth, makes non-invasive imaging of coronary arteries (deep arteries) possible. The calcium absorption of X-ray in calcified plaques is a good contrast source for CT diagnosis. The calcium score can be an indicator for early diagnosis and risk assessment of atherosclerosis (6).

Table 1 Comparison of coronary imaging modalities

	Angiography	MRI	IVUS	IV-OCT
Resolution(μm)	100~200	100~300	80~200	5~15
Invasive	No	No	Yes	Yes
Ionizing radiation	Yes	No	No	No
Artery wall imaging	No	No	Yes	Yes
Other	Flow only	N/A	N/A	Plaque character

However, none of the above diagnostic technologies are suitable for diagnosis of vulnerable atherosclerotic plaques in a coronary artery, because of their limited resolutions. Only invasive technologies, i.e., intravascular ultrasound (IVUS) and intravascular optical coherence tomography (OCT), permit visualization of coronary artery walls. This is critical for the risk assessment of plaques. Not all plaques are prone to rupture. Indeed, a vulnerable plaque, or to

say a high risk plaque, is characterized as a lipid necrotic core with a thin fibrous cap (7) (also

see Fig. 1 stages 4 and 5). On the other hand, imaging of coronary artery walls provides

information not only for diagnosis (risk assessment of plaques) but also for guiding treatment,

such as stent implantations and using other devices to restore blood flow at the site of the

blockage. Comparison of coronary imaging technologies is listed in Table 1.

1.2 IVUS and OCT imaging

Pathology studies have revealed a prototypic vulnerable plaque, thin cap fibroatheroma (TCFA).

TCFA is characterized as: 1) a large necrotic and lipid pool, 2) an overlying thin fibrous cap (<

65 μm), and 3) increased macrophage activity (7). Recently, imaging technologies for analyzing

the risk of plaque ruptures have advanced quickly. However, no method to date has demonstrated

the ability to identify all of the characteristic features of TCFA (7, 8).

IVUS permits the first direct assessment for artery-wall thickening. "Positively remodeling" and

"high eccentricity" have been introduced as markers for a potential high-risk plaque (9, 10). Yet

none of these factors are optimally predictive of TCFA. More recently, spectral analysis

algorithms of IVUS signal were conducted to construct virtual histologic maps according to

different major components in tissues (11-13). The most well-known one is IVUS-virtual

histology (IVUS-VH). Four colors are used for differentiating fibrous, fibrolipid, necrotic and

calcium tissue. In this method, periodograms of IVUS images are used to calculate prototypic

spectral parameters for each tissue type with the guidance of histopathology of correlated region

of interest. Recursive partitions were completed to optimize a classification tree (13). Moreover,

an IVUS-derived TCFA was later proposed based on this algorithm (14). The definition for the

IVUS-derived TCFA is a plaque with presence of necrotic core > 10% and atheroma volume >

40% without observable overlying fibrous tissue. A series of research has been reported to display the feasibility of this method and definition (15) while at the same time, questions and challenges have also been proposed (16). This method, together with other spectral analysis algorithms, such as iMap (11) and integrated backscatter IVUS (IB-IVUS) (12), are fundamentally insufficient to predict plaque-vulnerability due to the intrinsically limited resolution of IVUS.

In the meantime, IVOCT has been translated from an imaging technique to clinical use. With its superior axial (5-15 μm) and lateral resolution, OCT provides innovative insight for vulnerable plaque research. Optical scattering contrast in OCT is applied for classification of different tissue types. Low organelle density (and, thus, low reflective index fluctuation) in a lipid rich region leads to lower scatter power. Likewise, relatively uniform periodical and directional structure in a fibrous rich region leads to homogeneous higher scatter power. And the thickness of a fibrous rich region (fibrous cap) can be accurately measured relying on the high resolution of OCT. Furthermore, cells with a high macrophage density produce strong scatter signal (17). Thus, two major characteristics of TCFA can be identified by OCT. However, as a tradeoff for its high resolution, OCT is limited by poor penetration (< 1-1.5 mm in tissue) and is inadequate to measure the size of a lipid pool.

It is natural to think about comparing IVUS' and OCT's sensitivity and specificity for diagnosing TCFA. The first reported diagnostic capability research evaluated the accuracy of OCT, IVUS and IB-IVUS (18). These three methods were used to characterize calcification, fibrosis, and lipid pool in cadaver tissues. Then the results were compared with histology slides, the gold standard. The authors came to the conclusion that OCT is the best diagnostic technique if within its penetration depth. However, when a plaque is bigger than what OCT can penetrate, false

negative diagnosis may occur. On the other hand, IVUS is very sensitive to calcified plaque. Yet false negative diagnosis is caused by the limited resolution of IVUS. Later, a group in the Netherlands verified the feasibility of the combined use of separately acquired IVUS and OCT data for diagnosing vulnerable plaques in patients. The authors proposed that "the combined use of OCT and VH-IVUS might be a feasible approach for evaluating TCFA" (19). These results are confirmed by a more recent study (20) and this study proved that the combined use of OCT and IVUS can significantly improve the ability to diagnose vulnerable plaques.

However, all these previous studies were conducted by using separated IVUS and OCT catheters and offline fusion of the separated IVUS and OCT data sets. There are major limitations to these studies using offline fusion (19, 21): prior to fusion, matching OCT and IVUS lesions based on manual identification of landmarks, such as side-branches or calcification, is required. The matching procedures are not only tediously slow but also may lead to inaccurate co-registration, because lumens constantly change shape and the images acquired may not be identical at different points in time within each cardiac cycle. They cannot be used for real-time display either, severely limiting clinical utility for guiding interventions during a catheterization procedure. The ability to fully integrate OCT and IVUS capabilities into a single imaging system for in vivo assessment of plaques (7, 21) will help overcome these limitations. Fully-integrated techniques are also less time consuming, less traumatic, provide less radiation exposure, use fewer contrast agents, and provide more accurate imaging capabilities with the potential for a real-time fusion image display.

Therefore, it is critical to have a fully integrated IVUS-OCT for detection of vulnerable plaques and optimization of treatment decisions.

1.3 Summary of chapters

The aim of this thesis is to develop a fully integrated IVUS-OCT system for in vivo applications and to pave the way for its clinical utility.

Chapter 1 introduces atherosclerosis and its common diagnostic methods.

Chapter 2 summarizes the principle of OCT, especially the SNR of the OCT system.

Chapter 3 concerns the development of an SSOCT system, an SDOCT system and an ultrafast integrated IVUS-OCT system for intravascular imaging of atherosclerosis. Because an SSOCT system can be built more compactly and can image faster than SDOCT system, SSOCT design was selected to make the integrated IVUS-OCT system. Using the SSOCT and IVUS sub-systems, we further developed ultrafast IVUS-OCT systems. In 2012, the frame rate of the imaging system was achieved to 20 fps. In 2015, the frame rate of the imaging system is now achieved to 72 fps.

Chapter 4 introduces an intravascular imaging catheter design. A good catheter design is needed to achieve the goal of safe intracoronary imaging in vivo. Several challenges to catheter designs (such as mechanical, dimensional, biocompatible, and adaptable to clinical workflow) have been overcome in this process, which is described in this chapter. Two designs for a miniature IVUS-OCT imaging probe, sequential and back-to-back, were developed. A catheter that satisfies the requirements of clinical procedures was also developed.

Chapter 5 shows the in vivo imaging results obtained using this IVUS-OCT system and catheter. Optimal IVUS-OCT flushing agents were first studied, so as to maintain good image quality in vivo while inducing least toxicity to animals. In vivo IVUS-OCT imaging of thick cap

fibroatheromas in rabbit models, and as well as of swine coronary arteries, was achieved safely and successfully.

Following the success of animal experiments, we started to prepare for a pilot human study. The first and foremost challenge to our human experiments is to get FDA approval for using the investigational IVUS-OCT device we developed in humans. **Chapter 6** summarizes the testing and risk management we conducted in preparation for the FDA-IDE application.

Meanwhile, the effectiveness of a newly developed imaging system needed to be validated using a large sample set. **Chapter 7** elucidates the statistical analysis of the usefulness of the integrated IVUS-OCT system. Over 240 regions of plaques were imaged by this system. It was concluded that the use of IVUS and OCT was superior to IVUS-only and OCT-only diagnosis for detection and characterization of coronary atherosclerotic plaques. IVUS-OCT showed a high degree of sensitivity and specificity.

The application of an IVUS-OCT system is not limited to atherosclerotic plaque detection. **Chapter 8** summarizes preliminary results of other applications we achieved using the IVUS-OCT system. We clearly imaged stents and tumors.

Chapter 9 introduces a novel probe design to address a general problem of 3D reconstruction of OCT datasets. Most 3D reconstruction of 2D image sets is done under the assumption that probe trajectory is a straight line. The lack of probe trajectory information has limited our ability to render 2D images to true 3D anatomy. The beam-splitter probe, described in this chapter, can automatically track the probe trajectory while performing imaging. We demonstrated the feasibility of the design using a porcine trachea specimen.

Chapter 2

Principle of optical coherence tomography

2.1 Principle of optical coherence tomography

OCT measures the time delay of the reflected echo signal, similar to the principle of ultrasound. Since light transfers around one million times faster than sound and cannot be directly detected, interference is used to measure light reflection, as shown in Figure 1. The amplitude of the interference signal can be expressed as: $I(z) = 2I(1 + \cos\frac{4\pi z}{\lambda})$, where z is the path length difference between the sample and reference arms, I is the intensity and λ is the wavelength of the incident light. We can calculate the location of the reflector by demodulating the amplitude of reference signal.

For low coherence laser source, the constructive interference is only achieved within a certain region (Figure 2 bottom right inset) called coherence length

$$L_c = \frac{2\ln 2}{\pi} \frac{\lambda^2}{n_s \Delta\lambda} = 0.44 \frac{\lambda^2}{n_s \Delta\lambda} \tag{2-1}$$

Where n_s is the index of refraction of the sample and $\Delta\lambda$ is the full-width-at-half-maximum of spectral bandwidth. The coherence length is the full-width at half-maximum (FWHM) of the interference fringe envelope. This length is the theoretical axial resolution of any OCT system with a Gaussian spectrum. For a laser source with given FWHM, the Gaussian spectrum can provide the best resolution because its reduction of side lopes (22).

9

$$I(x) = 2I_0(1 + \cos\frac{4\pi x}{\lambda_0})$$

$$R_{axial} = L_c = 0.44\left(\frac{\lambda^2}{\Delta\lambda}\right)$$
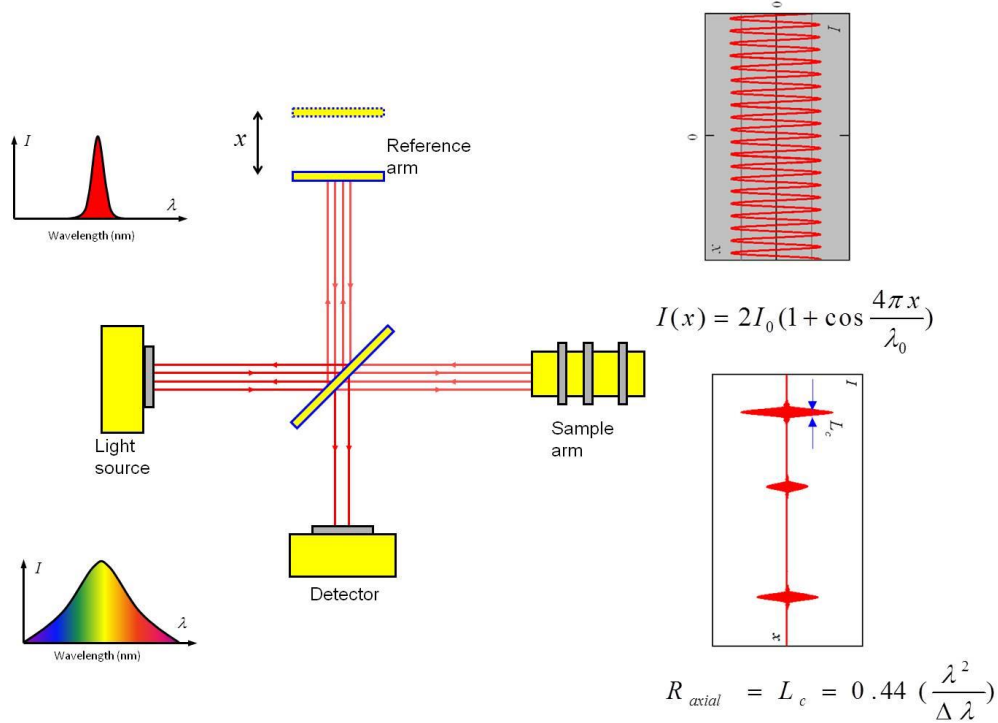
Figure 2 Schematic of Michelson interferometer and principle of OCT. When the light source is Quasi-monochromatic (top left inset), light coming back from reference arm interferences with back-scattered from sample arm at all depth. The detected signal is shown in the top right inset. When the light source is broad band low time-coherent light source (bottom left inset), noticeable interference is not always generated. The interference fringes are observed only when optical path lengths are matched within the coherence length of the source (bottom right inset).

The lateral resolution of OCT system is determined by the F number of the focusing lens. $\Delta x = 4\frac{\lambda F\#}{\pi} = 4\frac{\lambda f}{\pi D}$, where f is the focal length of the lens and D is the beam spot. The bigger the F number of the focusing lens is, the better the resolution. In an example of high resolution OCT, the Micro OCT (23) , a lens with 0.12 N.A and annularly apodized design was used to achieve 2 μm lateral resolution.

In Time domain OCT, scanning is achieved by moving the reference mirror (Figure 2). The A-line speed is limited by the mechanical scanning speed of the reference mirror. Mechanical scanning cannot exceed 20 kHz. Fourier domain OCT (FDOCT) was proposed to overcome this

limitation. In FDOCT, the depth scan is calculated by a Fourier transform of the acquired spectra. The principle and development of FDOCT is in Chapter 3.

2.2 The signal and noise of OCT system

There are three major sources of noise in OCT system: thermal noise of the detector, shot noise and relative intensity noise. Thermal noise-- also called Johnson noise -- is independent of power. The cooler the detector is, the smaller this noise is. The shot noise is caused by the discrete nature of electric charges. The more the number of electric charge (N), the higher the noise. The SNR of shot noise is $\sqrt{N}$. Thus, the noise current is approximately the square root of the power,

$i = q\sqrt{\dfrac{(P_r + P_s)}{h\nu}}$, where P_s and P_r are the power of sample arm and reference arm, q is the elementary electric charge, h is the Planck's constant, $h\nu$ is the energy of single photon and ν is the frequency of the photon, given by c/λ.

Considering the sensitivity of detector η, the power of the shot noise can be expressed as

$$P_{shot} = \eta q^2 \frac{(P_r + P_s)}{h\nu} \tag{2-2}$$

As for the relative intensity noise, it is caused by the fluctuation of the laser source, including the cavity vibration and fluctuation in the gain medium. Its power is proportional to the square of the signal power.

$$P_{RIN} = \left(\frac{\eta q}{h\nu}\right)^2 RIN(P_r + P_s)^2 \tag{2-3}$$

By considering the bandwidth of the detection BW, we can get the well-known expression for the noise power $\langle i_n^2(t) \rangle$ in OCT system

$$\langle i_n^2(t) \rangle = (i_{th}^2 + 2\eta q^2 \frac{(P_r + P_s)}{hv} + \left(\frac{\eta q}{hv}\right)^2 RIN(P_r + P_s)^2)BW \qquad (2\text{-}4)$$

The signal OCT system obtained can be expressed as

$$i_s(t) = \frac{\eta q}{hv}(P_r + P_o \int r^2(z)d(z) + 2\sqrt{P_o P_r} \int r(z)\Gamma(z)\cos(2k(t)z + \phi(z))dz) \qquad (2\text{-}5)$$

Where r(z) is reflectance power profile of the sample and $\Gamma(x)$ is the coherence function of the instantaneous laser output. P_o is the power illuminating the sample. $P_s = r^2 P_o$, where r^2 is the reflectivity of a reflector at $z=z_o$. In the phase term $\cos(2k(t)z + \phi(z))$, factor 2 is used because of the two way path length distance, coming and going. The k (t) is the resampling of k with same distance interval of t, more information about this is in chapter 3.1.2.

Note: only the third term in (2-5) is the inference signal that can be detected by the balance detector in SSOCT system.

2.3 The SNR advantages of FDOCT

To know the SNR of FDOCT, we need to know the signal and noise power in the Fourier domain.

The single current is given by:

$$i_s(t) = \frac{\eta q}{hv}(P_r + P_o \int r^2(z)d(z) + 2\sqrt{P_o P_r} \int r(z)\Gamma(z)\cos(2k(t)z + \phi(z))dz) \qquad (2\text{-}6)$$

12

Thus the power of the Fourier transform of the signal $\left|F_s(z_0)\right|^2$ equals to $N_s^2/2(i_s)^2$. The factor ½ is used because we use only the positive and negative frequency components of the signal after the Fourier transform. In TDOCT, only the reflector which matches with reference arm path length generates constructive interference. However all reflectors within the image depth generate constructive interference in FDOCT. Thus, the signals of FDOCT is N_s time higher than $(i_s)^2$, the signals of TDOCT. More signals are acquired in FDOCT than TDOCT per unit time.

The noise power can be calculated by the Parseval's theorem: the sum of the square of a function is equal to the sum of the square of its Fourier transform $\sum F_n^2 = N_s \sum i_n^2$. Thus,

$$SNR_{FDOCT} = \frac{\left|F_s(z_o)\right|^2}{\left\langle F_n^2 \right\rangle} = \frac{N_s}{2} SNR_{TDOCT} \tag{2-7}$$

where

$$SNR_{TDOCT} = \frac{\left\langle i_s^2(t) \right\rangle}{\left\langle i_n^2(t) \right\rangle} \tag{2-8}$$

The formula above (2-7) illustrates the principle and the important concept of SNR advantages in FDOCT.

However, the formula above does not provide much guidance for practical use. In practice, SNR in a SSOCT system (with a balance detector, i.e, first two terms in (2-5) cannot be detected) can be estimated by the following relationship

$$SNR_{SSOCT} \approx \frac{\eta P_s}{h \nu f_A} \tag{2-9}$$

13

where f_A is the A line scanning frequency. f_A is used instead of the BW in (2-4) because some OCT laser sources have a duty cycle under 100%.

The above estimation is deduced from (2-4) (2-5) (2-7) (2-8) at the shot noise limit condition (when P_s<<P_r and first and second term in (2-4) is negligible.

Using the relationship, we can make our OCT system perform to its best by adjusting the sample power, reference power and scanning speed. Thus, if the system is scanning at a faster speed, the sample arm power needs to be higher, so as to keep the SNR constant. This idea was used when adapting the system to 50 kHz laser (discussed Chapter 3.4). As for the selection of the reference power for best SNR performance, the theoretic value can be deduced by (2-4) (2-5). But it is not easy to use in practice. A more practical technique is that increasing the reference power can increase system sensitivity until the shot noise starts to dominate. Note: OCT system is usually operated at shot noise limit mode.

2.4 Speckle

Speckle is a double-edged sword in OCT. Speckles are both signal carriers and signal degraders. Speckle can also be used for measuring flow speed (24). They are caused by the random interference between reflected waves with a given spatial and temporal coherence. The size of a speckle is determined by 1) the optical properties and motion of the target object 2) the size and temporal coherence of the light source, 3) multiple scattering and phase aberrations of the propagating beam, and 4) the aperture of the detector. Usually, the higher the resolution, the smaller speckle. Different algorithms can be used to reduce speckle (25-27).

Chapter 3

Development of Fourier domain optical coherence tomography and integrated OCT-IVUS system

FDOCT is achieved by calculating a Fourier transform from the acquired spectra. Mechanically scanning the reference arm is not necessary for an axial scan. The interference signal in the frequency domain (i.e. wavelength (k) domain) is recorded using either a frequency-swept laser source (swept source OCT, SSOCT) or a spectrometer with a high speed line-scan camera as the detector (Spectral domain OCT, SDOCT). With the development of fast swept lasers (28, 29), SSOCT is able to scan as fast as 300 kHz to 1 MHz. On the other hand, the development of SDOCT system relies on the development of cameras. Silicon based cameras for the 800 nm system are usually more advanced than the InGaAs cameras for 1310 nm system and also cost less. Thus, a SDOCT system with a center wavelength of ~800 nm is used more often than 1310 nm one. In general, SSOCT system is more compact and can image faster than SDOCT. SDOCT, on the other hand, enables better phase stability than SSOCT and often applied for Doppler phase detection. Thus, both SSOCT (see Chapter 3.1) and SDOCT (see Chapter 3.2) were researched and developed for different application during my PhD.

In Chapter 3.3, the design of our IVUS sub-system is summarized. Using the IVUS and SSOCT sub-systems, we further developed ultrafast IVUS-OCT systems (see Chapter 3.4). In 2012, the frame rate of the imaging system was achieved to 20 frames per second (fps). In 2015, we have increased the frame rate of the imaging system to 72 fps.

3.1 Swept-source optical coherence tomography

3.1.1 SSOCT system design and assembly
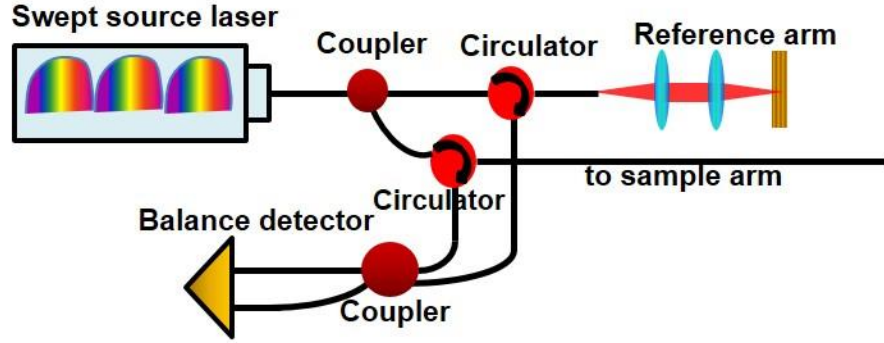
Figure 3 Schematic of SSOCT system

The schematic of our SSOCT system is depicted in Figure 3. In this design, a circulator, with low insertion loss (each port ~0.6 dB), is used to make full use of the returning signal. A balanced detector is used to compress the common mode of the detected signal. Here is the proof of the common-mode suppression:

The signal detected by the "+" side is

$$|E_r|^2 + |E_s|^2 + |E_r||E_s|\cos(kz_r + kz_s) + |E_r||E_s|\cos(kz_r - kz_s) \tag{3-1}$$

The signal detected by the "-" side is

$$|E_r|^2 + |E_s|^2 - |E_r||E_s|\cos(kz_r + kz_s) - |E_r||E_s|\cos(kz_r - kz_s) \tag{3-2}$$

The signal obtained by the balanced detector (the difference between the "+" and "-" sides) is

$$2|E_r||E_s|\cos(kz_r + kz_s) + 2|E_r||E_s|\cos(kz_r - kz_s) \tag{3-3}$$

16

Apart from designing the schematic of system, selecting of the components, designing their layout, assembling the system and testing its performance were also necessary. A photo of the SSOCT system we built is shown in Figure 4. A 1310 nm 50 kHz swept source laser (Santec Corporation, Komaki, Aichi, Japan) is used as the laser source. An 80/20 1X2 coupler is applied to split the light into the sample and the reference arms. According to formula 2-9 (SNR formula), the SNR of a system increases with an increase of sample arm power if the signal from reference arm is high enough to reach the shot-noise limit. Thus majority of the incident light (80%) is transmitted to the sample arm. Two circulators, one for the reference arm and one for the sample arm, are then applied to redirect the signal back to the detector. Three in-line polarization controllers are used to ensure the match of the polarization states for both the reference and the sample arms, thus generating constructive interference. A 50/50 2X2 is used before the balanced detector to collect signals from the sample and reference arm and deliver signals to the amplified balanced photodetector (PDB420, 75 MHz, Thorlabs Inc., Newton, New Jersey, USA).
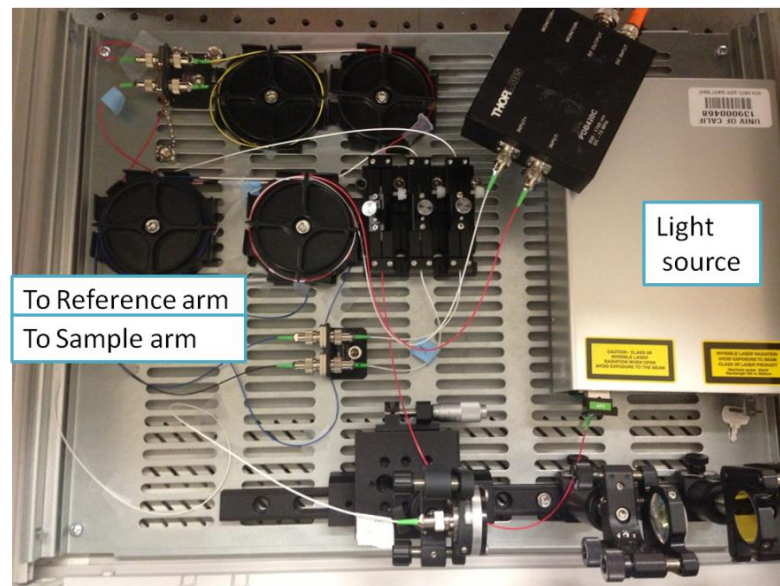
Figure 4 Photo of a fiber-based SSOCT system

3.1.2 Calibration

In a FDOCT, a Fourier transform pair of the depth z and the wavenumber k is commonly used. In each A-line, by calculating the discrete Fourier transform of current, I, corresponding to a uniform k interval, I(k), the current I as a function of each depth z can be solved. However, for our swept source OCT system, a trigger signal with a uniform time interval, initiates data acquisition from detector. That is to say, the signal we obtain is current I, corresponding to time t, that is I(t). If we compute the Fourier transform by I(t), instead of I(k), then OCT images will be deteriorated. Therefore, the relationship between k and t need to be calibrated. The process to solve the relationship between k and t, k(t), is called calibration.

Nowadays, most commercial lasers itself provides a k-clock for real-time calibration so that there is no need for software calibration. A k-clock is usually constructed using a fiber Fabry-Perot filter (FFPI) or Mach-Zehnder interferometer (MZI). The first real time calibration was proposed by Huber in 2005 (30). In this initial design, two streams of signals, sample and recalibration, are recorded simultaneously. A data point from the sample trace is only added to the calibrated signal array, if the values of the corresponding recalibration signal are higher or lower to its nearest sampling points. Thus, only sample points obtained with uniformed k interval are added to the calibrated signal array. The algorithm contains only two comparisons in one loop and does not include a complicated Fourier transform. Its processing time is negligible and this facilitates the real-time calibration. Recently, a similar method (31) was proposed for producing a k-clock in the vertical-cavity surface-emitting laser (VSCEL). A MZI was set at Nyquist sampling to generate the optical clock signal, with a constant interval of k.

However, k-clock cannot be applied in the integrated OCT-IVUS system, since IVUS requires sampling at a constant interval of time. Thus, digital calibration was used. The algorithm for calibration is demonstrated below.

The electric field of light can be written as,

$$E(t) = A\cos(k(t)z + \varphi) \tag{3-4}$$

where A is the amplitude and ϕ is the initial phase.

The electric fields from the reference arm and sample arm can be written as

$$E_R(t) = A_R \cos(k(t)z_R + \varphi_R)$$
$$E_S(t) = A_S \cos(k(t)z_S + \varphi_S) \tag{3-5}$$

Thus, the intensity of light that comes into the detector can be expressed as:

$$
\begin{aligned}
I(t) &=< (E_R + E_S)(E_R + E_S) > \\
&=< A_S^2 + A_R^2 + 2A_R A_S \cos(k(t)z_R + \varphi_R)\cos(k(t)z_S + \varphi_S) > \\
&=< A_S^2 + A_R^2 + A_R A_S \cos(k(t)z_R - k(t)z_S + \Delta\varphi) + A_R A_S \cos(k(t)z_R + k(t)z_S + \varphi_R + \varphi_S) >
\end{aligned}
\tag{3-6}
$$

where $\Delta\varphi = \varphi_R - \varphi_s$, and $<>$ means time average. After the detected signal passes through the balance-detector, only $A_R A_s \cos(k(t)z_R - k(t)z_s + \Delta\varphi)$ is left. We abbreviate $k(t)z_R - k(t)z_s + \Delta\varphi$ as Φ, then $\Delta\Phi = \Delta k(t)\Delta z + \Delta\varphi$. During calibration, we set the light path difference Δz between the sample arm and reference arm as 1mm. Since Δz is known and $\Delta\varphi$ is constant, $\Delta\Phi$ is linearly proportional to Δk. The calibration problem is simplified as solving the relationship between $\Delta\Phi$ and t. $\Delta\Phi(t)$ can be easily calculated by phase resolve methods (32).

Under the guidance of this algorithm, we can implement calibration in our system and evaluate the result by point spread function (PSF). Before calibration, the axial resolution is 17 μm. After calibration, the axial resolution is 7.8 μm in air, which is close to the theoretic resolution of 7.58 μm. The imaging difference of a mirror is demonstrated in Figure 5.
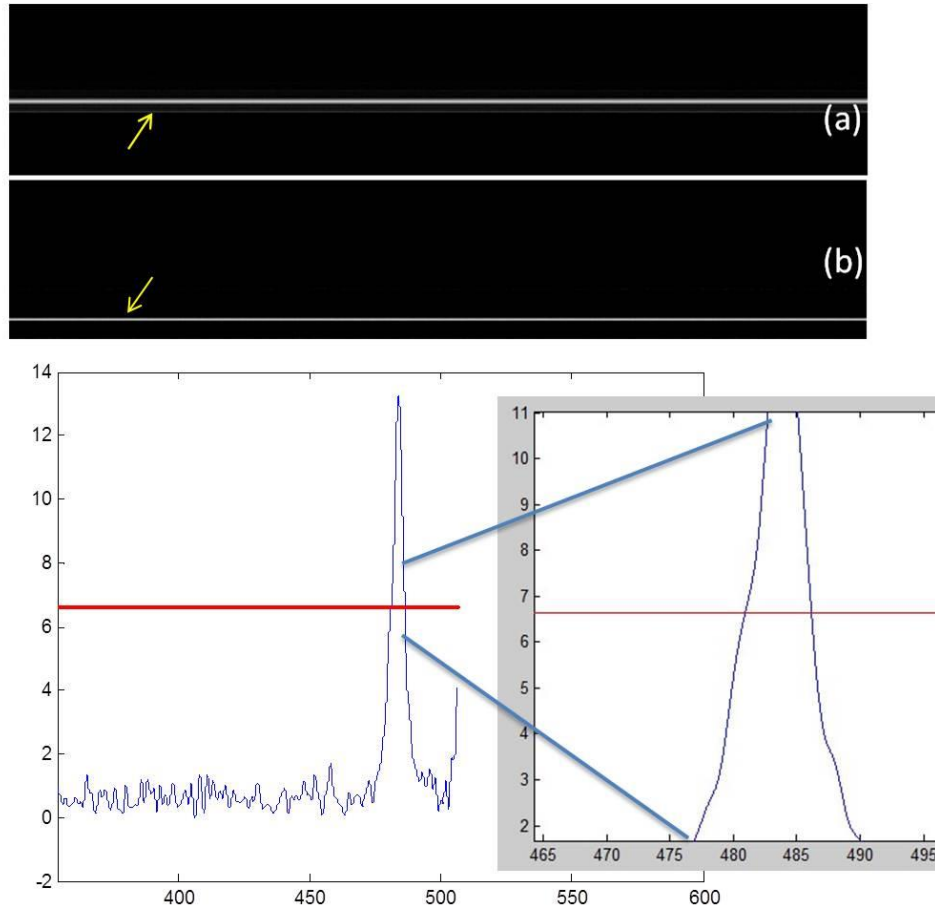
Figure 5 Calibration. (a) Image of a mirror before calibration. Arrow indicates deterioration of signal. (b) Image of a mirror after calibration. (c) PSF, i.e. full width half height, after calibration.

3.1.3 Dispersion compensation

Dispersion means the phase of a wave depends on its frequency (wavenumber). Though total dispersion value in a SMF28 fiber at 1310 nm is almost zero, where material dispersion

20

compensates waveguide dispersion, there are still two other causes of dispersion in our 1310 nm system. First, we employ a fiber-based (probe) sample arm while the reference arm is in free space. Light dispersions are different when light transfers in these two arms. Second, the bandwidth of the laser source is 100 nm. Although there is almost no dispersion in the fiber at the center wavelength of 1310 nm, dispersion still cannot be naturally compensated for at other wavelengths. Similar to calibration, dispersion compensation also finds a relationship between $\Delta\Phi$ and t. The only dissimilarity is that $\Delta\varphi$ is not a constant. The phase difference $\Delta\varphi$ is a function of k. With this principle in mind, the dispersion mismatch between the two arms of the OCT system can be compensated for by digitally canceling the frequency dependent nonlinear phase (33).

3.2 Spectral domain optical coherence tomography

3.2.1 Design of linear-k SDOCT

In Fourier domain OCT, the signal as a function of wavenumber k is obtained to reconstruct the image. A Fourier transform between k and the depth z is then performed. However, signals sampled with uniformed wavelength interval are acquired in the traditional SDOCT design. When we transform wavelength to wavenumber using the equation $k=2\pi/\lambda$, those sample points that correspond to lower wavelengths are more under-sampled than those of longer wavelengths (because $\Delta k=2\pi\Delta\lambda/\lambda^2$). As a result, the sensitivity of the signal drops quickly as the depth of the image increases. Thus, a linear-k spectrometer design, where singles are obtained with a uniform k interval, is preferred for a SDOCT system.

Our linear-k spectrometer was made using a transmission grating, a prism, a multielements lens, and an InGaAs line-scan camera, see Figure 6. The prism was applied to diffract light and generate a distribution of light on the camera with a uniform k interval (34).
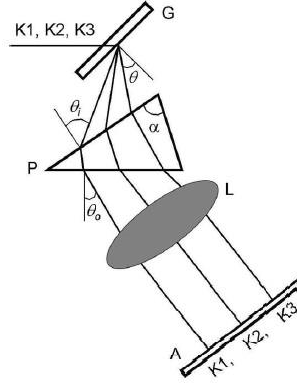
Figure 6 Schematic of the alignment of the linear k spectrometer (34)

The alignment of the grating and the prism is revealed according to the grating equation:

$$d\,(\sin\theta_{00} + \sin\theta) = m\lambda \tag{3-7}$$

Where d is the width of each line in the grating, θ_{00} is the incident angle on grating, and θ is the diffracting angle for each wavelength λ. To get lower order diffraction where the energy of light is higher, we usually choose m=1. Note: different wavelengths are not separated when m=0.

The famous Littrow configuration, $\theta_{00} = \theta$, was chosen. Since d= 0.873 nm and λ_{center}=1310nm, θ can be calculated as 48°.

With the existence of the prism, the output angle after the prism θ_0 can be expressed by (34):

$$\theta_o(\lambda) = \sin^{-1}(\sin(2\alpha)\sqrt{n(\lambda)^2 - \sin(\theta_i)^2} + \sin(\theta_i)\cos(2\alpha)) \tag{3-8}$$

Where $\theta_i(\lambda) = \sin^{-1}(n(\lambda_c)\cos(\alpha)) + \sin^{-1}(\mu\lambda - 0.5\mu\lambda_c) - \sin^{-1}(0.5\mu\lambda_c)$.

To ensure linear k, the derivative of θ_0 with respect to wavelength should be a constant.

There is a range of α values that can make sure the derivative is almost a constant (35). When δε <= 0.2%, distortions caused by the nonequidistance of detection of spectral components is insignificant.

3.2.3 Modifications made in the design of the SDOCT system

A Superluminal diode with center wavelength of 1310nm was chosen for imaging vessels, due to its high penetration depth. However, silicon based cameras are not applicable for obtaining images at this wavelength. An InGaAs camera was used instead. In general, the imaging speed of an InGaAs camera is lower than that of a silicon-based camera, which is lower than the sweeping speed of a swept laser. (Thus, SSOCT can usually image faster than SDOCT.)

With the development of InGaAs cameras, the speed of our system can improve. A new camera, Goodrich SU1024LDH2, was bought and installed to the previously developed system (36). Apart from using the new 93 kHz InGaAs camera, two other changes were made in the design of the SDOCT system to make it perform better.

First, an achromatic lens was added to the reference arm to balance the dispersion in the reference and sample arm. The sample arm consists of a collimator, two Rayleigh lens and one achromatic lens. The path length in air is 12 cm. However, the reference arm, under the original design, consisted of only a collimator and a mirror, with 8cm path length in air. The dispersions of the sample arm and reference arm were not balanced. Thus, I used an achromatic lens (red arrow in Figure 7) in the reference arm and designed the reference arm with a ~12 cm path length in air to compensate for the dispersion in sample arm. The lens focuses the collimated light and also makes the alignment of the reference arm easier.

Second, a dual-axis goniometer was added to control the incline angle of the prism. The old design only used a rotating stage to position the prism with a desired β and desired distance to the grating, i.e four degrees of freedom. However, the prism may not be coaxial with the light coming out from the grating. Thus, I used a dual-axis goniometer (red arrowhead in Figure 7) to fine-tune the prism's rotations about the x and y axes, i.e, adding two more degrees of freedom.
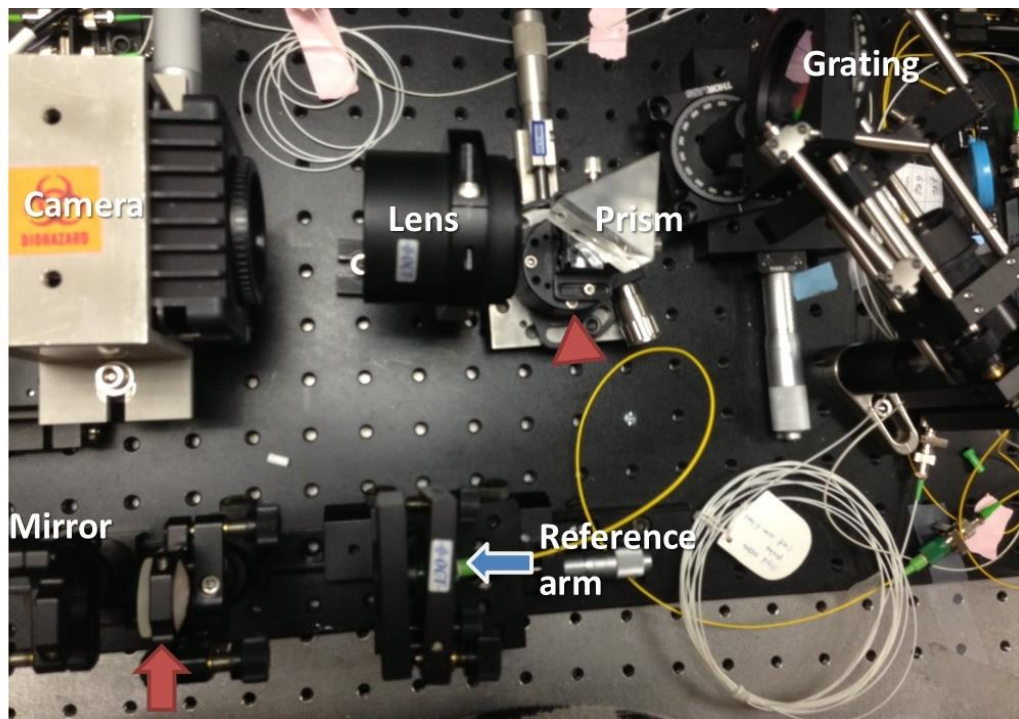
Figure 7 Photo of the SDOCT system with goniometer and achromatic lens.

3.2.4 Practical guidance for aligning the SDOCT

If the image quality is not better than Figure 8, the possible reasons are listed below.

1. The galvanometer mirror has two sides. One side of it has an ultra-high reflection coating. It is critical that this side is facing the incident light.

2. The distance between the multi-element lens and camera influences the image quality significantly. It is also critical that the camera sensor is located at the focus of the multi-

24

element lens. When the distance is correct, the spectrum signal from the FBG should be extremely-thin lines. Meanwhile, the FBG lines are needed to be matched with the marker lines in the user interface.

3. Sometime, self-interference (one surface of the sample constructively interferences with another surface of the sample) may happen, when the light arrives at the sample arm too strong. Here is the method to confirm the existence of self-interference: block the reference arm and check whether the interference signal still exists.
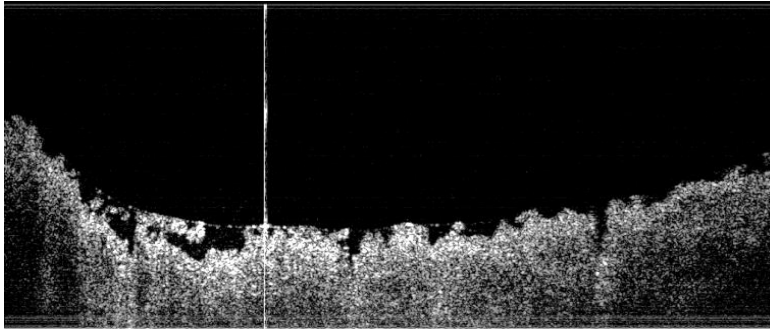
Figure 8 Example of a good image obtained in the SDOCT system

3.3 IVUS system

In the IVUS subsystem, a Panametrics PR5900 pulser/receiver (Olympus NDT, Kennewick, WA) is used to drive the transducer for pulse generation and subsequent echo signal detection, for 20 fps system. 2 μJ pulse energy is used to drive the transducer. 26 dB gain and 10-100 MHz band-pass filter are applied to the received RF signals. For the more advanced design, a 50 kHz-external-triggered ultrasound pulser/ receiver (DRP500, JSR ultrasonics, Pittsford, NY) is used to drive the transducer and detect the eco signal.

For the IVUS signal processing, the captured IVUS data is digitally filtered with a pass band of 20-60 MHz to help isolate the echo signal from the pulse followed by a Hilbert transform and

logarithmic scaling.

3.4 Development of an ultrafast integrated OCT-IVUS system

Because SSOCT system is more compact than SDOCT system and easier to be used in hospital, we choose the SSOCT design to be integrated with IVUS for intravascular imaging.

Several prototypes of the integrated IVUS-OCT system, with a frame rate up to 4, were developed (37-40). However, the translation of integrated IVUS-OCT system into clinical practice was hindered by the large gap between IVUS and OCT imaging speeds (21). 32 fps is the fastest speed which has ever been reported in using a commercial IVUS system, while commercial OCT systems usually perform over 100 fps. That is to say, an IVUS-OCT system can only operate at IVUS's limited speed. With the 32 fps ultrasound imaging speed, an extensive amount of the contrast agent was needed, but would be extremely dangerous for the patients (for example, 40-second injection of 120 ml contrast agents will be required if a 10 cm artery is imaged). The use of contrast agents may lead to renal function disorder (41). Some patients may also encounter life-threatening reactions, such as cardiotoxic effects and seizures. We have proved that the speed of IVUS imaging system is theoretically possible to be increased (42). Here we successfully addressed this challenge by technical advancements (a more advanced IVUS pulser/receiver, electrical slip ring and customized catheter design, etc). This work greatly narrows the gap in translating the IVUS-OCT technology to the clinical applications.

The ultrafast integrated IVUS-OCT imaging apparatus consists of three major components: integrated IVUS-OCT catheter; motor drive unit and imaging system. A block diagram illustrating the construction of the apparatus is shown in Figure 9. The integrated IVUS-OCT

catheter is a single disposable catheter which is capable of IVUS and OCT imaging simultaneously. The motor drive unit is the interface between catheter and imaging system, which includes a rotational motor, linear pullback stage and signal coupling joints. The imaging system is composed of several hardware units as well as custom built software, responsible for controlling transmitting, receiving and processing IVUS and OCT signals.

The overall imaging performance has been benchmarked. In 2012, the frame rate of the imaging system was achieved to 20 fps with 500 A-lines per revolution and 8192 sampling points in each A-line. In 2015, the frame rate of the imaging system is now achieved to 72 fps with 800 A-lines per revolution and 4096 sampling points in each A-line. The system is capable of real time displaying and raw data saving for both IVUS and OCT. Pull-back speed is now 12.5 mm/s. Resolutions of OCT imaging are 8 μm and 30 μm in axial and lateral directions, respectively. Resolutions of IVUS imaging are 57 μm and 275 μm in axial and lateral directions, respectively, with a 40 MHz ultrasonic transducer.
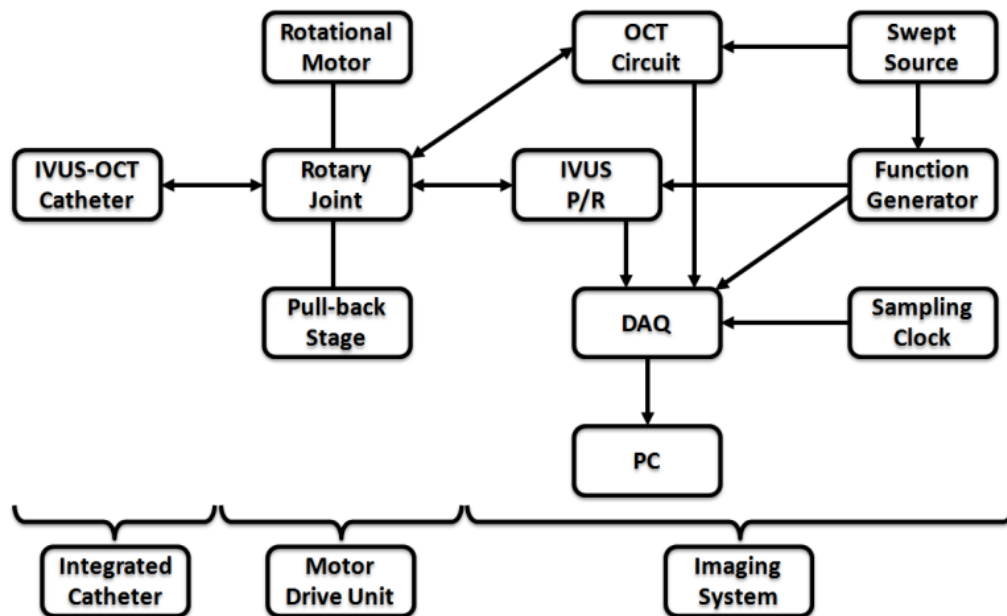
Figure 9 Diagram of the integrated IVUS-OCT imaging apparatus, which is composed of integrated IVUS-OCT catheter; motor drive unit and imaging system

3.3.1 Motor Drive Unit

A custom built motor drive unit (middle portion in Figure 9) interfaces the IVUS-OCT catheter and imaging system, as shown in Figure 10. The unit is used for motion control and signal coupling between the rotational part and the stationary part. A rotational motor is linked through a belt to a fiber optic rotary joint, which connects the integrated catheter via the OCT connector to translate rotational torque. The optic rotary joint and a brushed electrical slip ring are used for OCT and IVUS signal coupling, respectively, to allow the whole probe rotate freely. All these components are fixed to a linear translation stage which functions for imaging pull-back.
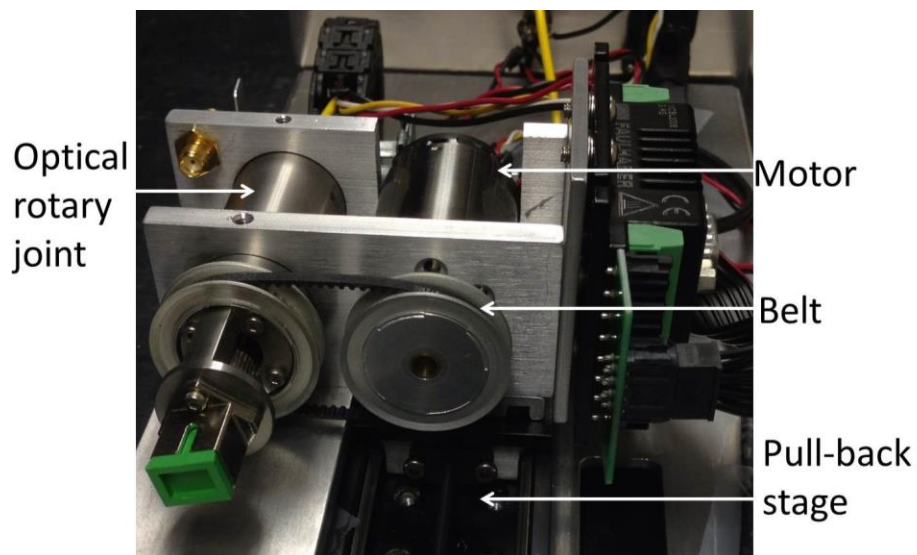
Figure 10 A rotary joint device connects the rotational and pull-back motor; and couples electrical and optical signals between the rotational and stationary parts

3.3.2 Ultrafast integrated IVUS-OCT Imaging System

The integrated IVUS-OCT imaging system (right portion in Figure 9) is responsible for transmitting and receiving IVUS and OCT signals; data acquisition (DAQ); and synchronization. The imaging system is composed of laser source, OCT circuits, ultrasound pulser/receiver (P/R),

digitizer, computer, as well as custom built software.

The swept-source laser source in the OCT sub-system generates 20 kHz or 50 kHz trigger signals which drive a function generator to synchronize the digitizer and the pulser/receiver. For the 20 fps system, IVUS and OCT signals are fed into separate channels of the 12 bit digitizer and digitized at a sampling rate of 200 MHz. The sampling clock is provided by an external voltage controlled oscillator (VCO). The reason of choosing 200 MHz sampling rate is multiple. High frequency broadband IVUS signals (40 MHz) require a certain degree of oversampling to avoid aliasing. However, since OCT signals require full fringe period sampling, higher sampling rate will dramatically increase the amount of data generated at both channels of the digitizer. The 200 MHz sampling rate is chosen to balance the data processing time and IVUS/OCT image quality. For the 72 fps system, IVUS and OCT signals are fed into separate channels of the 12 bit digitizer and digitized at a sampling rate of 250 MHz, using the internal clock of the digitizer.

The acquired IVUS and OCT signals are processed, displayed and saved in real time by custom built software. The framework and control mechanics are completely written in C++ while the entirety of the data processing is implemented in NVIDIA's CUDA software development kit (SDK). Processing of the data occurs on a frame by frame basis. The data set size (8192) per A-line is chosen to be a power of two to speed up Fast Fourier Transform (FFT) calculations. The acquired frames are transferred to the onboard memory of a GPU (NVIDIA GTX 580, NVIDIA, Santa Clara, CA) for the respective processing. The OCT data first undergoes resampling [27], either by linear interpolation or spline interpolation, to achieve linearity in the K domain followed by the subsequent inverse FFT and logarithmic scaling. The captured IVUS data meanwhile is digitally filtered with a pass band of 20-60 MHz to help isolate the echo signal from the pulse followed by a Hilbert transform and logarithmic scaling. Both IVUS and OCT

29

sets of data are then scan-converted and formatted into bitmaps and transferred back to the host for display. The GPU acts as a massively parallel processor, allowing for very fast arithmetic computations on large data sets. FFT performance on 1000 lines improved from 421 ms on a single CPU thread to 212 μs using the GPU. Logarithm calculations likewise experienced large scaling improvements from 276 ms on the CPU to 1.05 ms on the GPU. Both linear and spline OCT resampling were implanted with almost negligible differences due to the large oversampling of the data. The overall time to process one pair of IVUS and OCT images from the transfer of data to the GPU until the transfer of the processed bitmaps back into the host's memory is on average 10.5 ms.

3.5 Summary

Both SSOCT and SDOCT systems were developed. But SSOCT was chosen to be used in the integrated IVUS-OCT system due to its compact size and stability. An integrated IVUS-OCT system with a speed of up to 20 fps was achieved in 2012. An integrated IVUS-OCT system with a speed of up to 72 fps was achieved in 2015.

Chapter 4

Catheter design for intravascular imaging

A good catheter design is needed to achieve the goal of safe intracoronary imaging in vivo. Several challenges to catheter designs have been overcome in this process, which is described in this chapter. These challenges include the strict size constraints for the integrated probe (so that it fits the inner diameter of human coronary arteries, 2-8 mm); the flexibility and pushability of the catheter (so that it can navigate smoothly through the human artery tree); the transparency and low toxicity of the catheter material, the achievement of a minimal amount of non-uniform rotational distortion, and the catheter's adaptability for clinical procedures. To fit the catheter's strict size requirements, two miniature OCT-IVUS probe designs were developed (see Chapter 4.1 and 4.2). To fit the necessary mechanical requirements, transparency and low toxicity, the materials for the catheters were carefully selected (see Chapter 4.3). Simple approaches to reducing non-uniform rotational distortion were also researched (see Chapter 4.4).

4.1 Sequential OCT-IVUS probe design

We developed a miniature integrated IVUS-OCT probe (38), Figure 11, which is small enough for imaging inside the coronary artery. The OCT probe design permits light from a single mode fiber to be focused by a 0.35-mm-diameter gradient-index (GRIN) lens and then reflected by a 0.25-mm-diameter micro prism into the sample. A 0.5mm $\times$ 0.5mm 35MHz PMN-PT side-viewing ultrasound transducer is combined with the OCT probe for ultrasound imaging. By arranging the OCT probe and US transducer sequentially, the outer diameter of the integrated

IVUS-OCT probes is decreased significantly to 0.69 mm. This miniature integrated probe simultaneously provides both OCT and ultrasound imaging.
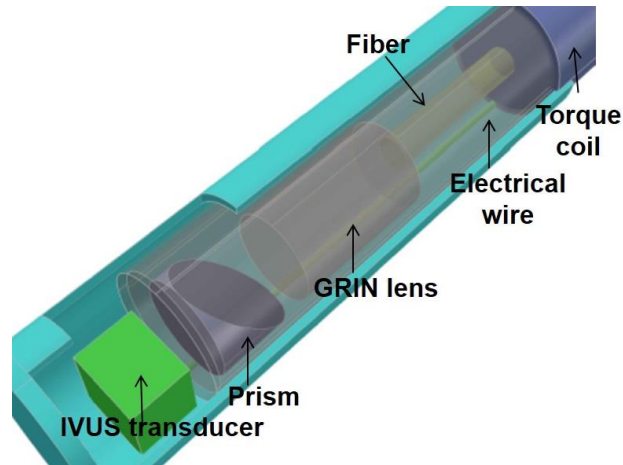
Figure 11 Sequential-design IVUS-OCT probe.

4.2 Back-to-back OCT-IVUS probe design and fabrication

4.2.1 Motivation

In preliminary research, our group first developed an integrated OCT-IVUS system and different imaging probes (37-39), including the previously described sequential design one. Independently, Li *et al*. (40) designed a similar hybrid OCT-IVUS system and used it for in vitro human cadaver imaging. Although Li's design enables co-localized imaging, the side-by-side design prevents co-axial IVUS-OCT imaging and true image co-registration. Recently, we reported the safe and successful in vivo imaging of plaques in rabbits and coronary arteries in a swine, using a miniature probe design (38). However, one limitation of the previously employed miniature probe (38) was its difficulty to co-register data in real-time, due to the offset between the OCT prism and IVUS transducer.

A typical cardiovascular system is shown in Figure 12 d. The system includes several sharp turns: from the descending aorta to ascending aorta, there is a curve of over 180 degrees. Furthermore, the right (or left) coronary artery and ascending aorta are normally 80-90 degrees angularly spaced. This curvy structure demands a probe with high flexibility, small diameter, and short length of the rigid-part to provide safe access to the coronary arteries. In previously reported probe designs (37-40), either the probe's OD is too large or the rigid-part is too long, both of which potentially reduce the safety of catheter interventions. The probe previously reported by our group has a 0.7 mm OD but a rigid-part as long as ~3.5 mm (38), while the probe reported by Li (40) has a 2.5 mm-long rigid part, but an OD as large as 1.0 mm. The back-to-back ball-lens design probe reported here minimizes the probe's rigid-part to 1.5 mm-long, which is the same size as clinically-used IVUS or OCT rigid-parts, while maintaining an OD of 0.9 mm. The reduction of probe size is a significant improvement, which allows for safer access to the coronary artery system. Using available space more efficiently than previous designs, we further reduces probe size without reducing the size of optical lenses, hence maintaining image quality.
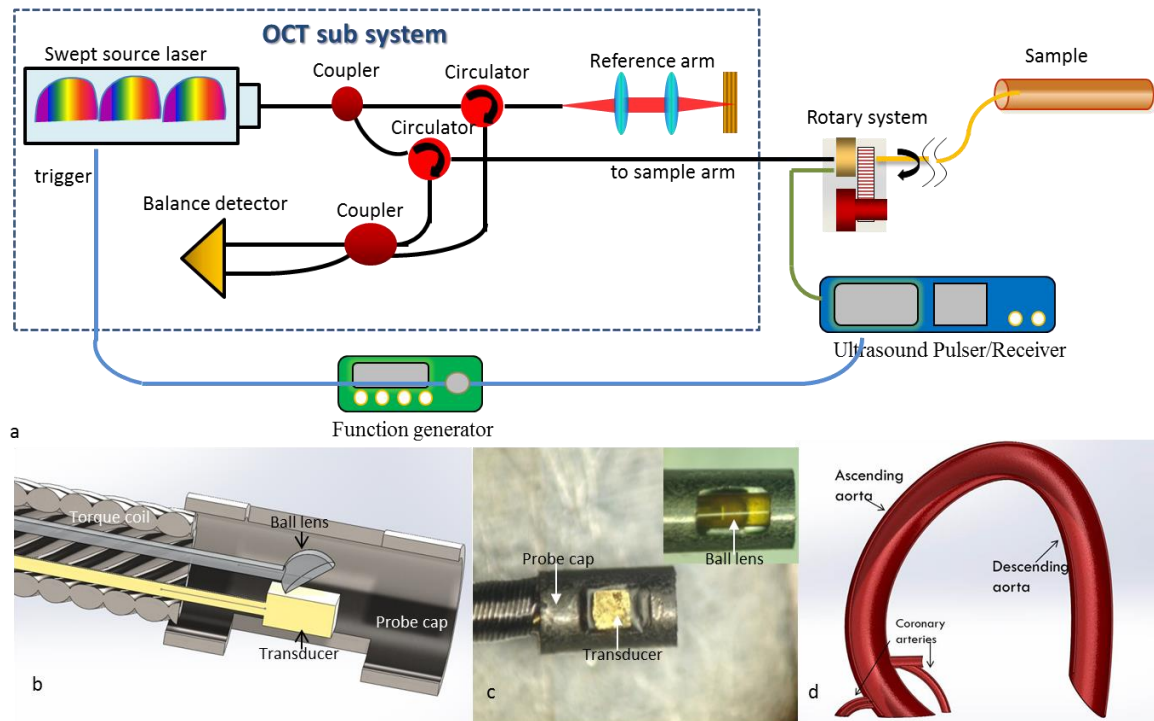
Figure 12 (a) Schematic of the integrated imaging system. The dashed box illustrates the OCT sub-system, a swept source OCT system. Black lines, a green line and a blue line denote the optical path, the ultrasound path and the electrical trigger signal, respectively. (b) Schematic of back-to-back OCT-IVUS probe, (c) Photo of back-to-back probe, showing the transducer. Insert: photo showing the OCT sub-probe, (d) Schematic of cardiovascular system

4.2.2 Materials and Methods

With the guidance of visible light from the OCT-sub probe, a back-to-back, co-registered OCT-IVUS probe (Figure 12 b and c) was made by carefully aligning an OCT sub-probe with an IVUS sub-probe, while confirming that the light beam and sound wave exit at the same axial position, but 180 degrees apart. This integrated probe provides automatically co-registered and co-axial fusion imaging. The combined probe was then inserted into a customized probe cap (a stainless steel tube with two windows; OD: 0.9 mm; length: 1.5 mm). Following the probe cap, we used a double wrapped torque coil to encompass the fiber and electrical wire, giving the

34

probe adequate flexibility and torque control. During experiments, the probe was inserted into a sheath. Water was filled in the sheath to facilitate ultrasound imaging.

We used a 0.4 mm x 0.4 mm x 0.3 mm 45 MHz (1-x)[Pb(Mg1/3Nb2/3)O3]-x[PbTiO3] (PMN-PT) single element transducer for our IVUS sub-probe, which is thinner than in previous designs (37, 38). The functional element was lapped to a thickness of only 300 μm before it was mechanically diced into 0.4mm*0.4mm square shape. The center core of a coaxial cable was connected to the side of the backing layer and covered by epoxy to insulate from the front electrode without increasing the thickness of the transducer. For the OCT sub-probe, we chose a ball-lens design, which enables less insertion loss and stronger interfaces (43) than the traditional GRIN lens design (40). Ball lenses also have the potential to be manufactured in large quantities while maintaining constant performance. A single mode fiber was fusion-spliced to a fiber spacer (cladding OD: 0.125 mm; reflective index: 1.457) using a splicing workstation. Then, a ball with a 560 μm-long fiber spacer (43) was created at the distal end of the fiber spacer using the splicing workstation. This ball lens can generate a beam focusing at ~1 mm from the ball surface. Next, the lens was mechanically polished until the angle between the polished surface and optical fiber was less than 37 degrees. The ball lens was later inserted into a sealed polyimide tube, isolating the ball lens from the water in the sheath and maintaining an air-fiber interface to ensure that the total internal reflection (TIR) was generated at the polished surface.

4.2.3 Characterization of probe performance

The working distance and focal spot of the ball lens can be measured by the Dataray beam profiler. The intravascular OCT probe that we used has a working distance of 1.2 mm and a beam radius of 35 μm.
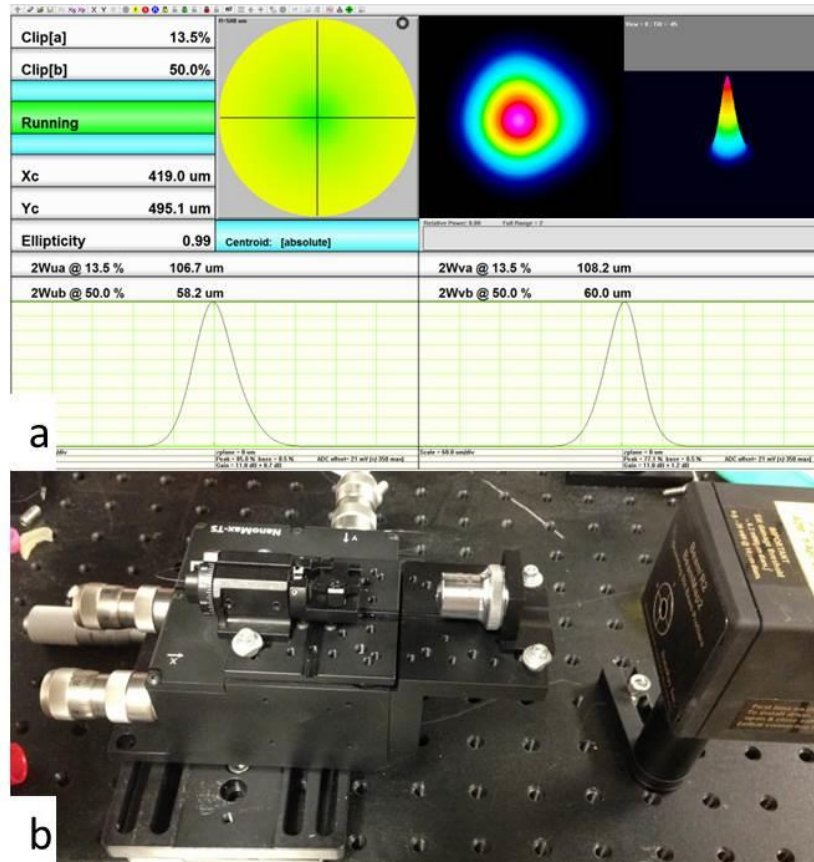
Figure 13 Characterization of OCT probe (a) Beam spot measurement of the ball lens OCT probe. (b) The optomechanics system to clamp a ball lens and measure its beam spot.
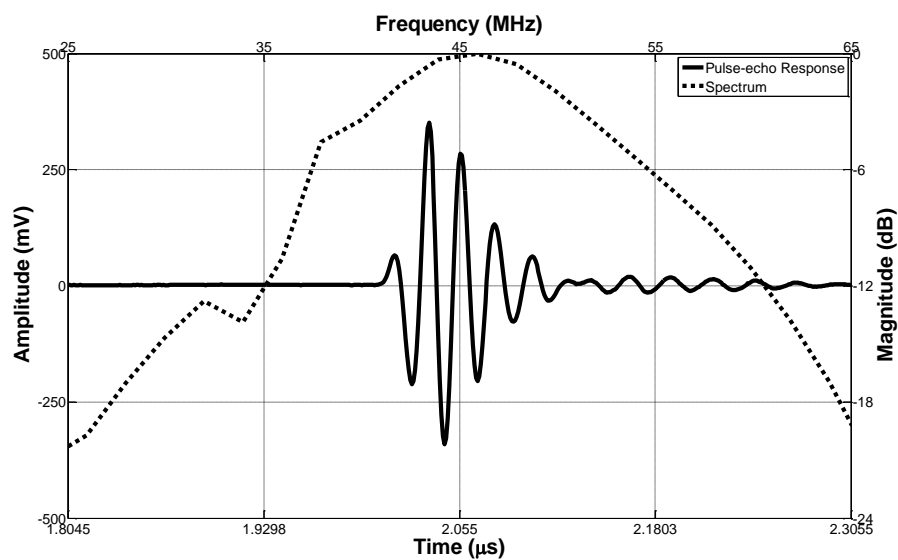
Figure 14 The time domain pulse-echo waveform and frequency spectrum of the IVUS probe with 1mm long coaxial cable connecting to a slip ring.

Figure 14 showed the time domain pulse-echo waveform and frequency spectrum of the IVUS probe with 1mm long coaxial cable connecting to a slip ring. The testing was performed in de-ionized water with an X-cut quartz plate as reflecting target at room temperature. The setting of pulser/receiver (Panametrics PR5900, Olympus NDT, Inc., Waltham, MA) was the same as experiment condition with a 100 Vpp negative pulse. At the focal depth of 1.5 mm, the amplitude of received echo signal was found to be 700 mV without amplification. The center frequency of IVUS transducer was found to be 45 MHz. The transducer exhibited a center frequency of 45 MHz and a -6 dB fractional bandwidth of 40%. Thus, the IVUS transducer with thin thickness (300 μm) demonstrated satisfied performance compared to previous published results (37-39).

4.3 Catheter design

4.3.1 General requirements

In order to satisfy the requirements of clinical procedures, our catheter (including the probe and outer sheath) shares the following characteristics. First, a 0.65 mm outer diameter double wrapped torque coil is used outside of the optics fiber and electrical wire is used for protection instead of the stainless steel tube. This torque coil transmits the rotation of the proximal end accurately to the distal tip. Furthermore, its flexibility allows the torque coil to maintain performance even in bent sections. As such, it is possible to use the catheter in a clinical study where the coronary artery is accessed through the femoral artery and the catheter is required to make a ~ 180-degree sharp bend. Second, in the same design as the IVUS catheter, the probe was spinning within a 3.6 Fr catheter sheath, see Figure 15, to protect the probe from contamination and also help to avoid causing trauma to the inner vessel wall. For the integrated IVUS-OCT

catheter, a special material for the sheath needs to be used which is not only transparent to US but also IR light to avoid noise in US or OCT images. Third, the precise position of the imaging probe is identified by two X-ray-detectable marker bands. A 0.40 mm inner diameter channel is engineered at the distal end of the sheath for the catheter in order to work as a standard guide wire rail. Last, but not least, with over 160 cm in usable length, when the catheter is inside the body, 15–20 cm of intracoronary length is able to be achieved during a procedure.
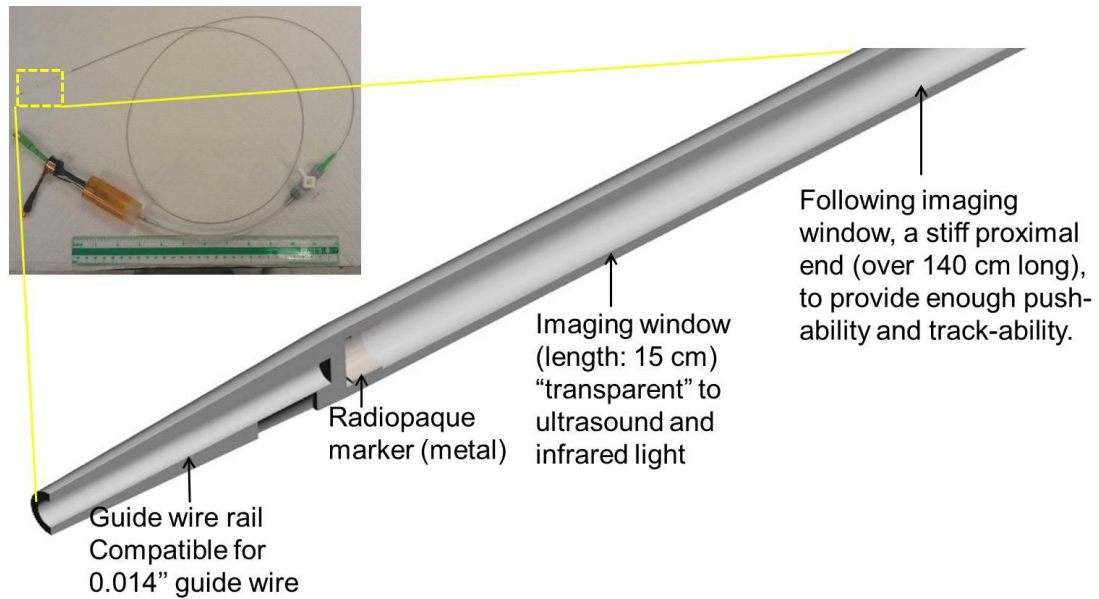
Figure 15 General requirements of IVUS-OCT catheter sheath. Top inset, photograph of IVUS-OCT catheter sheath.

A comparison between our integrated catheter and commercially available IVUS/OCT catheters is shown in Table 2. It illustrates that the dimensions of the catheter, dose of OCT laser and ultrasound frequency, and techniques used by imaging for our probe are identical to what are currently in use (and approved) on human subjects.

Table 2 A comparison between our IVUS-OCT catheter and commercially available OCT or IVUS catheter

		Our integrated IVUS-OCT catheter	Latest commercial IVUS catheter	Latest commercial OCT catheter
General dimensions	Total Usable Length(cm)	135	135	135
	Intracoronary Usable Length	>15cm	>15cm	28cm
	Imaging Window Profile	3.2F	3.2F	2.7F
Sheath design	6F Guide Catheter Compatibility	√	√	√
	1.5 cm guide wire rail length	√	√	√
	Marker band for precise positioning	√	√	√
OCT imaging probe	No need for occlusion balloon	√	√	√
	Laser Power to artery	3mW	~5mW	NA
US imaging probe	Transducer frequency	35~45 MHz	20~45 MHz	NA

Usually, the higher the mechanical strength (the thicker the material or with the material's higher durometer), the higher the reflection that will be generated. To ensure the high pushability of the catheter and the high transparency of the catheter's imaging window, we used different materials for the imaging window and the proximal side of the catheter. We used a high durometer material for the proximal side to provide high pushability and trackability. A relatively soft low-ultrasound-attenuation material was used to ensure image quality (see Chapter 4.3.2). These two

materials were thermally bonded together to ensure a smooth transition and a strong connection between the imaging window and the proximal side.

4.3.2 Selection of the material of the imaging window

The material selection is very critical for ensuring image's good quality. We first attempt to find the right sheath material by testing different materials that are available off-the-shelf. Figure 16 shows images obtained using different sheaths.
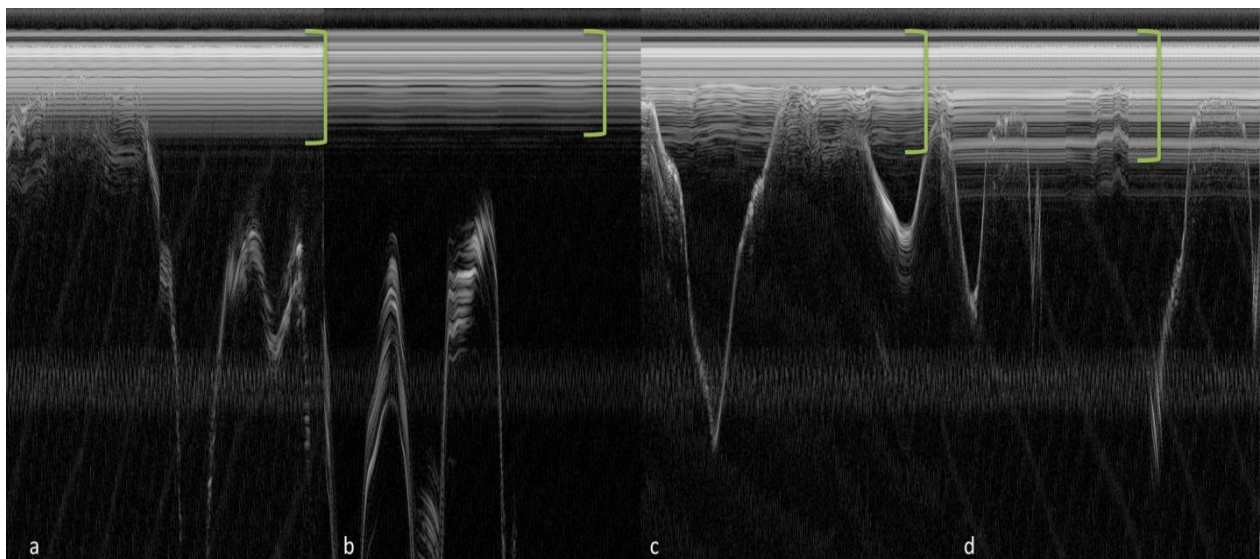
Figure 16 Ultrasound image with different sheaths a) without sheath b) using commercial IVUS sheath c) Pebax 55D d) Pebax 72D green brackets denote the ring down effect caused by the ultrasound pulse and sheath.

4.3.3 Design for eliminate torodial astigmatism

As mentioned previously, a sheath is usually needed for in vivo imaging. However, the surface of a sheath—a toroidal with high reflective index—acts like a negative lens in the y direction when light passes from air to the sheath (44). This causes the focus of the y direction to be different than the focus of the x direction. This phenomenon is called astigmatism.

In commercially-available intravascular OCT probes, this effect is minimized by purging an index-matching liquid into the sheath before OCT imaging. Usually, a sterile saline solution (with a refractive index of ~1.4) is used. The effect of the injected liquid is simulated by Zemax, as shown in Figure 17, where light focuses in the x and y directions at approximately the same point.
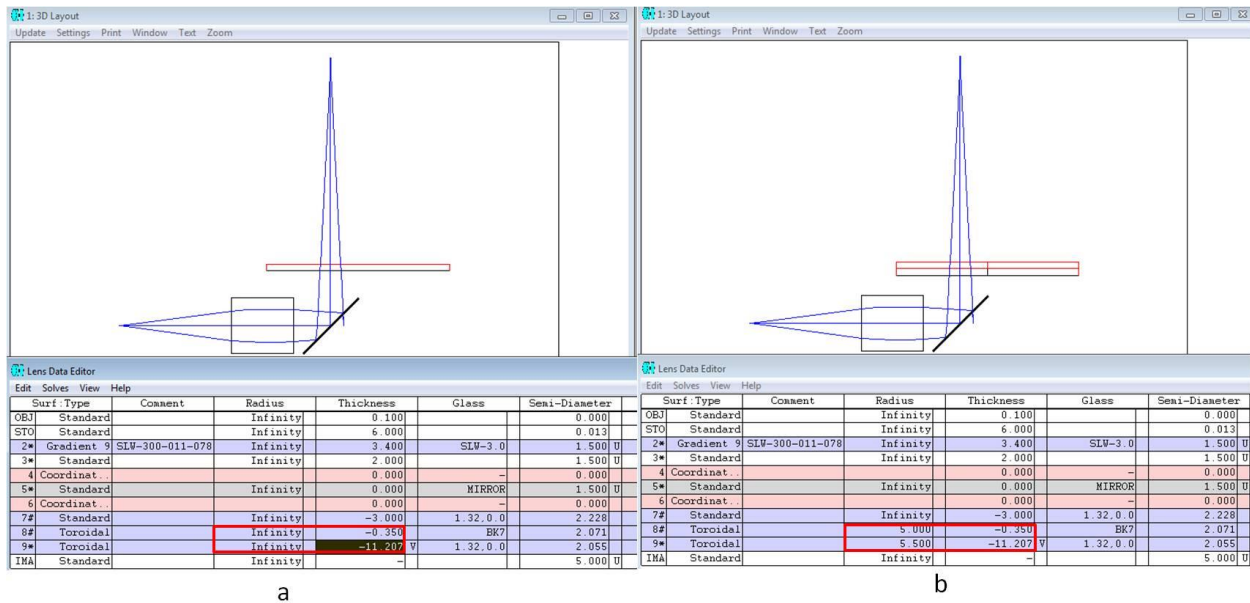
Figure 17 Simulation of the light focus in (a) the x direction (b) the y direction. Red box shows the difference of radius between the x and y directions.

In IVUS-OCT probe design, liquid has to be injected into the sheath for the coupling of ultrasound signals. However, an extra layer of tube is used in the ball-lens design to ensure total internal reflection (discussed in Chapter 4.2). To compensate for the astigmatism caused by the toroidal of the polyimide tube, the ball lens is intentionally morphed into an ellipsoid. Via Zemax's simulation, we found that a 150µm-radius ball with a 0.5 mm radius polyimide tube generates a beam that has a working distance similar to that produced by an 180 µm-radius ball without a toroidal sheath (Figure 18). Thus, we specifically designed our ball lens's fusion-splice

procedures to make the ball lens an ellipsoid shape: 180 μm-radius in the X-direction and 150

μm- radius in the Y-direction.
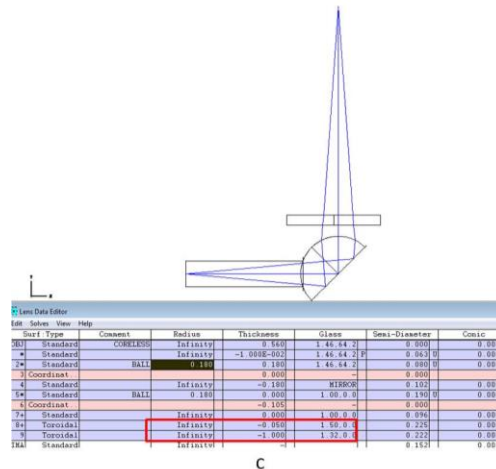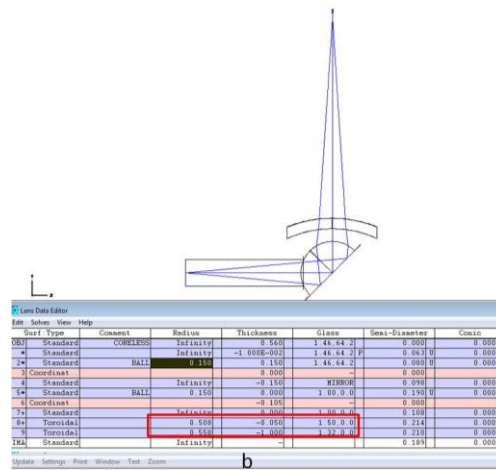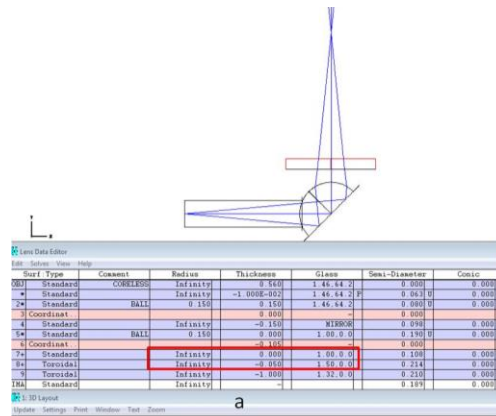
Figure 18 Simulation of the light focus of the ball lens in (a) the x direction (b) the y direction for ball lens and (c) the x direction with a different ball radius, highlighted by the black box. Red boxes denote the difference of radius between the x and y direction.

4.3.4 Nonuniform rotational distortion

Nonuniform rotational distortion (NURD) is caused by either motion artifacts and/or non-uniform catheter rotations (45). In our system, signal acquisition speed is set to be the same as the rotating speed of the motor. The motor rotates the proximal end of probe through a timing belt. If the image scanning speed, i.e. the distal end rotating speed, is the same as the signal acquisition speed, no NURD is going to be generated. However, the rotational speed of the probe distal end is not always the same as the speed of the probe proximal end, because of bulk motions (such as breathing or heartbeat) or non-uniform rotations of the catheter. Distortion in the image is then induced by non-synchronization between the signal acquisition speed and the rotation speed.

The major reason for the mismatch between distal and proximal speeds is friction. Friction between the probe, sheath and water inside the sheath causes variations in the rotation speed. This effect becomes stronger when the probe passes tortuous bends. Physical approaches and algorithm correction can be used to minimize NURD.

The principles of various physical approaches are the same: to reduce friction and to keep the speed of the distal end the same as the proximal end of probe. To reduce friction in an IVUS-OCT probe, we could inject more lubricating fluid into the catheter sheath for IVUS coupling. However, this approach was not investigated due to the concern of FDA approval for the fluid. To keep the rotation transmitting more uniform, we tried a more rigid torque coil design. This new design has 4 more filars per layer than the old design. The inner diameter and outer diameter of the new torque coil are the same as the old one. With this design, NURD is reduced.

Apart from physical approaches, algorithms can also be used to reduce NURD. Dynamic time wrapping (DTW) is one of the algorithms that has showed efficient reduction of NURD (45). The idea of DTW is to match two time series by finding the optimal path through a construct cost matrix, and then use the A-line shift path to reconstruct the image. The implantation of this algorithm into our system was researched by a rotation student, Krit Charupanit, who was instructed by me.

4.4 Summary

This chapter discussed the development of an integrated IVUS-OCT catheter. The catheter was made of an imaging core and sheath. Two different designs were used for the imaging core. The sequential design ensured the outer diameter of imaging core to remain as small as possible, while the back-to-back design enabled real-time co-registered IVUS-OCT imaging capability and short rigid-part length. The sheath material was specially selected and the sheath was specially designed to match standard intervention procedures.

Chapter 5

In vivo IVUS-OCT imaging

Prior to all in vivo imaging, we investigated on acoustic and optical flushing agents, so as to perform the in vivo experiments in animals without inducing great amount of toxicity. To demonstrate the potential of the ultrafast IVUS-OCT for evaluating plaques in vivo, we first imaged the aortas of atherosclerotic rabbits, vessels which are comparable to the caliber of human coronary arteries. We then imaged porcine models, which offer close approximations of human heart and coronary artery anatomy. Such models are commonly used prior to human cardiovascular research to validate the design of catheters (their pull, torsion, flex, buckling, pull back, resistance, leaking, etc).

5.1 Flushing agent selection

5.1.1 Motivation

Integrated intravascular ultrasound and optical coherence tomography (IVUS-OCT) has the potential to provide better visualization of coronary lesions (40, 46, 47) and improve accuracy of atherosclerotic plaque characterization (48). Great progress has been made in developing a fully integrated IVUS-OCT system and catheter. However, to our knowledge, no research has been performed to find optimal flushing agents that provide both the necessary clarity for OCT and IVUS.

Blood is a high-scattering source for OCT signals and high definition IVUS (HDIVUS). Either blood occlusion or continuous flushing is needed for intravascular OCT imaging. Although no flushing agents are needed in 40 MHz IVUS imaging, some OCT flushing agents may hinder the

45

transmission of IVUS signals, such as perfluorocarbon (49), when using IVUS and OCT functions simultaneously. Thus, it is critical to identify flushing agents that are effective for IVUS-OCT imaging. This research will also benefit acousto-optics (AO), photoacoustic (PA) imaging and spectroscopy, acoustic radiation force optical coherence elastography (ARF-OCE) and other imaging techniques that simultaneously use light and ultrasound.

X-ray contrast agents (such as iohexol and iodixanol) are commonly used for intravascular imaging to clear blood for OCT (50). However, the use of contrast agents in some patients may lead to renal function disorder (41) or life-threatening reactions, such as cardiotoxic effects and seizures (51). It was reported that one dominant reason that physicians avoid using intravascular OCT is the injection of extra contract agents (52). Although combined light and sound based techniques are very promising for improving health outcomes, the wide clinical utility of these techniques will not be achieved until the challenge of safe and effective flushing is addressed.

Dextran (53, 54) and oxygen-carrying blood substitute perfluorodecalin (PFD; a type of perfluorocarbon) (55) have been previously studied as alternative flushing agents for OCT imaging. These have minimal toxicity compared to contrast agents (54, 55). Dextran reduces scattering of red blood cells by matching refractive indices between blood plasma and blood cells (56). PFD, which has high viscosity, can displace blood and clear OCT images. However, PFD can cause significant reduction of the ultrasound signal (40). In addition, PFD has not been approved by the FDA and cannot be used in patients (57). Accordingly, PFD was excluded from our quantitative experiments. We also considered using mannitol solution as a flushing agent, based on mechanisms of optical flushing. Mannitol injection is approved by the FDA and is typically used to promote diuresis and reduce intracranial/intraocular pressure. Last but not least,

iohexol is a commonly used contrast agent for OCT flushing. Its toxicity is lower than iodized contrast agents (58).

To pave the road for new imaging techniques with both acoustic and optical functions, we studied the principle of flushing and experimentally evaluated the attenuation characteristics of flushing agents using an integrated IVUS-OCT system. We selected three solutions as representative flushing agents for testing because of their image-enhancing effects and relatively low toxicities: mannitol, dextran and iohexol.

While previous testing on flushing agents has been performed in static baths (56, 59, 60), we chose to mimic complex, dynamic in vivo human coronary arteries using an in vitro circulatory system model and live rabbits.

5.1.2 Methods and Materials

5.1.2.1 In vitro circulatory system model

To avoid unknown variables as in animal experiments, a well-controlled phantom test was first performed for comprehensive quantitative analyses of different flushing agents. An in vitro circulation model was built (shown in Figure 19) according to the dimensions of a human arterial system, to best mimic the circulation system in vivo. This model was a closed loop system, simulating the heart-artery-vein-heart closed loop circulation, and made from Masterflex L/S® tubes, tube adapters, three-way luer valves, a glass jar, and a peristaltic pump. Similar to the middle of the human left anterior descending coronary artery, where intravascular imaging is usually performed, the tubing had an inner diameter of 2.4 mm. The total length of all tubes with blood flow was 3 m, which simulated the blood circulation through the entire arterial and venous system. Since the distance between the imaging region and the guiding catheter influences the

efficiency of flushing (61), this distance was also controlled to be similar to the in vivo distance. The peristaltic pump's parameters were then set to mimic the pressure profile of human circulation. The fluid reservoir was physically located 1m above the imaging region which raised the minimal blood pressure to 78 mmHg, approximately the diastolic pressure of a healthy human. The peak pressure during pumping was approximately 40 mmHg higher than minimum, mimicking a systolic pressure of 120 mmHg. The pump was then set to ~60-80 times/minute, mimicking the normal heart rate.
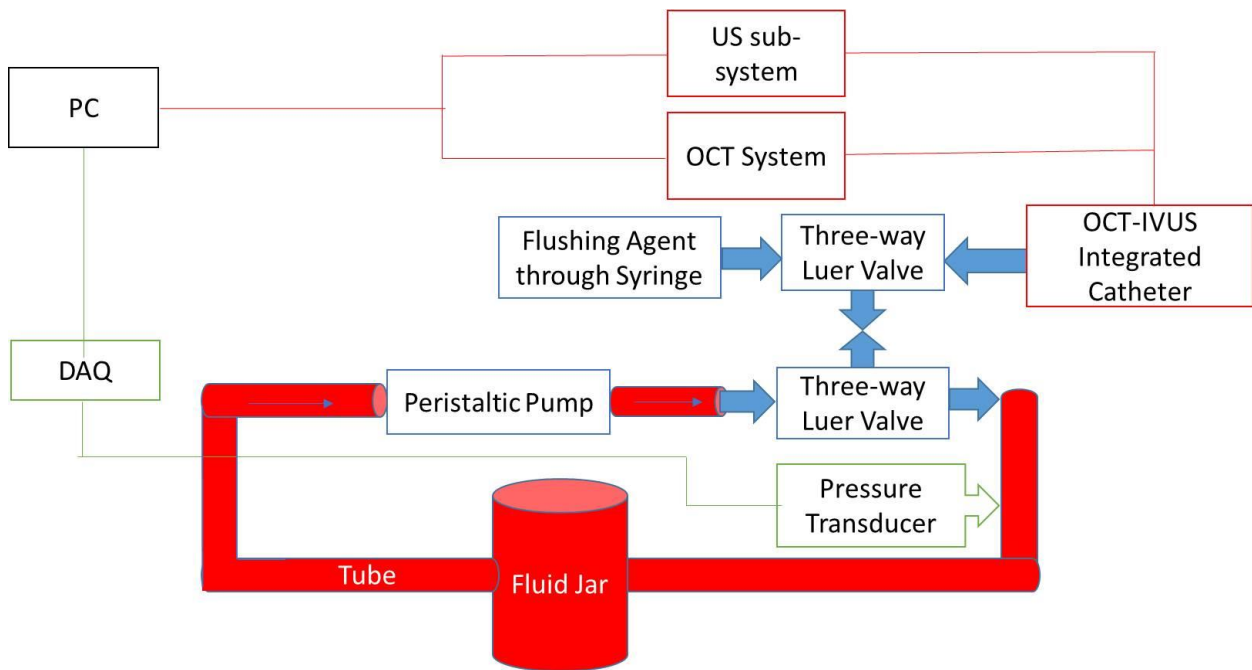
Figure 19 Schematic of the in vitro circulatory system model with signal acquisition devices. The Personal computer (PC) acquired the OCT signal, IVUS signal, and fluid pressure signal. Three-way luer valves were used to provide access to the closed-loop tube system and allow the imaging probe and chemicals to enter. Red areas denote where blood circulates.

Three flushing agents, dextran [40,000 molecular weight (MW)], 20% mannitol in normal saline, and iohexol (350 mgI/ml, NOVAPLUS), were examined in our quantitative experiments. Because the concentration of dextran solution was reported to affect the enhancement of OCT image quality (56), we tested the effect of dextran with different concentrations at 1%, 3% and

5%. Although dextran with high MW, such as MW 500,000 or 70,000, may provide better blood optical clearing (62), high MW dextran takes a longer time to be extract from human body (63). Thus, we used dextran MW 40,000 in our experiments.

The maximal injection speed of a flushing agent commonly used in patients is 4 ml/s at the coronary artery proximal (54, 64). To keep the volumetric delivery of flushing agent comparable to the in vivo setting, we chose 1 ml/s as the maximal testing speed because the inner diameter of our tube is one half of the inner diameter of the coronary artery proximal end, where flushing is usually performed. All three flushing agents were tested at flushing speeds 0.1 ml/s, 0.5 ml/s, and 1 ml/s.

During the experiment, 500 ml EDTA-added (anti-coagulated) porcine whole blood was circulated inside the circulation model. Imaging was performed using our previously published IVUS-OCT system (42) with a 1310nm OCT system and 40 MHz IVUS transducer. We obtained 1000 A-lines in each frame.

An ideal flushing agent should provide minimal attenuation with the lowest possible delivery; therefore, we measured the attenuation during imaging for each agent at each speed setting. In each A-line, the attenuation coefficients (AC) of each flushing agent at each speed setting were calculated in the equations (65) below using Matlab:

$$R(z) = I_0 \, T(z) \, e^{-2\alpha z} \tag{5-1}$$

$$R(z) = I_0 \, T(z) \, e^{-\mu z} \tag{5-2}$$

where R is the intensity of the signal obtained in ultrasound or OCT system, I0 is the intensity of

the outgoing sound signal or the incident light intensity. T is the reflectivity of the sample as a function of scanning depth, α is the ultrasound AC, and μ is the optical AC.

To minimize the effects of tube heterogeneity and speckles in images, 10x10 pixel windows were averaged. The means and standard deviations of the AC for all 1000 A-lines were then calculated. The AC of an adjacent three-image unit was then averaged to obtain the final AC value of the corresponding flushing agent at its corresponding speed. Summaries of these final values for each setting are shown in Figure 20 and Figure 21.

5.1.2.2 In vivo studies

To demonstrate the clinical applicability of these flushing agents, simultaneous optical and acoustic imaging of rabbit abdominal aortas was performed in vivo. The experiment protocol was approved by the University of California, Irvine Institutional Animal Care and Use Committee (IACUC). All animals were treated in accordance with federal and state regulatory guidelines. During the imaging procedures, rabbit were anesthetized, intubated and mechanically ventilated. Laparotomy was performed. The thoracic aorta was then isolated and exposed. At this opening, a 6-F arterial catheter was inserted into the aorta (66). The IVUS-OCT catheter was advanced through the 6-F arterial catheter and into the abdominal aorta. We examined three flushing agents, 10% dextran (40,000 Da MW) in normal saline, 20% mannitol in normal saline, and iohexol (350 mgI/ml, NOVAPLUS), in the abdominal aortas of three anesthetized rabbits, which mimic the diameter of human coronaries (55). To evaluate the effect of different flushing agents in the in vivo experiment, clear image frame (CIF) was used as a criteria. CIF is defined as the image frame where over 270 degrees continuous arc of artery wall can be visualized, similar to previously published concepts (53, 54).

5.1.3 Results

5.1.3.1 Phantom result

OCT image quality increases as the flushing speed increases. Dextran at 5 g/dL and flushed at 1 ml/s had strong effects on both OCT and IVUS (10.3% μ decrease, 4.16% α increase). Mannitol at 1 ml/s had marginal effects on both OCT and IVUS signals (4.6% μ decrease, 3.37% α decrease). Iohexol at 1 ml/s dramatically improved OCT signals (23% μ decrease) but hindered IVUS signals (17% α increase). Iohexol had the best effect for OCT flushing. The high concentration of dextran, when flushing at a high speed, can provide a flushing effect similar to that of low-speed iohexol.
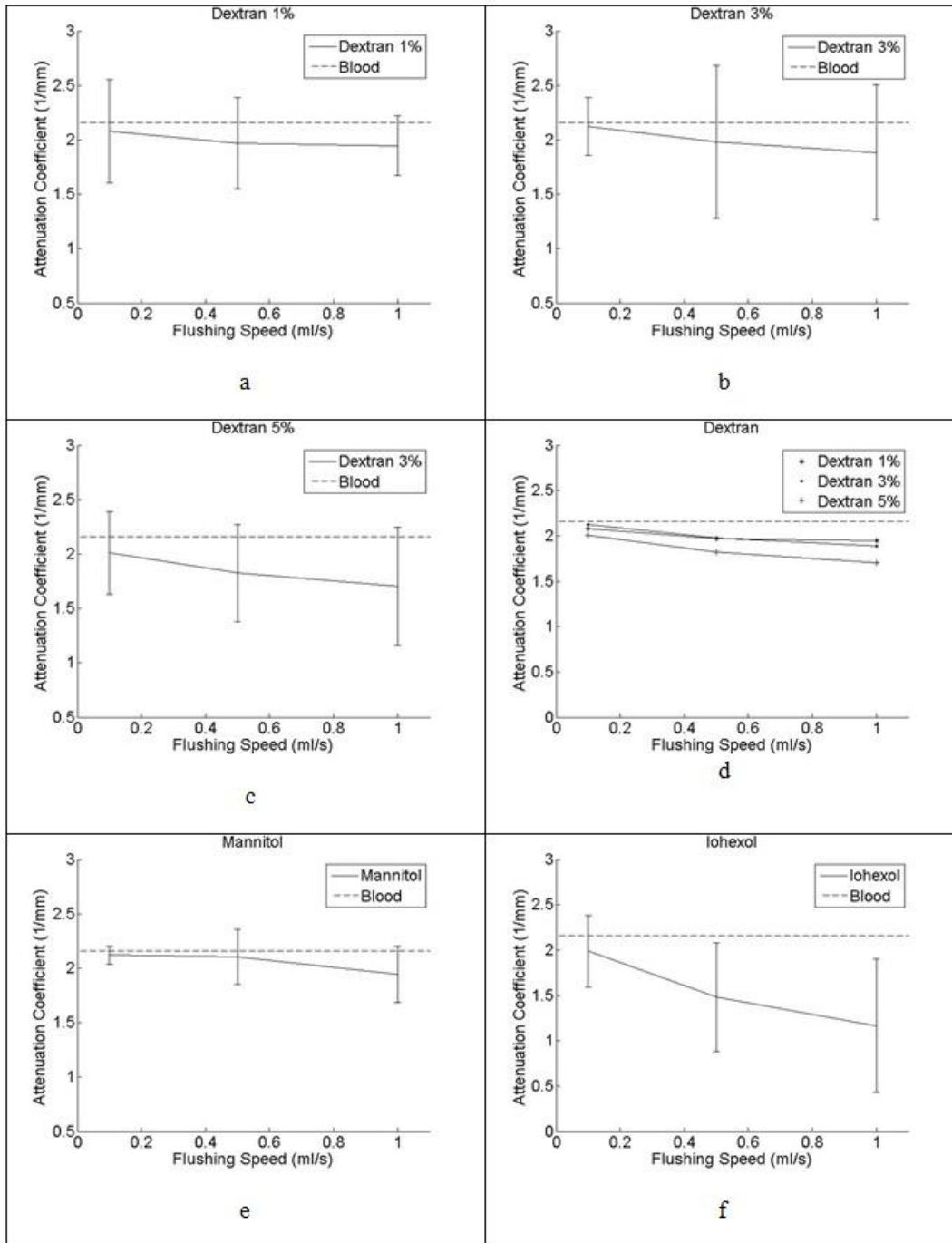
Figure 20 OCT ACs using different flushing agents. Dashed lines represent the AC of blood at 2.16 mm^{-1} (56). The error bars represent the standard deviation of ACs encountered when rotating the imaging probe along the tube wall.
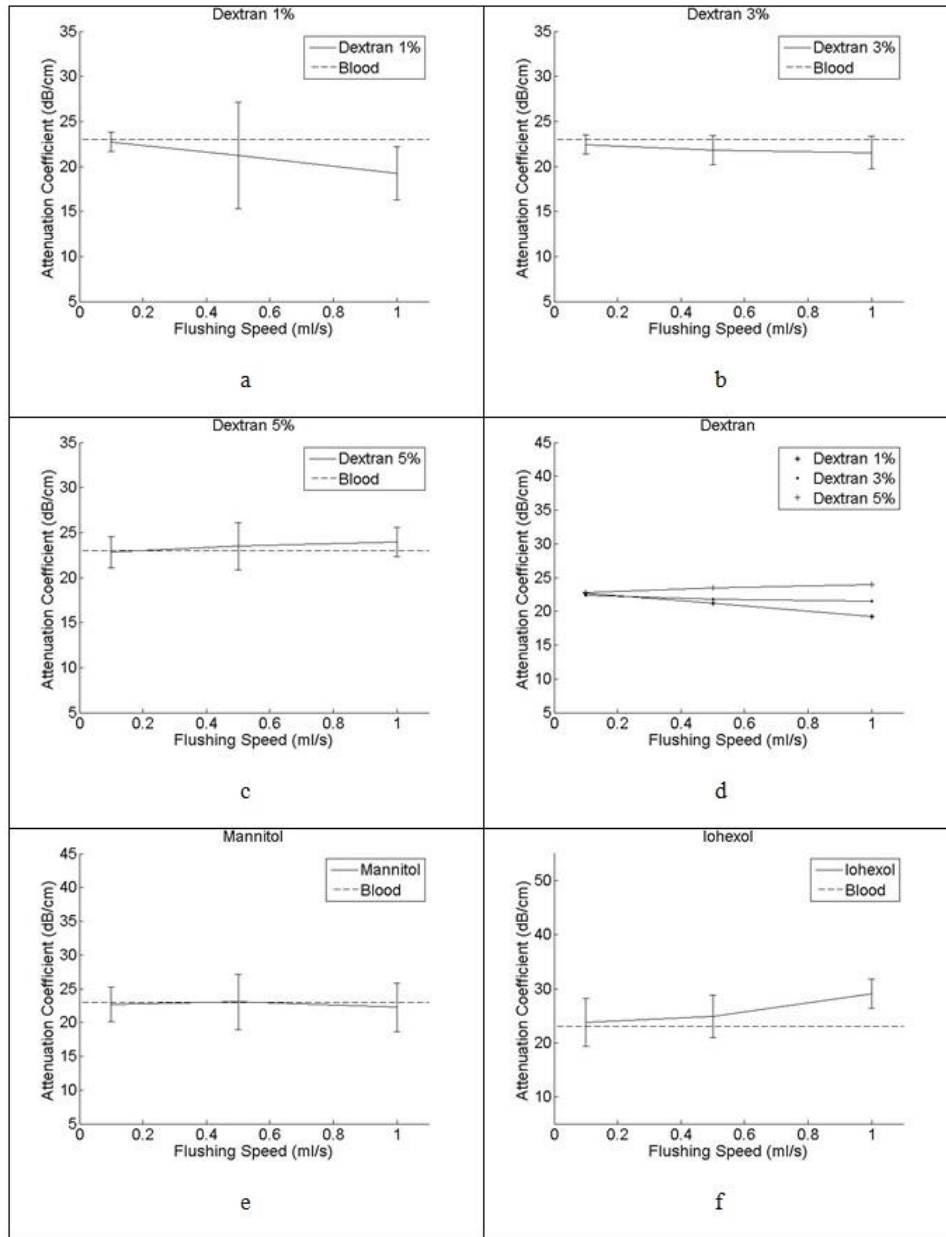
Figure 21 IVUS ACs using different flushing agents. The AC of blood is 23 dB/cm (shown in dashed lines) (67).

5.1.3.2 In vivo result

From the acquired OCT images, CIFs are 99%, 97.5% and 50% for iohexol, dextran, and mannitol flushing, respectively. There were many image frames acquired with mannitol flushing that were partially clear, see Figure 22 (c), but most image frames acquired with dextran were

clear. Based on the semi-quantitative criteria of CIFs, different flushing agents showed a similar effect on IVUS images.
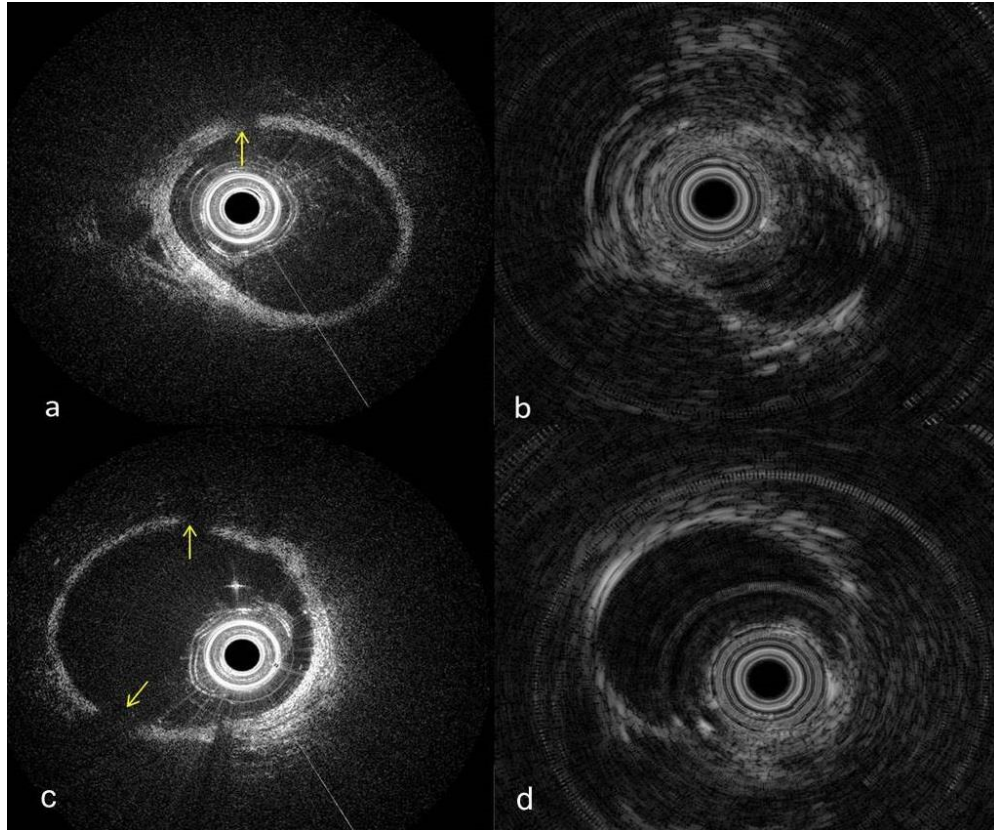
Figure 22 Representative images acquired with alternative flushing agents, dextran (a), (b) and mannitol (c), (d). (a), (c) are OCT images of rabbit artery. (b), (d) are corresponding IVUS images. Arrows denote areas where the artery wall is not visible in the image.

5.1.4 Discussion

From our phantom testing and in vivo experiments, we found that dextran at a high concentration worked well for both IVUS and OCT, as measured by a low optical and US attenuation and a high CIF rate. Mannitol was not very effective for OCT flushing while iohexol reduced the US signal. Here, we attempt to explain these results by the mechanisms behind OCT and US flushing.

5.1.4.1 Mechanisms of improving OCT image quality

Two mechanisms are associated with the increase of OCT imaging quality: index matching and the displacing of blood.

Attenuation of optical signals is caused by absorption and scattering. At 1310 nm, where water absorption is negligible compared with scatterings, and where the absorption of hemoglobin is also low, scattering is the dominant source of attenuation. Scattering of light is generated by the difference in the index of refraction between the scatterer and surrounding medium (56). By employing index matching chemicals and raising the refractive index of blood plasma (n=1.33) to match that of blood cells (n=1.40) (53), the OCT light experiences a lesser change in the refractive index at the plasma-cell interface. During the in vivo experiment, 10% dextran (n=1.349), mannitol (n=1.357), and iohexol (n=1.46), which have higher refractive indices than plasma (n=1.33), increased the refractive index of the mixed solution towards that of RBC (1.40). Extensive studies of index matching and optical clearing were investigated for reducing scattering in the stagnant blood imaging (56, 60).

In flowing blood, however, there is another mechanism associated with reducing scattering. As shown in our results, 1% dextran, which has a refractive index (1.334) similar to that of blood plasma (1.33), can still improve OCT image quality. A flushed chemical may completely displace blood in which case refractive index matching does not matter because no plasma-cell interface exists. In a completely displaced medium with a constant refractive index, very little scattering occurs. Flushing low concentration dextran displaces some blood, decreasing the number of plasma-cell interfaces and thus reducing scattering. This explains why flushing low

concentration dextran improved the OCT signal despite its refractive index similar to that of blood plasma.

Table 3 Comparison of Viscosities and Refractive Indices

Chemical	Viscosity at 20 ℃ [cP]	Refractive Index at 589nm
Dextran 1%	3.23*	1.335**
Dextran 3%	4.34*	1.338**
Dextran 5%	5.89*	1.342**
Dextran 10%	12.18*	1.349**
Mannitol	5.2948 (68)	1.357 (69)***
Iohexol	20.4 ****	1.46 (70)
Blood plasma	1.39-1.64 (71, 72)	1.33 (53)
Red blood cell	N.A	1.40 (73-75)

* Logarithmic interpolation of data from a paper (76).

** Calculated by the equation from (77).

*** Refractive index of 20% mannitol was not available. Closest is 16%.

**** NOVAPLUS Omnipaque™ (iohexol) injection.

5.1.4.2 Mechanisms of improving IVUS image quality

Similar to light attenuation, the attenuation of sound is caused by acoustic absorption and scattering. The strength of absorption is related to the viscosity of material and the velocity of the flow. More friction and thermal consumption of energy will be induced when sound propagates through high viscosity media at a high speed (78). The higher the viscosity is, the stronger the resistance to shearing flow and thus the larger friction that is generated. In addition, a higher flushing speed in a high viscosity medium causes a larger speed difference between the medium flowing over the surface of the tube/artery wall and the medium flowing in the center of the

tube/artery wall. As a result, a high speed flushing may generate stronger friction. Iohexol, which has the highest viscosity, caused a stronger ultrasound signal reduction than other tested chemicals (see Figure 21), and a high flushing speed of iohexol induced an even stronger reduction than at a lower speed [see Figure 21 (f)].

High viscosity is a double-edged sword for acoustic-optical imaging. Chemicals with higher viscosity most likely displace more blood because they have stronger internal "stiffness" in pushing blood forward. This hypothesis is consistent with our results that both dextran 5% and iohexol had higher viscosities than mannitol and that they improved OCT signals better than mannitol. However, higher viscosities are known to cause more acoustic attenuation due to the increased damping of mechanical energy (67). As revealed in Figure 20 (d) and Figure 21 (d), increasing the dextran concentration (and thus, viscosity) deteriorated the IVUS signal and improved OCT image quality. Similarly, iohexol (a high viscosity chemical) increased IVUS attenuation but reduced OCT attenuation. In the context of simultaneous IVUS-OCT imaging, the medium's viscosity may serve as a critical parameter in determining the optimal balance between OCT and IVUS signal strengths. Dextran at a high concentration, with an intermediate viscosity, worked well for both IVUS and OCT. It is also significantly less toxic than iohexol, which may also enable us to perform IVUS-OCT imaging even on patients with renal insufficiency (54). Thus, we believe dextran is a good contrast agent for simultaneous IVUS-OCT imaging.

5.1.4.3 Effect of blood aggregation

Occurring when blood cells "stick" onto one another through fibrinogen protein interactions, aggregation alters the blood's state and hence its AC. More specifically, aggregation is

hypothesized to affect the OCT AC because it reduces the number of interfaces with different refractive indices (56). Additionally, aggregation is believed to affect the ultrasound AC because of sound reflectivity's dependence on particle size (67). Aggregation, however, typically occurs in stagnant blood or flowing blood with very low shear rates. For our experiment, the average shear rate across the pump's tube diameter was at 56 inverse second (s^{-1}), which was high relative to lower shear rates at 0 to 15 s^{-1} (79). Thus, aggregation was assumed to not occur. In addition, we did not observe any aggregation or sedimentation processes in the experimental images, as shown in Figure 22, so changes in ACs must be caused by the introduced chemicals and their interactions with blood, not the blood interacting with itself to form cellular aggregates.

5.1.4.4 Outlook

Flushing, or optical clearing, is not only necessary in OCT but also in other optical based imaging methods, such as optical elastography, acoustic-optics and photoacoustic imaging (80). For example, stronger intravascular photoacoustic signals were detected in an experimental setting without blood than were detected with blood showing the necessity for effective flushing agents (81). In addition, optical clearing has also proven to be useful for enhance imaging performance and sensitivity in photoacoustic microscope (82, 83) and flow cytometry (84). HDIVUS (with a center frequency of over 50 MHz) recently received FDA approval and has caught physicians' attention at prestigious medical conferences due to its remarkable resolution (85, 86). However, unlike common IVUS, HDIVUS also suffers from reduction in image quality from blood scattering and performs better with a flushing agent (87). With the system setup mentioned in this paper, the ideal non-toxic flushing agent for HDIVUS can easily be found. This study will also potentially benefit the clinical adoption of HDIVUS. Based on our research,

we would argue that the optimal IVUS-OCT flushing agent should have an index of refraction over 1.34 and a viscosity lower than 15 cp.

In this paper, we quantitatively investigated three representative flushing agents. However, more optical clearing agents, such as glucose solutions, propylene glycol (59) and hemoglobin (88-90), can be investigated using the methods proposed in this paper. Before in vivo experiments, a preliminary theoretical analysis and low-cost phantom testing would be useful for initial screening.

5.1.5 Conclusion

We analyzed the effects of three flushing agents (dextran, mannitol and iohexol) in a blood-filled closed loop tube system and in vivo on rabbits. Dextran improved intravascular OCT signals, with higher concentrations leading to stronger signals, but it had variable effects on IVUS signals depending on concentration. Mannitol had a marginal impact on both OCT and IVUS signals. Iohexol significantly improved OCT signal but also significantly deteriorated the IVUS signal due to its high viscosity. From in vitro results, flushing high concentration dextran at 1ml/s was most useful for simultaneous IVUS-OCT imaging. This conclusion confirms previous reports (54, 56) that dextran performs well in intravascular OCT which can replace harmful contrast agents and thus reduce the side effects from intravascular imaging. In vivo result also validated the effectiveness of dextran for simultaneous IVUS-OCT imaging.

5.2 In vivo rabbit imaging

To demonstrate potential of imaging plaques in vivo, we performed 3D imaging of atherosclerotic plaque microstructure in rabbit models. The rabbit model is one of the most

commonly used and successful animal models for atherosclerosis research (91). Lesions similar to atherosclerotic plaques were developed in the abdominal aortas of rabbits (92), where the size of artery lumen is similar to the human coronary artery lumen. A smaller animal model such as the rat cannot be utilized given the small size of their vessels and heart.

5.2.1 Methods and materials

The experiments followed the guidance of a UC Irvine IACUC approved protocol 2009-2897. The first step was to develop a model of atherosclerosis. Six male New Zealand white rabbits were fed a high-cholesterol diet (0.5% cholesterol, 6% peanut oil, Newco distributors, inc). After 1 week on the diet, de-endothelialization procedures were performed on all rabbits. We inserted a Fogarty arterial catheter via a femoral artery and advanced to the level of diaphragmatic recess of the aorta. Next, we inflated the balloon catheter to 8 atm and pulled back in the abdominal aorta to the level of approximately the common iliac arteries. The balloon was deflated and the above de-endotheliazation process was repeated for a total of three passes within the abdominal aorta. After surgery, rabbits were continuously fed with the high cholesterol diet. After 12-16 weeks, lesion formation was mature. It is believed that these lesions produced by balloon de-endothelization and high-cholesterol diet are similar to human atherosclerosis plaques (92).

In the second phase of the study, we proceeded with imaging atherosclerotic plaques using the OCT-IVUS system. A total of 12 volumetric data sets were obtained from 5 rabbits. During the imaging procedures, the rabbits were anesthetized, incubated and mechanically ventilated. Sternotomy was performed to expose the heart and the thoracic aorta. The thoracic aorta was then isolated and exposed. At this opening, a 6-F arterial catheter was inserted into the aorta (66).

The OCT-IVUS catheter was advanced through the 6-F arterial catheter and into the abdominal aorta. During approximately 4 seconds, several 2-8 mm long aorta segments were imaged. Perfluorocarbon (PFC), saline and Omnipaque (a conventional clinically used CT contrast agent) were used for blood clearance for OCT imaging. Before imaging, a 10 cc flushing agent was flushed into the rabbit aorta at ~3 cc/s. Only Omnipaque is suitable for simultaneous high-quality OCT-IVUS imaging (shown in Figure 23 (b) and (d)), because PFC causes high attenuation for IVUS signal and saline is not effective to clear blood. After imaging, each abdominal aorta was dissected, fixed, embedded, sectioned to 6 μm-thick slides and stained with H&E.

The area of lumen was subject to change between in vivo imaging and histology, due to the reduced intra-lumen pressure after the artery was harvested. Thus, instead of area percentage, the plaque circumference percentage (93) (equal to plaque arc (94, 95) in percentage units) was used as a standard to compare the agreement of OCT images and histology, the agreement of IVUS images and histology, and the correlation of IVUS images and OCT images. Data were compiled using Microsoft Office Excel 2007 and accuracy/reproducibility analysis was performed with R statistical software.

5.2.2 Results

A total of 12 volumetric data sets were obtained from 5 rabbits. OCT-IVUS image pairs and corresponding histology photos of a rabbit abdominal aorta with a lipid plaque shown in demonstrate the image capability of the integrated OCT-IVUS system during contrast agent flushing in vivo. Positive remodeling and low density acoustic signal region (denoted by the arrow in Figure 23 (a)) demonstrate a plaque in US image. However, this image illustrates the inability of IVUS to determinate the plaque types and the plaque cap boundaries. At same site in

OCT image (Figure 23 (b)) a homogenous-boundary, weak-signal region under a high-signal region indicate that this plaque is a necrotic plaque with an overlying fibrous cap. Also, the minimum thickness of the cap can be easily measured to be ~100 μm by OCT, indicative of a "thick" cap fibroatheroma. The classification of plaque type is validated by the corresponding histology photo, Figure 23 (c) and (d), which shows foamy macrophages adjacent to loose necrotic material. This area is covered by smooth muscle and fibrous proliferations at the luminal surface which is consistent with a fibrous cap.
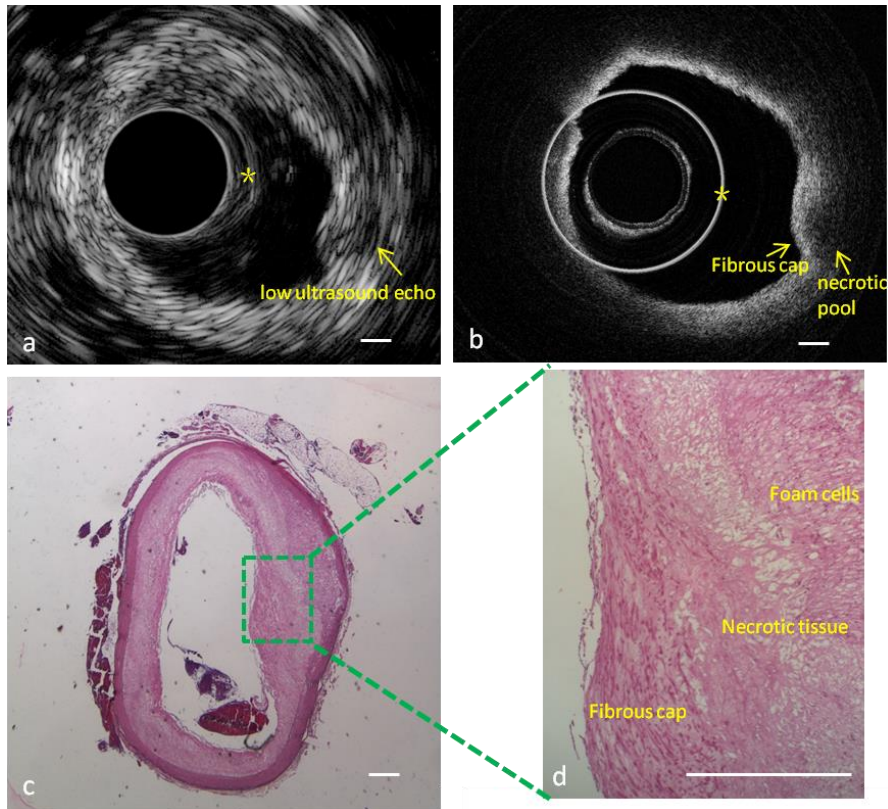
Figure 23 In vivo imaging of rabbit abdominal aorta with OCT-IVUS system. IVUS (a) and OCT (b) cross-sectional images of atherosclerosis microstructure in a rabbit with Omnipaque flushing. (c) Corresponding H&E histology. (d) A high magnified image of the histology slide. Artifact circles in IVUS images, * in (a), are due to the ultrasound pulse ring down effect and the reflection of catheter sheath. Artifact circles in OCT images, * in (b) are caused by the high back reflection from the interface between the prism and GRIN lens. The shape of this artery changed between in vivo imaging (a) and histology (c), due to the reduced intra-lumen pressure after this artery was harvested. Scale bar: 0.5mm.

5.3 In vivo pig imaging

Pigs are commonly used animal models. In general, the cost of a pig (~$300) is lower than that of a dog (~$350) or primate (over $1500). Pigs also have better facility acceptance and anatomical similarities than dogs. For cardiovascular research, pigs are one of the best animal models. The key reasons are: 1) a pig has a coronary artery distribution more similar to human's than other animals; 2) a pig has similar lipoproteins (critical molecules related to the atherosclerosis process) to humans; 3) The morphology and biochemistry of pig plaque is similar to that of human plaque (10).

5.3.1 Methods and Materials

The in vivo swine experiment followed the guidance of a UC Irvine IACUC approved protocol 2009-2910. A 47.0 kg female Yorkshire white swine was anesthetized with Ketamine and Xylazine before imaging. The imaging procedures are done by the conventional femoral access and X-ray guidance. First, the femoral artery was cut down and exposed. A 7 French arterial sheath was then inserted and flushed. Through this arterial sheath, a 7 French guide catheter was advanced and used to engage the ostium of the left main coronary artery. Second, a balance middle weight (BMW) guidewire was then inserted through the guide catheter and advanced through the catheter and into the LAD artery. Over this guidewire, the integrated OCT-IVUS catheter was advanced into the LAD artery. After positioning the device, the artery was flushed with Omnipaque contrast. OCT and IVUS images were obtained at the same time. The imaging system and guide catheter were then removed, and the animal was sacrificed. At last, the imaged section (2 mm) of the LAD was dissected, fixed, embedded, sectioned to 6 μm-thick slides and stained with H&E.

63

5.3.2 In vivo imaging of a swine coronary artery wall structure

To demonstrate the clinical applicability of this integrated system, we performed in vivo OCT-IVUS imaging in a swine coronary artery. The swine model has a comparable heart to body size ratio and similar coronary artery anatomy as humans. Such a model is commonly used prior to human cardiovascular research. The catheters used in this experiment were specially designed and suitable for simple adaptation into routine clinical IVUS (or OCT) imaging procedures. Previous research has found that approximately 95% of human vulnerable plaques are located at the middle to proximal part of left anterior descending (LAD) coronary artery (96). Accordingly, we initiated imaging from the mid portion (~50 mm from coronary ostium) of the LAD of the swine. Then imaging catheter was pulled back and stopped at the proximal to ostial region of the LAD. Our ability to perform this successfully (and without complications) suggests the possibility of safe imaging of the human coronary arteries (considering the similar size of human and swine coronary artery).

Two representative OCT-IVUS image pairs are shown in Figure 24 and Figure 25, respectively. In Figure 24 (a), OCT image illustrates the three-layer structure of the artery wall. From the center of the OCT image, there is a high-signal thin band corresponding to the intima, followed by a high-signal strip corresponding to the external elastic lamina (EEL), and finally a low-signal area corresponding to the adventitia. Since this swine artery is healthy, there is no positive vascular remodeling. OCT is able to penetrate all three layers of the artery wall and provide a clear visualization of layers. On the contrary, the layer structure in an artery with a lipid-rich plaque (see Figure 23 (b)) is sometime difficult to visualize with OCT because lipid is a high attenuation source for optical signal. In the IVUS image (Figure 24 (b)), the three-layer structure

of the swine coronary artery (wall thickness 0.3 mm) is hardly visualized with the resolution of

60 μm. In Figure 25, LAD branching can be visualized.
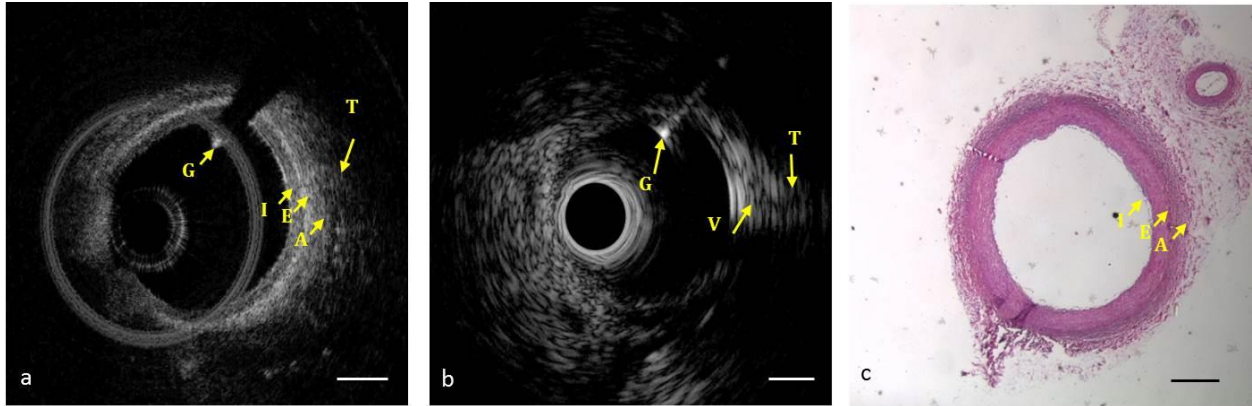
Figure 24 An OCT-IVUS image pair obtained in a normal swine coronary artery in vivo. (a) OCT image (b) IVUS image (c) corresponding H&E histology. ∗ in (a) denotes guidewire artifact. G: guide wire. T: tissue. V: vessel. I: intima. E: EEL. A: advatitia. Scale bar: 1 mm.
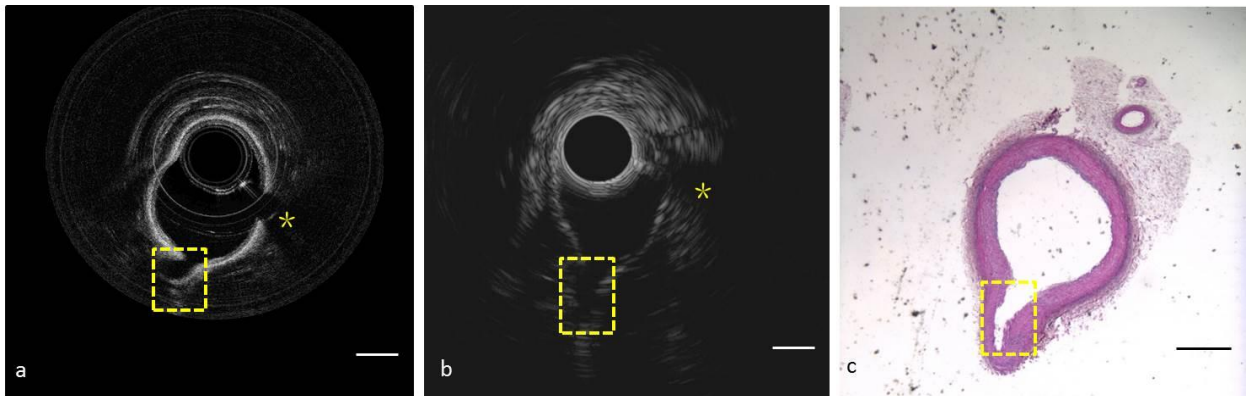
Figure 25 An OCT-IVUS image pair, obtained in swine, demonstrates LAD branching. (a) OCT (b) IVUS cross-sectional image. (c) Corresponding H&E histology. ∗ in (a) and (b) denotes guidewire artifact. Yellow boxes denote LAD branch. Scale bar: 1mm.

5.4 Summary

With the integrated IVUS-OCT system and clinically compatible catheter, in vivo OCT-IVUS

imaging of a thick cap fibroatheroma in rabbit models and a swine coronary artery were achieved

safely and successfully. Alternative flushing agents were also researched to ensure the safety of in vivo experiments.

Chapter 6

FDA application

One important step before using the integrated OCT-IVUS system in patients is to get the approval from the instructional review board (IRB), or the Food and Drug administration (FDA). If a device is categorized as "non-significant risk" then it is exempt from FDA regulation and can be approved to be used in clinical trials by IRB. Significant risk devices includes those intended for use as an implant supporting human life; or have importance in diagnosing, curing and mitigating disease; or represents potential for serious risk to the health, safety or welfare of a subject. The integrated OCT-IVUS catheter is classified as significant risk device by UCI IRB, due to the risks behind the procedures of inserting the catheter. Thus, FDA approval is needed before performing imaging in a human.

The FDA Investigational device exemption (IDE) allows a research device to be used in a clinical study. It is relatively easier than 510(k) and Premarket Approval (PMA). According to IDE guidelines, I wrote a pre-IDE application and submitted it to the FDA. The following information was provided: the name and address of the sponsor, report of prior investigations, investigational plan, a description of methods, facilities and controls, investigators' agreements, IRB, sale, environmental assessment, labeling, and consent forms. Among these listed requirements, risk analysis, managing of potential risks and bench testing are of great importance although they are often overlooked in the engineering design of the system and catheters.

6.1 The additional risks of using the device and its management

Potential risks include:

1. Advancing the imaging device over a guidewire into the coronary artery, and removing the imaging device after imaging has been completed

2. Additional contrast, minimal radiation exposure and procedure time associated with performing the imaging

With respect to #1, there is a theoretical risk that the device could cause mechanical damage to the artery during advancement or that the device could dislodge in the coronary artery. In an effort to minimize these risks, we have placed our experimental device within an approved commercial IVUS catheter sheath, Boston Scientific Atlantis Sr Pro 2 catheter, approved on 08-04-2011as a 510(k) filing with the approval number: K111043. Biocompatible testing has already been conducted for this catheter sheath. The profile of the imaging core is similar to the commercially available IVUS imaging core. The stiffness of the integrated catheter is well-controlled.

With respect to risk #2, we anticipate in patients undergoing OCT/IVUS imaging will have a longer procedure time, increased sedation time, and increased dose of contrast agent. OCT/IVUS imaging will increase procedure time by approximately 5 minutes, which will prolong conscious sedation time by the amount of time required to do additional OCT/IVUS imaging. The increased amount of contrast agent use if OCT/IVUS is performed is approximately 15 mL, which is relatively minimal in comparison to the PCI procedure where total contrast can be up to 300 mL.

Published studies involving in vivo human intracoronary OCT imaging reported no major complications or adverse events (1-3). A multicenter study with intracoronary OCT and IVUS

imaging by Yamaguchi et al (4) demonstrated the feasibility and safety of these modalities. As with any medical therapy, however, there may be risks that cannot be predicted.

OCT/IVUS does not produce ionizing radiation; however there may be a small increase in fluoroscopy time for placement of the OCT/IVUS imaging system (approximately 20 seconds to ensure positioning). The total dosage associated with angiography plus stenting an artery has been estimated at 15 millisievert (1500 millirem) (5). The average fluoroscopy time for percutaneous coronary intervention is approximately 18 minutes (6). Therefore, the additional radiation associated with this study is minimal in comparison to the standard radiation dose.

To manage potential risks, the experimental device is housed in a commercially available sheath as mentioned previously. As with any standard cardiac catheterization and PCI procedure, the cardiologists, investigators, and catheterization laboratory staff will follow the patient closely for side effects, hemodynamic and electrocardiographic changes throughout the study. Appropriate therapy will be administered according to standard of practice and protocol for any discomfort, adverse reactions or complications.

6.2 Required testing

Apart from animal testing, discussed in Chapter 5, the following bench testing is also needed:

1. Mechanical Integrity (e.g., pull, torsion, flex, buckling, pull back, resistance, leaking, flushing system) after fatigue and conditioning testing that are representative of the worst case scenarios of the use of the catheter in clinical practice.
2. Electrical and Electromagnetic Safety (EN 60601-1 and EN 60601-1-2 standards) to ensure the device is electrically and electromagnetically safe in its use environment and demonstrate

that it does not affect and is not affected by the clinical devices in its intended use environment during clinical study.

3. Biocompatibility: any material in contact with the patient (skin, fluids, tissue) need to be demonstrated as biocompatible according to their duration in the clinical scenario (ISO 10993-1)

4. Sterilization

5. Preliminary effectiveness of the device (image qualities, measurement accuracy etc)

6. Laser safety, ultrasound safety

7. Software documentation and validation.

As for software validation, the classified level of concern for our software is "major" (the "major" level corresponds to a failure or latent flaw that could indirectly result in death or serious injury of the patient or operator through incorrect or delayed information or through the action of a care provider), because the motor and pull-back stage is controlled by the software and its failure may cause severe injury to the patients. Thus it is necessary to provide the following information: device hazard analysis, software device hazard, analysis requirements specification (SRS), architecture design chart, software design specification (SDS), traceability analysis, software development environment description, verification and validation documentation and unresolved anomalies. To minimize cost for these complicated analyses and potential risks for patients, attempts to avoid controlling the motor and pull-back stage by software were studied. One approach is to apply erasable programmable read only memory (EPROM).

To ensure the mechanical integrity, the mechanical properties of the commercial catheter were first measured and set as performance standards. Our home-made integrated OCT-IVUS catheter was then modified to fit all these standards.

Electrical safety testing was conducted by a Rigel analyzer. Earthbond, earth leakage, enclosure and patient leakage-F-type were tested (applied parts are those device that contact patients). The intravascular imaging catheter may directly contact with cardiac tissue, thus we tested our imaging catheter following the standards of type CF (direct cardiac application) to ensure its safety. Patient leakage-F-type was tested accordingly: the leakage current of the applied part was measured by applying 110% of mains input voltage to the applied part connectors under short circuit conditions (Figure 26). Note: patient auxiliary current (current between applied parts) is not tested because there is only one applied part in our imaging catheter.
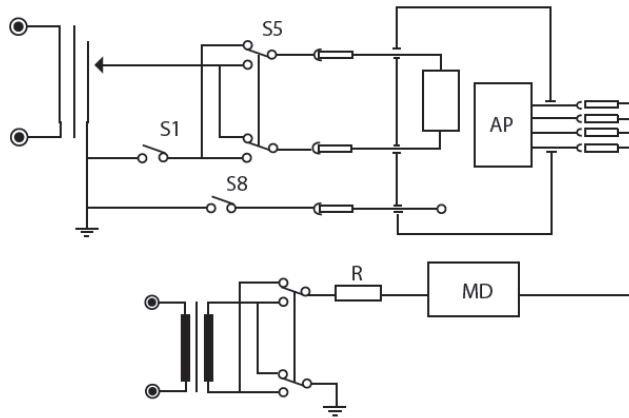
Figure 26 Test circuit for patient leakage-F-type (image copied from "Rigel medical practical guide document")

Preliminary effectiveness of the device, Laser safety and ultrasound safety were performed at UCI and USC.

Biocompatibility testing and sterilization will be performed by a regulation service company and UCI medical center. The following biocompatibility tests will be conducted: 1) cytotoxicity 2) sensitization 3) intracutaneous 4) systemic toxicity 5) hemolysis. Other tests are also suggested and may be tested: complement activation, material mediated pyrogens, thromboplastin time and

thromboresistance. One potential vendor for testing is NAMSA, which is well known company in this field and has assisted many research labs to get FDA approval.

6.3 Summary

To use the integrated system in humans, FDA application is needed. Bench testing, including electrical, mechanical, and laser safety and so on, was conducted to prepare the FDA IDE application. The Pre-IDE application was submitted using the in vivo animal results, bench testing results, and risk management plan.

Chapter 7

Diagnostic accuracy

There are several studies comparing the diagnostic accuracy of IVUS and OCT. The sensitivity/specificity of IVUS based imaging diagnosis and OCT-based imaging diagnosis for calcified plaque, fibrous plaque and lipid-rich plaque in Rieber's (97), Kume's (98), and Kawasaki's (99) papers are listed in Table 4. In general, OCT is superior in differentiating lipid plaque and fibrous plaque (soft tissues) while IVUS is superior in visualizing and characterizing deep tissue components (deeper than 500 μm) as summarized in Table 5. However, all three of these studies expose the natural limitation that the comparison requires offline-fusion of images acquired by separated IVUS and OCT systems. This limitation would not only contribute to the errors caused by inferior co-registration of IVUS and OCT but also reduce the significance of translating these studies to clinical benefits. The purpose of the present study was to investigate the diagnostic accuracy of our integrated IVUS-OCT system and develop clinical objective diagnostic criteria for diagnosing atherosclerosis by combined use of IVUS and OCT.

Table 4 Previous reported diagnostic accuracy of IVUS-only and OCT-only based diagnosis by Rieber's (97), Kume's (98), and Kawasaki's (99).

Sensitivity/ Specificity	Rieber's (94)		Kume's (95)		Kawasaki's (96)	
	IVUS	OCT	IVUS	OCT	IVUS	OCT
Calcified	76%/98%	67%/97%	98%/96%	96%/88%	100%/99%	100%/100%
Fibrous	63%/59%	64%/88%	88%/86%	79%/99%	93%/61%	98%/94%
Lipid-rich	10%/96%	77%/94%	59%/97%	85%/94%	67%/95%	95%/98%

Table 5 The advantages and disadvantages of OCT and IVUS in classifying each type of atherosclerotic plaque

		Calcified	Lipid-rich	Fibrous
OCT	Advantages	Assesses detailed calcification boundary	By optical contrast, provides higher accuracy than IVUS	By optical contrast, provides higher accuracy than IVUS
	Disadvantages	Limited penetration depth: Deep calcification may not be imaged	Limited penetration depth	Limited penetration depth
IVUS	Advantages	Distinguished strong echo signal	NA	NA
	Disadvantages	Acoustic shadow blocks visualization of the entire calcification	Low soft tissue contrast	Low soft tissue contrast and deep fibrous plaque may be interpreted as calcified plaque

7.1 Diagnostic accuracy of the integrated system for human coronary plaque characterization

7.1.1 Methods

7.1.1.1 Specimen preparation

To bring a valuable data to bear on the issue of imaging atherosclerotic plaques, we carefully collected samples from cadavers who died of acute coronary events or were diagnosed with atherosclerosis. A total of 241 regions of interest (ROI) were examined from 175 diseased coronary arterial segments and 20 cadavers (12 females and 8 males, mean age 77 ± 13) up to 48 hours postmortem. After harvesting, the specimens were stored at 4 ^{o}C until imaged with the IVUS-OCT integrated system in warmed phosphate buffered saline (PSB) at room temperature. The study was approved by the Institutional Review Board of the University of California, Irvine.

7.1.1.2 Histology analysis

The imaged artery blocks were marked by a ink mark and needle, and then these blocks were dissected, numbered, fixed with 10% buffered formalin, decalcified in a standard ethylene diaminetetraaceitc acid-4 Na-20% citric acid solution for 10 hours, and then embedded in paraffin. The blocks were finally sectioned to 6 μm-thick slides along the longitudinal pull back axis of artery, and the cross-sections were stained with H&E, Elastic, Trichrome and CD 68 stain. According to the American College of Cardiology clinical standard, these stains would routinely allow for the classification of calcified, fibrous and lipid-rich plaque. All the histological classification were evaluated by a single experienced pathologist (Dr. Correa) blinded to the results of any imaging modalities.

7.1.1.3 OCT-only image and IVUS-only image analysis

We have set a total of 241 regions of interests (ROI: one quadrant of the whole cross-sections) on both the IVUS and OCT images. All IVUS-only diagnosis and OCT-only diagnosis were performed by two cardiologists (Dr. Patel and Dr. Mohar) with random order. OCT-only ROIs and IVUS-only ROIs were classified as calcified, fibrous and lipid-rich by two cardiologists so as to compare the diagnostic results from using IVUS-OCT image pairs later. Cardiologists classified the OCT-only images, blinded to IVUS and histology, and then classified IVUS-only images, blinded to OCT and histology. Using previously established criteria (17, 99, 100), for OCT images, the calcified plaque was defined as signal-poor, intimal-thickening with sharp borders; the lipid-rich plaque was defined as signal-poor, intimal-thickening with diffuse borders; fibrous plaque was defined as a signal-high, intimal-thickening region. In IVUS images, calcified plaque was defined as acoustic shadowing; lipid-rich as intimal thickening with echo density less

than adventitia; fibrous plaque as intimal thickening with echogenicity between lipid and calcification.

7.1.1.4 IVUS-OCT image analysis and diagnosis criteria

Since using different plaque images may influence the sensitivity/specificity result, the same images of IVUS and OCT were used in the experiments before in order to minimize this effect. All IVUS-OCT diagnoses were made by cardiologists, blinded to histology, one week after they first reviewed the IVUS-only and OCT-only images. The IVUS-OCT image pairs were re-sorted in random order to be reviewed by the two cardiologists. Each of 241 IVUS-OCT paired image ROI was also classified as calcified, fibrous or lipid-rich plaque. The objective criteria were established by using a training set composed of IVUS, OCT and histology images pairs from previous publications (99). The existing IVUS diagnostic criteria (101) and OCT diagnosis criteria (102) were also adopted as references to develop this IVUS-OCT diagnostic criteria. IVUS images were mainly used to differentiate between calcified tissue and soft (fibrous and lipid-rich) tissue due to its high sensitivity of identifying calcification and deep imaging depth according to previous reports (97-99). Although OCT is not capable of identifying calcified plaque beyond its shallow imaging depth, it is still able to yield supplementary information on the exact location and size of superficial calcified plaques. The diagnosis loop for the calcified plaque is established by using IVUS as the main determination factor and OCT as the supplementary factor (loop 1). The OCT diagnosis played a decisive role in distinguishing the fibrous and lipid-rich plaque based on its high resolution and relatively higher optical contrast (17, 100). Meanwhile, the IVUS images offer complementary depth information and acoustic contrast to make a secondary supportive evidence for the OCT initial assessment which forms two more loops of criteria for fibrous plaque (loop 2) and lipid rich plaque (loop3). A three-loop

76

structure formed by main determinant and supportive evidence is established by the complementary use of IVUS and OCT, which would hypothetically improve the diagnostic accuracy of these three plaque classifications, especially the lipid-rich plaque.
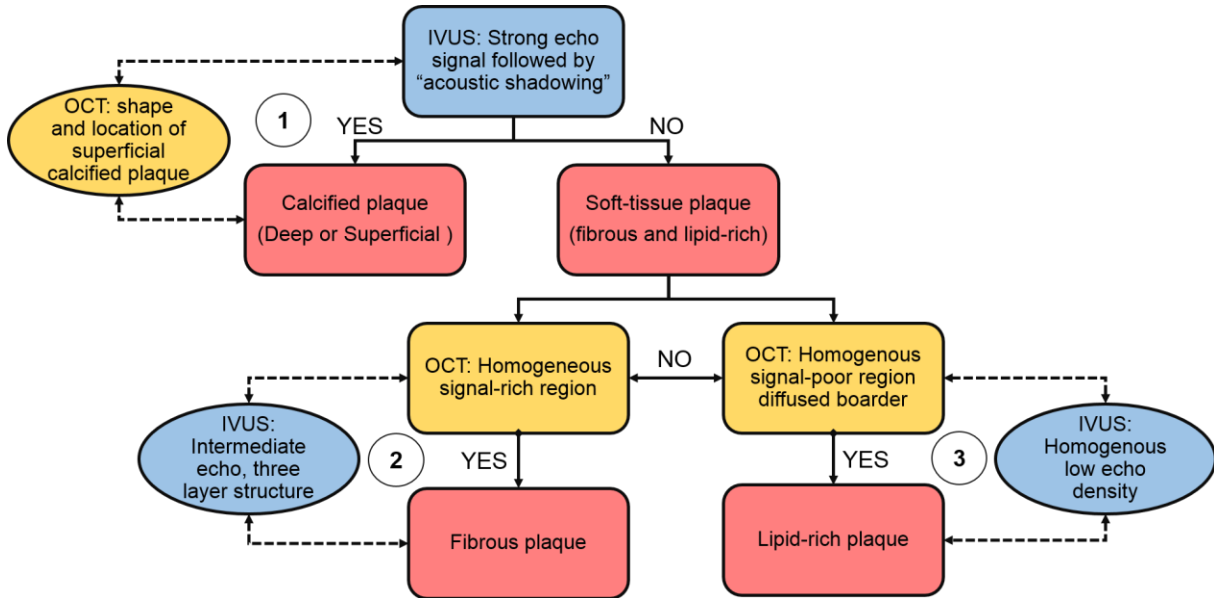
Figure 27 Flow chart for objective diagnostic criteria of IVUS-OCT. Solid arrow with rectangular block represent main determinant path, dashed arrow with elliptic block represent secondary supportive evidence path. By combined use the complementary information of both IVUS and OCT, three loops diagnostic criteria are formed to characterize calcified (loop 1), fibrous (loop 2) and lipid-rich (loop 3) plaques.

7.1.1.5 Statistical analysis

We evaluated the predictive ability of each modality by calculating the sensitivity and specificity of each different imaging technique and comparing the point estimates with 95% confidence intervals. The histopathology diagnoses were set as the "gold standard" for each tissue component. We used ROIs in which the diagnoses made by the two readers were identical. All the numerical data were expressed as the mean ± standard deviation. A p value of 0.05 was considered statistically significant by conducting independent student t-test. We further quantified the agreement between results of each imaging technique and histopathology

diagnoses, and intra-observer variability of each imaging technique by Cohen's κ test for concordance. A Cohen's κ value of 0.61-80 indicates substantial agreement, and 0.81-1 indicates almost perfect agreement. All statistical analyses were performed using commercial software MedCalc for Windows, version 12.5 (MedCalc Software, Ostend, Belgium).

7.1.2 Results

7.1.2.1 Reliability of imaging system

Two physicians who have experience in examining IVUS and OCT intravascular imaging first made the diagnosis based on IVUS-only, OCT-only images and IVUS-OCT paired images for the selected 241 ROIs from the volumetric data blinded to each other's diagnosis, other imaging results and histological results. Only the identical diagnoses between the two cardiologists were used to make the statistical validation of imaging diagnoses compared to the histology results. The IVUS-OCT diagnoses had the perfect overall agreement between the two cardiologists with the Cohen's κ = 0.86 (95% confidence interval (CI) 0.81 to 0.92) and 221 identical diagnoses. The overall agreement between the two cardiologists of OCT-only diagnoses and IVUS-only diagnoses were 0.78 (95% CI 0.71-0.85) and 0.72 (95% CI 0.65-0.80) with the identical diagnoses number of 207 and 200, respectively. As shown in Table 6, the IVUS-OCT diagnoses between the two cardiologists had higher overall agreements and more identical diagnoses than that of OCT-only and IVUS-only diagnoses.

Table 6 Interobserver variability of each imaging diagnosis

Interobserver Variability of IVUS-OCT Diagnosis

	Cardiologist 2			
Cardiologist 1	Calcified	Fibrous	Lipid	Total
Calcified	92	1	1	94
Fibrous	6	101	5	112
Lipid	1	6	28	35
Total	99	108	34	241

Cohen's κ = 0.86(0.81-0.92)

Interobserver Variability of OCT-only Diagnosis

	Cardiologist 2			
Cardiologist 1	Calcified	Fibrous	Lipid	Total
Calcified	76	1	0	77
Fibrous	8	98	14	120
Lipid	9	2	33	44
Total	93	101	47	241

Cohen's κ = 0.78(0.71-0.85)

Interobserver Variability of IVUS-only Diagnosis

	Cardiologist 2			
Cardiologist 1	Calcified	Fibrous	Lipid	Total
Calcified	87	8	4	99
Fibrous	2	98	11	111
Lipid	1	14	16	31
Total	90	120	31	241

Cohen's κ = 0.72(0.65-0.80)

7.1.2.2 Statistical comparison of imaging-based diagnosis compared with histological analysis

As shown in Table 7, within the 221 ROIs where identical diagnoses were made by the two cardiologists, the IVUS-OCT diagnosis had the highest overall agreement with histology diagnosis with the Cohen's $\kappa = 0.96$ (95% CI 0.81 to 0.92). The overall agreement between OCT-only diagnosis and histology diagnosis was 0.91 (95% CI 0.86-0.96) within the 207 ROIs where identical diagnoses were made. The overall agreement between IVUS-only diagnosis and histology diagnosis was lowest ($\kappa = 0.89$, 95% CI 0.83-0.94) within the 200 ROIs where identical diagnoses were made. The lipid-rich plaque was the most misidentified plaque type by using the IVUS-only diagnosis.

Table 7 Overall agreements between the imaging based diagnosis and histological diagnosis

Comparison between IVUS-OCT diagnosis and histological diagnosis				
	Histology			
IVUS-OCT	Calcified	Fibrous	Lipid	Total
Calcified	92	0	0	92
Fibrous	0	97	3	100
Lipid	0	2	27	29
Total	92	99	30	221
Cohen's κ = 0.96(0.93-1.00)				

Interobserver Variability of OCT-only Diagnosis				
	Cardiologist 2			
Cardiologist 1	Calcified	Fibrous	Lipid	Total
Calcified	76	1	0	77
Fibrous	8	98	14	120
Lipid	9	2	33	44
Total	93	101	47	241
Cohen's κ = 0.78(0.71-0.85)				

Comparison between IVUS-only diagnosis and histological diagnosis				
	Histology			
IVUS	Calcified	Fibrous	Lipid	Total
Calcified	85	1	0	86
Fibrous	2	87	9	98
Lipid	0	1	15	16
Total	87	89	24	200
Cohen's κ = 0.89(0.83-0.94)				

7.1.2.3 Diagnostic accuracy of imaging diagnosis

The diagnostic accuracy of each imaging technique is listed in Table 8. The corresponding sensitivity of IVUS-OCT diagnosis for charactering calcified, fibrous and lipid-rich plaque was 100%, 98%, and 90%. The specificity of IVUS-OCT diagnosis was 100%, 97.5% and 98.4%,

respectively. The respective sensitivity of OCT-only diagnosis for charactering calcified, fibrous and lipid-rich plaque was 96.2%, 96.8%, and 84.9%. The specificity of OCT-only diagnosis was 100%, 93.8% and 97.7%, respectively. The sensitivity/specificity of IVUS-only diagnosis were 97.7%/91.1%, 97.8%/90.1% and 62.5%/99.4% for charactering calcified, fibrous and lipid-rich plaque, correspondingly. The histogram in Figure 28 is an alternative representation of diagnosis accuracies of three imaging-based diagnoses for charactering three different plaques. The sensitivity of IVUS-OCT on classifying lipid-rich was statistically higher than that of OCT-only and IVUS-only diagnosis with a p-value less than 0.05. The specificity of IVUS-OCT on classifying fibrous plaques was also statistically higher than that of OCT-only and IVUS-only diagnosis.

Table 8 Diagnostic accuracy (sensitivity and specificity) of IVUS-OCT, OCT-only and IVUS-only imaging diagnosis for characterizing calcified, fibrous and lipid-rich plaques. Data are percentages with 95% confidence intervals.

	IVUS/OCT (n=221)		OCT-only (n=207)		IVUS-only (n=200)	
	Sensitivity	Specificity	Sensitivity	Specificity	Sensitivity	Specificity
Calcified	100.0 (96.3-100.0) n = 92	100.0 (97.2-100.0) n =92	96.2 (89.3-99.2) n = 79	100.0 (97.1-100.0) n =79	97.7 (91.9-99.7) n = 87	99.1 (95.2-99.9) n =87
Fibrous	98.0 (92.9-99.7) n = 99	97.5 (93.0-99.5) n = 99	96.8 (91.0-99.3) n = 95	93.8 (87.5-97.4) n = 95	97.8 (92.1-99.7) n = 89	90.1 (83.0-94.9) n = 89
Lipid-rich	90.0 (73.4-97.8) n=30	98.4 (95.5-99.7) n=30	84.9 (68.1-94.8) n=33	97.7 (94.2-99.4) n=33	62.5 (40.6-81.2) n=24	99.4 (96.9-99.9) n=24
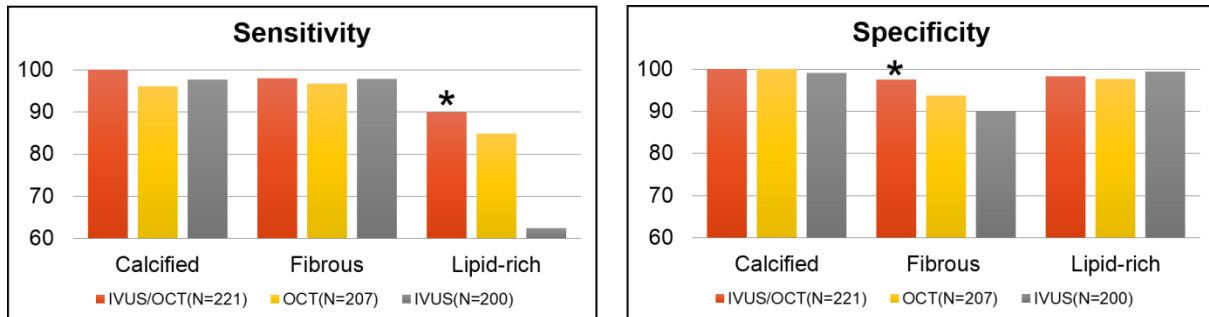
Figure 28 Histograms of sensitivity and specificity of imaging-based diagnosis. *Data statistically different when comparing IVUS-OCT diagnosis to IVUS-only or OCT-only diagnosis.

7.1.3 Discussion

7.1.3.1 Characterization of calcified plaque

Both IVUS-only diagnosis and OCT-only diagnosis demonstrated superior capability of identifying calcified plaque with high sensitivity and specificity in the present study, which was consistent with previous conclusions (10). However, both IVUS and OCT run into problems in providing a full characterization of calcification. As shown in Figure 29, a deep calcified plaque

obviously distinguished by IVUS because of the unique feature of bright echo signal followed by acoustic shadowing. Conversely, due to the limited penetration depth of the infrared light beam, OCT was unable to provide any information on the deeply accumulated calcium, which might lead to a misdiagnosis of calcified plaque to be fibrous plaque. However, for the superficial calcification, strong acoustic shadowing artifacts caused by acoustic impedance difference of calcium and relatively poor resolution made it impossible for IVUS to provide an entire morphological visualization of the calcified plaque, especially the small calcification. On the other hand, OCT outlined the entire boundary of the calcified plaque and targeted the precise location of the small calcification (Figure 30) owing to its high resolution. Therefore, by combing the best features of both techniques while minimizing their respective weaknesses, the IVUS-OCT diagnostic criteria carrying the complementary information from both acoustic and optical contrast are capable of presenting all the major histological features of calcified plaques.

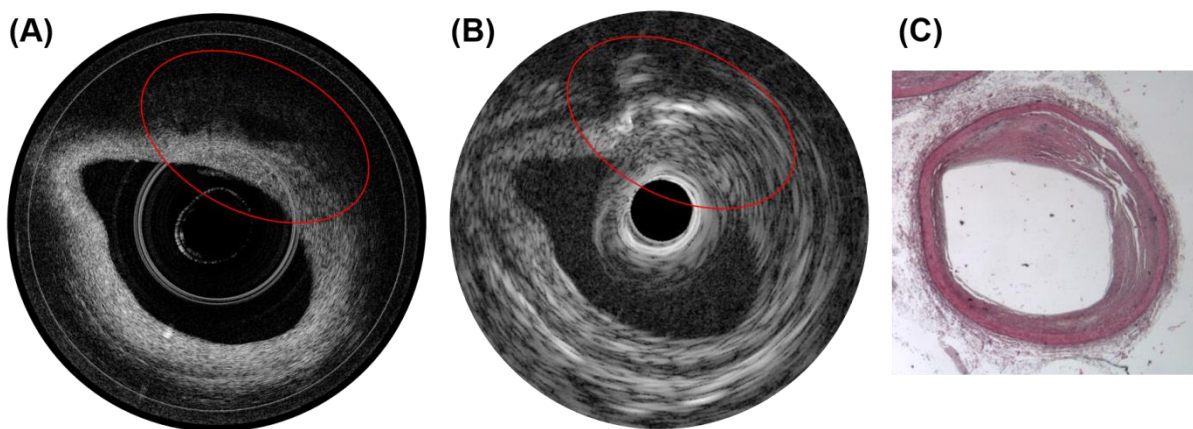Figure 29 Example of deep calcified plaque detection. (a) OCT image: due to limited imaging depth, a deep calcified plaque (within the elliptic ROI) was misdiagnosed to be fibrous plaque by OCT-only diagnosis. (b) IVUS image: a calcified plaque were diagnosed with clear future of bright echo signal followed with acoustic shadow. (c) Histology image (H&E stain) confirmed a deep calcified plaque.
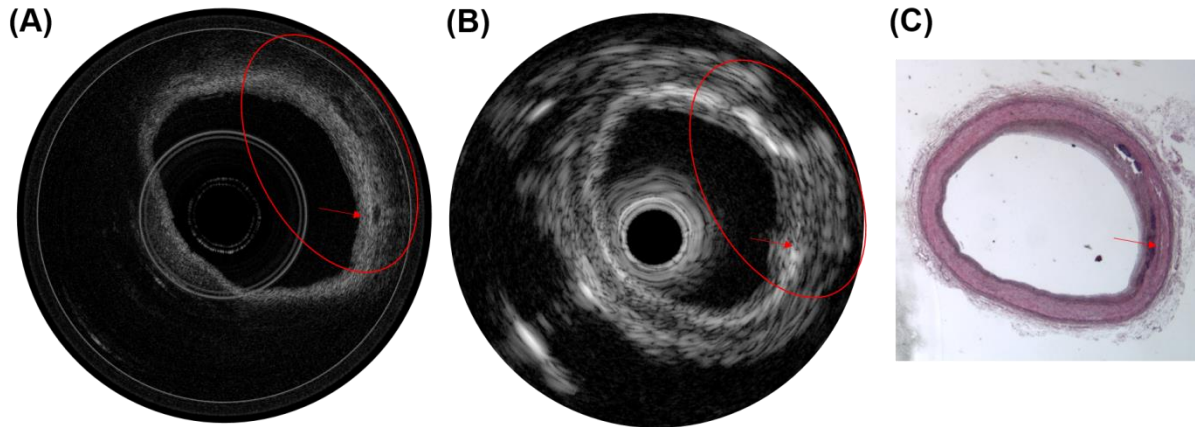
Figure 30 Example of superficial calcified plaque characterization. (a) OCT image: within the ROI, clear boundary and precise location of a large calcified plaque as well as a small calcified plaque (pointed by arrow) were characterized by OCT diagnosis. (b) IVUS image: due to the poor resolution and acoustic shadowing artifacts, the size and shape of the calcified plaques could not be detail characterized. (c) Histology image (H&E stain) confirmed a large calcified plaque and a small calcified plaque within the ROI.

7.1.3.2 Characterization of lipid-rich plaque

According to a previous study (99), a higher frequency transducer (40 MHz) was able to detect intimal lesions more easily than a lower frequency transducer (30 MHz). In the present study, a 45 MHz transducer was used. As a result of the stronger focusing characteristics of higher frequency acoustic beams, a 45 MHz transducer enables higher axial resolution and a more limited focal zone. This strength is comprised by downgrading the lateral resolution and detection sensitivity beyond the focal zone, which made the position of transducer inside the artery becoming an influential factor for IVUS diagnosis. For example, as shown in Figure 31, an accumulated lipid deposit was confirmed with histological results, and the position of this lipid-rich ROI was relatively farther away from the transducer. A false negative case of lipid-rich plaque diagnosis based on IVUS-only was produced due to insufficient resolution and sensitivity. However, using the OCT image as the reference, a slightly larger echolucent region compared with an adjacent media layer allows it to be interpolated to serve as the secondary supportive

verification in the IVUS-OCT diagnostic criteria. Past data have attributed that false-negative OCT diagnosis of lipid-rich plaque to the limited penetration depth of OCT, causing some thick-capped, large lipid pools to be misinterpreted as fibrous plaque (100) as the example shown in Figure 32. However, by adding the complementary depth information of IVUS, this false-negative diagnosis can be eliminated in the IVUS-OCT diagnosis criteria. Meanwhile, the specificity of charactering fibrous plaque was also slightly improved since this type of false-positive diagnosis of fibrous plaque was reduced. Therefore, the present study not only supports the previous report that OCT diagnosis could detect lipid-rich plaque more accurately than IVUS diagnosis, but also demonstrates the objective IVUS-OCT diagnostic criteria could further increase the sensitivity of differentiating lipid-rich plaque with statistically significance.
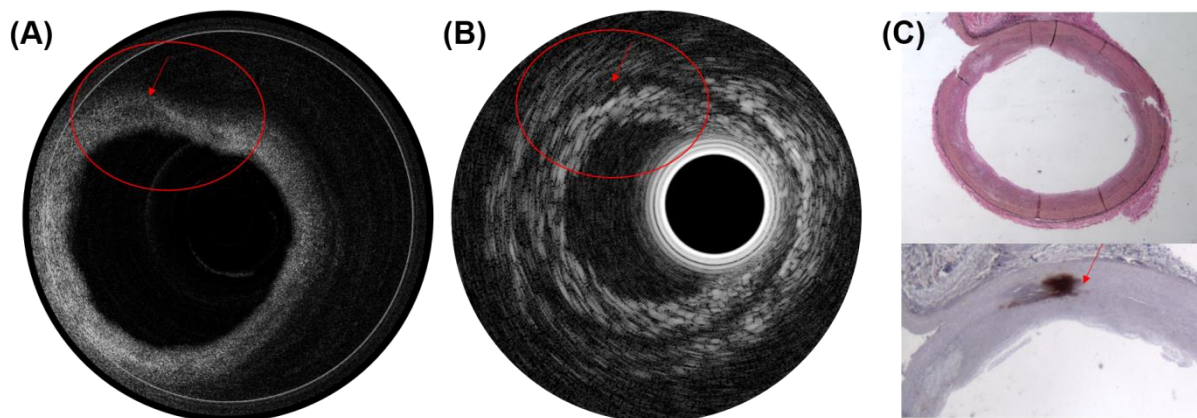
Figure 31 Example of discrepancy between the OCT and IVUS on lipid-rich plaque diagnosis. (a) OCT image: a lipid rich plaque was detected by OCT as a diffused boarded, signal-poor regions with overlying signal-rich bands. (b) IVUS image: a false negative case of same lipid-rich plaque by IVUS-only diagnose to be fibrous plaque. Referenced by OCT image, a corresponding region of signal-poor characteristic was interpolated to be the supportive evidence in IVUS-OCT diagnosis. (c) Histology images: Top image (H&E stain) and bottom image (highly magnified image of CD68 stain).
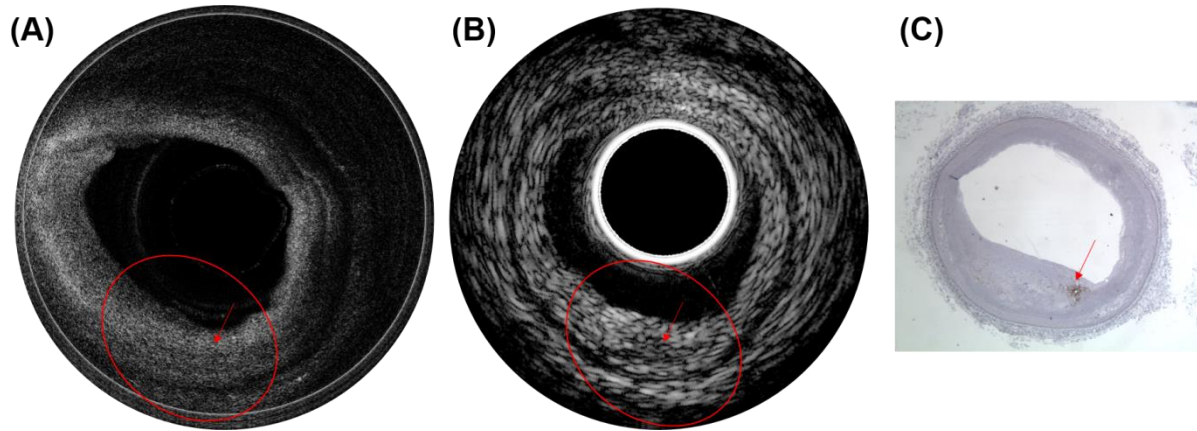
Figure 32 Example of a false-negative diagnosis of lipid-rich plaque by OCT-only diagnosis. (a) OCT image: a lipid-rich plaque was misdiagnosed as fibrous plaque by OCT-only diagnosis. (b) IVUS image: a region homogenous low echo-density region was shown (pointed by the arrow), but the lipid-rich plaque still could not be clearly discriminated without using OCT as a reference. (c) Histology image (CD 68 Stain).

7.1.3.3 Discrimination of fibrous plaque

In previous studies (98, 99), both OCT and IVUS demonstrated high diagnostic accuracy for charactering fibrous plaques, which were supported by our present data. In the present study, all of the false-negative diagnosis cases of fibrous plaques were linked to the false-positive of lipid-rich plaques in IVUS-OCT diagnosis and OCT-only diagnosis except for IVUS diagnosis. According to Yabushita (100), this type of plaque often contains a dominate amount of fibrous component and a small amount of lipid distribution. As shown in Figure 33, the IVUS images offered the strong evidence of fibrous plaque with overall intimal thickening. In spite of this, like the OCT-only diagnosis, the IVUS-OCT diagnosis still misclassifies this ROI as a lipid-rich plaque because OCT characteristics served as the major determinant in differentiating fibrous and lipid-rich plaque in the OCT-IVUS diagnosis criteria. As a result, the current IVUS-OCT diagnostic criteria should be further modified to add more classification features in differentiating clinically relevant significant and insignificant lipid accumulations.
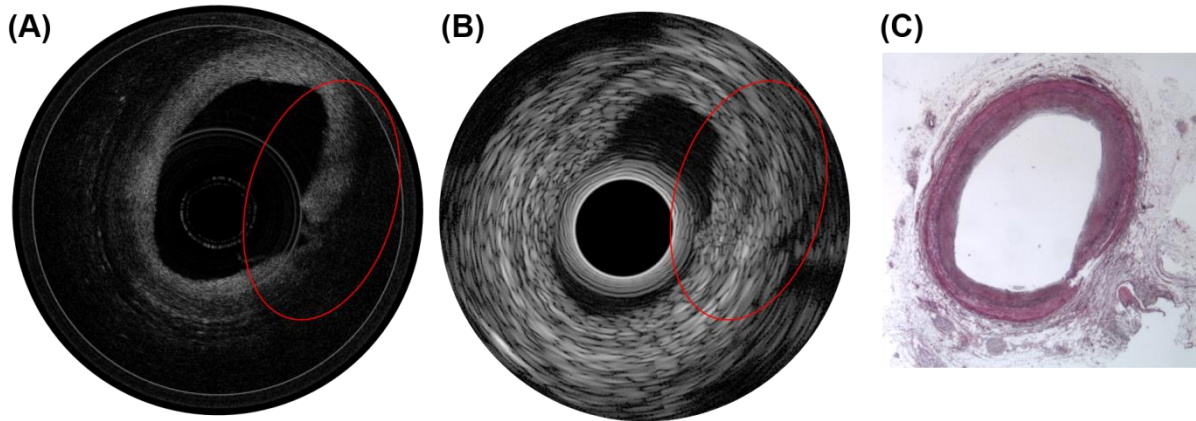
Figure 33 Example of false-negative IVUS-OCT diagnosis of fibrous plaque within overall intimal thickening. (a) OCT image: ROI was misdiagnosed as lipid-rich plaque by OCT-only, and IVUS-OCT diagnosis since OCT served as the major diagnostic factor. (b) IVUS image: whole three-layer structure with overall intimal thickening were visualized by IVUS image. (c) Histology image (H&E stain).

7.1.4 Limitations

There are several limitations associated with this study that makes it difficult to allow our finding to be used directly in a clinical setting. First, even though the imaging processes were performed within 48 hours postmortem, the specimen degradation caused by artery tissue changes was not evaluated in this study, which was a natural limitation by using cadaver specimens. Second, different from clinical settings, the flow of PBS through the arteries and physiological pressure were not maintained in the present study. Third, although we eliminated most histology images with tissue-fold or stain artifacts, histology processes may cause some artifacts, such as changes of luminal area. The slice thickness of histology is 6 μm, where OCT lateral resolution is 30 μm and IVUS 200 μm. This difference may cause imperfect matches for IVUS-OCT and corresponding histology images and thus may affect the result. Fourth, even though the testing probe enables the auto co-registration of IVUS and OCT images within one image frame, the transducer and OCT probe's position and angle to the plaque may also affect the accuracy of the

diagnoses. Finally, the selected ROI were simply classified into calcified, fibrous and lipid plaques, while the heterogeneity of atherosclerotic plaque composed of variously complex tissue components was not fully considered. Therefore, IVUS-OCT diagnostic criteria should be modified further to include additional classification features for differentiating plaque components, especially the lipid pools and insignificant lipid accumulation in fibrous tissue dominant plaque. We have imaged 241 ROI; but for lipid-rich plaque, we have only imaged 36 ROI in total due to the limited access to younger patients' coronary arteries. Further studies, with a larger sample set and in vivo clinical imaging, will be required to provide a more accurate sensitivity/specificity assessment of this system with higher statistical significance for identifying each plaque types and TCFA.

7.1.5 Summary

We reported the diagnostic accuracy comparison of IVUS-OCT diagnosis, with IVUS-only diagnosis and OCT-only diagnosis based on the fully integrated IVUS-OCT system and hybrid catheter. It is concluded that the use of IVUS and OCT is superior to IVUS-only and OCT-only diagnosis for detection and characterization of coronary atherosclerotic plaques with high degree of sensitivity and specificity. We also developed, in detail, the objective IVUS-OCT diagnostic criteria based on the unique complementary nature of these two imaging modalities. The present finds suggested the fully integrated IVUS and OCT system holds great promise for improving diagnosis of atherosclerosis and translating into clinical benefit.

7.2 Imaging of vulnerable plaques

To investigate the capability of recognition of vulnerable plaques using this IVUS-OCT technology, we imaged 50 human coronary arteries in vitro and characterized the plaques.

Examples are shown in Figure 34. TCFA and false TCFA can be differentiated using IVUS-OCT images (Figure 34 Ia, Ib, IIa, IIb, IIIa and IIIb). Corresponding histology photos (Figure 34 Ic, IIc and IIIc), where the positive CD 68 stain regions confirmed the existence of macrophages and necrotic cores, validated the diagnosis based on IVUS-OCT images. Cross-sectional OCT (Figure 34 Ia) and IVUS (Figure 34 Ib) images clearly demonstrate complementary information about the coronary artery wall. OCT allows for recognition of the thin cap feature, which is not seen in the IVUS image, thanks to its high spatial resolution. IVUS detects the presence of an echolucent region, representing the necrotic core ("NC" in Figure 34 Ib). In Figure 34 II, physicians diagnosed this ROI as TCFA when only reading the IVUS image. This misdiagnosis was caused by the insufficient resolution and sensitivity of IVUS. However, using the OCT image as reference (see Figure 34 IIa), a signal low region with a diffuse boundary (lipid plaque) could be visualized, and the thickness of the signal high region (fibrous cap) could be measured to be greater than 150 μm. In Figure 34 III, physicians diagnosed this ROI as TCFA when only reading the OCT image. Macrophages accumulated in the intimal surface created a TCFA-like image. This misdiagnosis was caused by OCT's limited penetration depth. However, using the IVUS image as reference (see Figure 34 IIIb), no underlying necrotic core can be found.
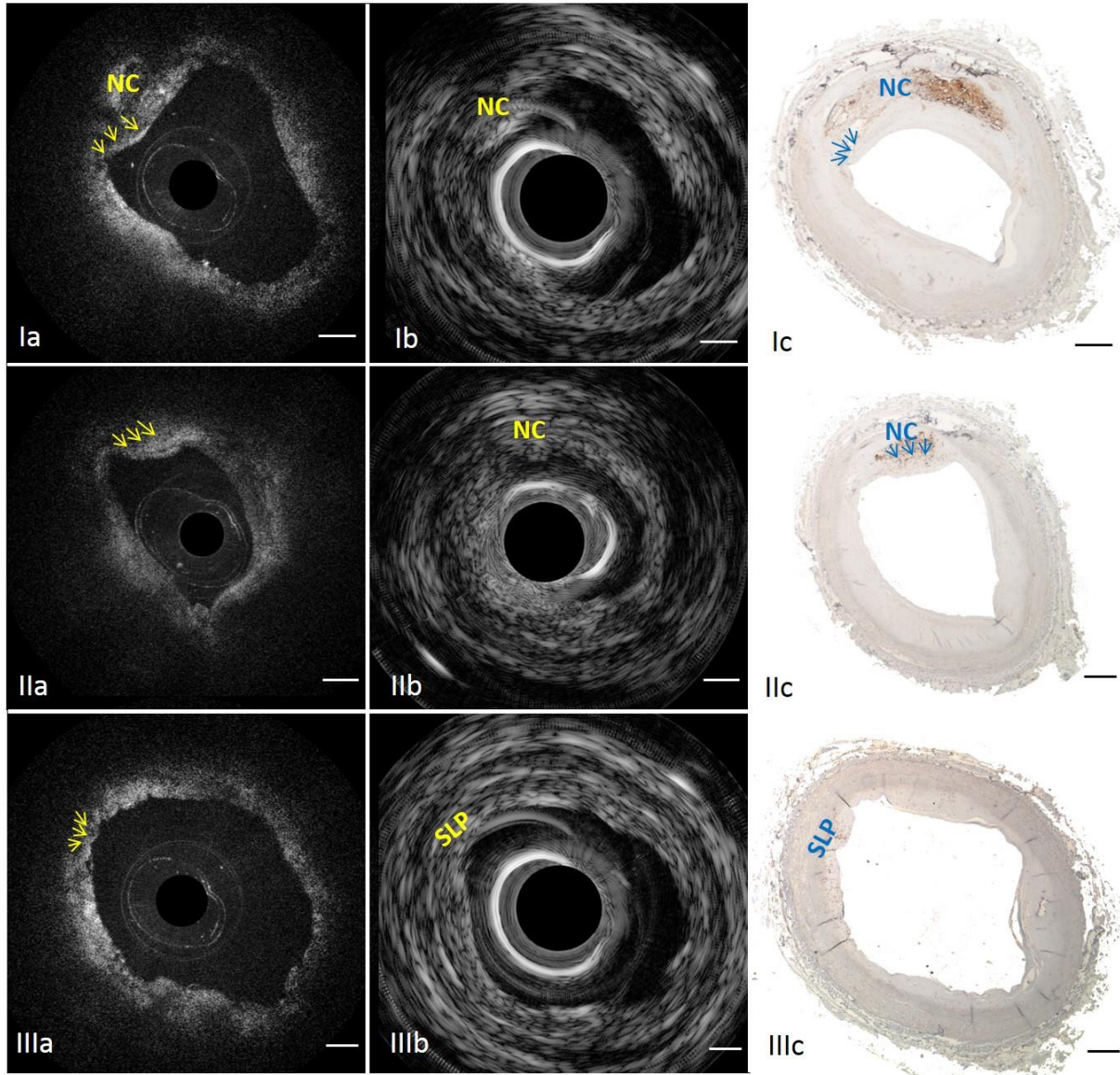
Figure 34 Characterizing human atherosclerotic plaques by the ultrafast IVUS-OCT system. First row: Example of a TCFA. (Ia) OCT image in which arrows point at the fibrous cap; (Ib) corresponding IVUS image indicates the location of necrotic core; (Ic) photo of the corresponding histology slide with CD 68 stain, highlighting macrophages and necrotic core. Middle row: A false positive case of TCFA diagnosis based on IVUS-only (IIb) was produced due to the insufficient resolution and sensitivity. Size of the thick cap can be determined by the corresponding OCT (IIa) and CD 68 histology (IIc). Bottom row: A false positive case of TCFA diagnosis based on OCT-only (IIIa) was produced due to OCT's limited penetration depth. A small lipid pool can be determined by IVUS (IIIb) and CD 68 histology (IIIc). Arrows denote the fibrous cap. NC: necrotic core; SLP: small lipid pool. Scale bar: 0.5mm.

7.3 Post processing

Since OCT-IVUS requires real-time imaging and displaying, very little processing is used to ensure a high speed of data processing. As for IVUS data, Hilbert transform, log and polar transform are needed. As for OCT, k-t transform, FFT, log and polar transform are needed.

Once the area of interest is found, such as a plaque region which needs to be classified, we use some simple postprocessing methods to increase signal to noise contrast. By doing this, we can display IVUS-OCT images more clearly to physicians and make the characterization of plaque components (see Chapter 7.1) easier.

Matlab has several powerful and easy-to-use functions for imaging processing. Thus, I use Matlab to post process image in our research.

1. Simple average is often used in OCT (40). Averaging 2 or 3 images is what usually used, but using more than 3 images will also make the processed image very blurred. For OCT images acquired by rotating probe, averaging 2 to 3 images instead of averaging adjacent A-lines can only be used when the probe is pulled back very slowly and also images are not suffering from non-uniform rotation distortion (NURD).

2. Median filter is relatively better than simple averaging in terms of avoiding blurring. "medfilt2(A, [m n])" function can be used for 2-D image filtering.

    Because OCT-IVUS uses two modalities simultaneously, some integrated probes have good quality for OCT but not IVUS and verse vice. In cases like this, we have to compromise by choosing a relative high quality probe and doing more post-processing for the "bad-quality" modality image. For a bad-quality image, either averaging or a median filter could be used to improve image quality (see Figure 35).

92
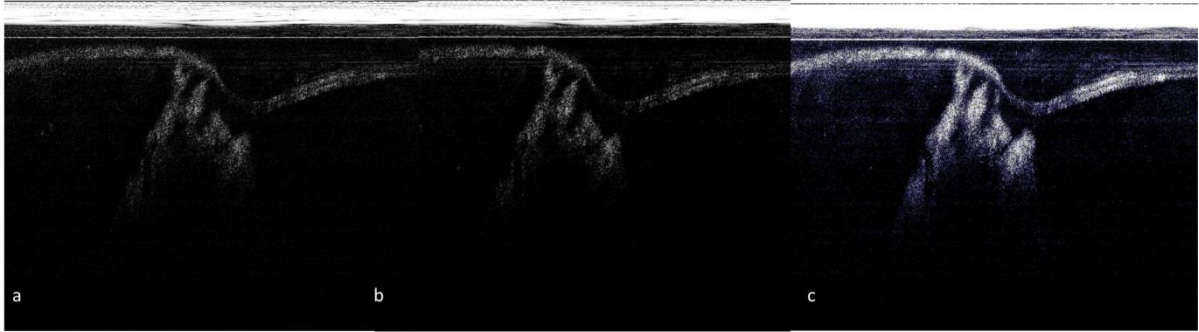
Figure 35 (a) original image (b) image after 2D median filter (c) image after averaging three adjacent images

3. If a median filter or averaging is making the image blurred a lot, sharpening the image using "imsharpen" function can help. Sharpening can enhance the image by emphasizing edges. Figure 36 shows an example of the effect of sharpening. The cap region is clearer after post-processing.
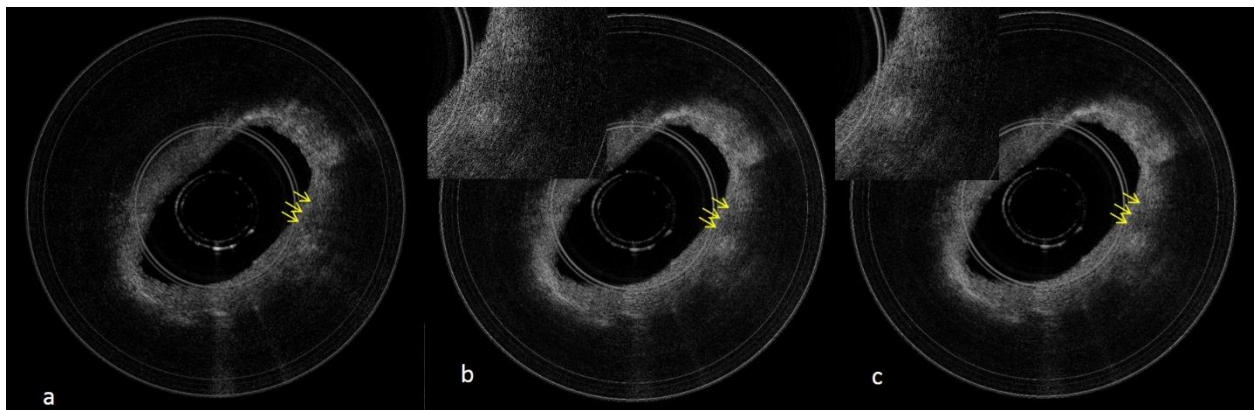
Figure 36 (a) original image (b) image after averaging and sharpening. Inset: zoom in image of the cap region. The cap is more obvious after post-processing (c) image only after averaging. Inset: zoom in image of the cap region. Blurring is seen in the image.

7.4 Summary

Quantitative evaluation of the diagnostic accuracy of the integrated system was performed. In vitro imaging of cadaver coronary specimens demonstrates that by combining the best features of both IVUS and OCT while compensating for their respective weaknesses, combined use of

IVUS-OCT diagnosis has a higher diagnostic accuracy for atherosclerotic plaque characterization. The overall agreement between IVUS-OCT and histology diagnoses was excellent. Images of TCFA and false TCFA were also obtained and analyzed. Simple but time-efficient post-processing methods were also presented.

Chapter 8

Other applications for the IVUS-OCT system

8.1 Stent imaging

Malposition and Neointimal coverage of stent struts are of great concern for interventional cardiologists. Stent underexpansion and incomplete reendothelialization play important roles in the pathogenesis of stent thrombosis. IVUS is commonly used during stent implantation. Intravascular OCT has recently received widespread attention because of its superior resolution. Here we provide a tool that enables real-time co-registered OCT-IVUS functions. The three dimensional (3D) imaging of coronary stents within these cadaver coronary arteries, obtained by an integrated OCT-IVUS system, is presented. Several examples of stent apposition and stent asymmetry detected by IVUS or OCT are compared. The complimentary capability of the integrated OCT-IVUS system is demonstrated.

8.1.1 Motivation

Atherosclerotic vascular disease is the No.1 cause of death worldwide. Stenting is one of the most common treatments for server atherosclerotic lesions. Intravascular imaging tools are usually needed to evaluate stent position and avoid in-stent thrombosis and other deadly side effects of stenting (103).

Intravascular ultrasound (IVUS) is the most commonly used intravascular imaging tool and it has been used for 20 years. However, IVUS, with its limited resolution, cannot visualize endothelial coverage post-stenting, an important predictor for in-stent thrombosis. In contrast, OCT meets this need due to its superior resolution capability, though at the expense of penetration depth. A

multicenter study (104) and several controlled studies (105-107) demonstrated the clinical significance of OCT for evaluation of stenting: OCT-identified suboptimal stent positions is a cause of acute stent thrombosis.

Considering the strength and limitation of OCT and IVUS in imaging stents, it is natural to attempt to combine the use of OCT and IVUS for better guiding of stent implantation. Researchers have been working on designs for an integrated IVUS OCT technique for the past several years, but no result of OCT-IVUS in stenting has been published. Here we use a previously developed IVUS-OCT system for imaging coronary stenting. We showed that stent-tissue microstructure visualization can be provided with this integrated system.

8.1.2 Methods

To ensure the elasticity of sample best mimic artery in vivo, we used a fresh human cadaver coronary artery segment, 48 hours post mortem. A stent (Jostent graftmaster, 4.5mm-16mm long, by Abbott laboratories) is implanted in the segment by an inflation device (Merit medical system inc.).

8.1.3 Result

Co-registered OCT-IVUS Imaging is performed using the integrated system at 10 frames per second, 1000-A-line per frame. Representative pairs of incomplete stent apposition and irregular strut separation are show in Figure 37. These two features, especially incomplete stent apposition which is responsible for stent thrombosis and acute cardiac death, are of great clinical importance. Images of stent obtained by ball lens probe design, where artifact lines are avoid, are shown in Figure 37 (e) and (f). Figure 37 (g) is its 3D reconstruction.
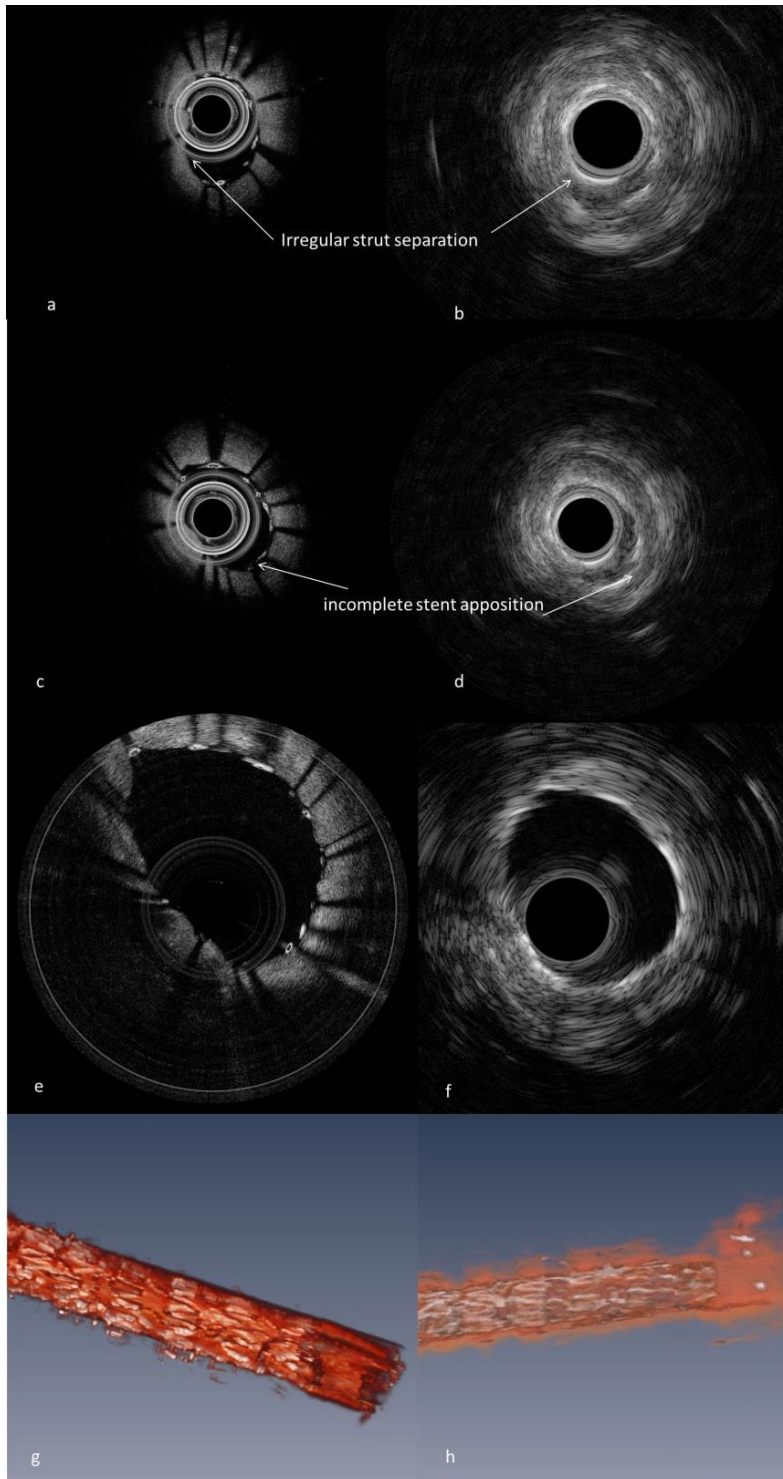
Figure 37 Stent irregular spacing between adjacent struts can be visualized by (a) OCT (b) IVUS. (c) At 7 o'clock the stent is under deployed by 100 µm. This small feature is obvious in the corresponding IVUS image (d). Representative pair of OCT (e) IVUS (f) imaging using ball lens OCT probe design to reduce artifact lines' intensity. (g) 3D rendering of a human coronary artery specimen with a stent. The white color coded places are stent struts and the red coded places are coronary artery tissue.

8.1.4 Discussion and future directions

The integrated OCT-IVUS system is promising for evaluation of important stent-tissue microstructure information because of its high resolution and deep tissue penetration depth. Incomplete stent coverage and in-stent neointima are clinically significant predictors for late stent thrombosis and sudden coronary deaths (105, 108). IVUS is a standard technique to evaluate tissue response after stent implantation. The novel integrated system that we propose enables full 3D visualization of the stent structure and these predictors with higher resolution; thus, a potentially higher predictive accuracy may be expected than using IVUS alone.

Apart from its long term usage in routine stenting procedure, the integrated OCT-IVUS system also provides a tool that allows cardiologists to compare OCT with IVUS. Commercialized Intravascular OCT has only received FDA approval for four years and just started to be used more frequently in US hospitals. Standards, especially a quantitative threshold for optical stent positioning, have not been established yet. The clinical relevance of the findings requires further research. By using OCT-IVUS images obtained by the integrated auto co-registered OCT-IVUS system (46), interventional cardiologist can adopt already-established IVUS standards to OCT, which will expedite the process of the OCT implementation in stenting.

8.1.5 Summary

Three dimensional (3D) imaging of coronary stents within cadaver coronary arteries was performed. A long image range catheter using a 2.3 mm-working-distance ball lens was developed to image a large artery and avoid ghost reflections.

8.2 Bile duct imaging

8.2.1 Significance

Gastrointestinal (GI) cancers cause more than 140,000 deaths with more than 290,000 new cases in the United States in 2014. Specifically, cholangiocarcinoma (CCA) of the bile duct is the second most common primary hepatic malignancy in the United States with more than 2,500 new cases diagnosed each year. Advanced CCA is deadly and early diagnosis of CCA is essential to prevent death. The most common diagnostic method for CCA is brush cytology, where biopsy is done without the guidance of any catheter. As a result, some malignant cells are not collected by random scraping. The sensitivity of this method is only around 50%; accordingly, half of the patients with CCA may receive a false negative diagnosis and thus not receive on-time treatment. The 5 year survival rate of advanced staged CCA is less than 5%. Accordingly, timely treatment and early detection is very critical for saving CCA patients' lives. Intraductal imaging methods, such as US, have shown high diagnosis sensitivity and specificity for CCA (109, 110). OCT has also been used in vivo during endoscopic retrograde cholangiopancreatography (ERCP) and is able to visualize the biliary tree duct (111, 112) with 10 times better resolution than US. However, the penetration depth of OCT is only ~1 mm, which is not enough for detecting deep tumor margin. The combined use of these two complementary imaging techniques could provide capability for cancer staging (high penetration depth by US) and early detection (high resolution by OCT). US will be used for staging tumors, according to the size of the primary tumor and whether it has invaded lymph nodes and other parts of the body. OCT is for visualizing detailed information, such as dysplasia and neoplasia, for early detection of tumors. Thus, we proposed to use the miniature integrated US-OCT catheter to guide biopsy to improve the diagnostic accuracy of CCA.

8.2.2 Methods and Materials

8.2.2.1 Long range OCT system

The size of the common bile duct (CBD) varies from person to person. The common bile duct may have any diameter reading between 2 mm and 15 mm and be normal. There is about a 4% chance of having an ID of less than 4 mm, about a 10% chance of having an ID of 4 mm-6 mm, about a 30% chance of having an ID of 6 mm-8 mm, about a 30% chance of having an ID of 8 mm-10 mm, and about a 26% chance of having an ID of more than 10 mm.

Since more than 80% of people have a CBD with an ID over 6mm, a long image range OCT system is needed for GI imaging.

The Santec laser that we used for intravascular imaging has a coherent length of 10 mm. The detector in an OCT system only acquires real signals but not complex signals. After FFT, complex signals are generated. The real half and image half are mirror images of each other, as shown in Figure 38 (a). To keep our system compact, simple and without inducing extra noise, we did not add any extra components (113, 114) in the OCT system for solving the complex conjugate ambiguity. Instead, only the real half of the image is used. Thus, the effective coherent length for this laser is 5mm. To achieve long range imaging easily, we used a different laser (with a measured coherence length of 41.2 mm, i.e. 4 times that of the old laser) in the bile duct imaging system. With this laser, our system can achieve effective image range of 20 mm.

image

real

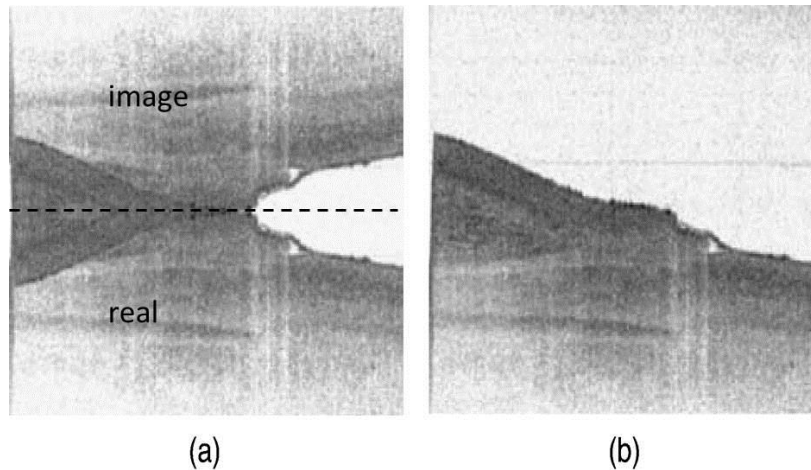(a)   (b)

Figure 38 Image before (a) and after (b) solving the complex conjugate ambiguity (113)

To facilitate the safe and convenient use of the OCT-IVUS system in hospitals, the previously published IVUS-OCT system (42) was modified and made more compact. The fiber-based interferometer and the 1310 nm swept-source laser was enclosed in the same case and pull back sub-system was enclosed in a different case (Figure 39 and Figure 40). By this design, most moving parts and cables are not exposed to live animals or patients, which provide a safer operation environment for interventional cardiologists. Figure 40 is the photo of pull back sub-system. The inner content of the sub-system box is pulled out for demonstration. The pullback console consists of a rotational part, a pull-back stage, a cable carrier and cables. During the experiment, a motor rotates the rotary joint through belt transmission. Pull-back is achieved by a motorized linear stage. The cable carrier (orange arrow in Figure 40 (a)) is used to protect fiber, BNC and power cables while the stage pulls back the motor and rotary joint. A SMA connector (orange arrowhead in Figure 40 (a)), through which the ultrasound signal transmits from probe to the pulser/receiver, was mounted on a bracket. The entire pull-back box was designed in Solidworks software (Figure 41) and then made by a machine shop, according to the drawings I designed. On the back panel of the pull-back box, a power supply connector [the arrowhead in Figure 40 (b)] and a FC/APC fiber connector [the arrow in (b)] were mounted. 15 V DC power

supplies the pull-back linear stage and the rotational motor, through the circular panel-mount power-supply connector. An optic fiber jumper coming from the sample arm in the OCT system is connected to the fiber connector. Two DB9 serial ports were used for transmitting the signal of the linear stage and the motor, respectively.
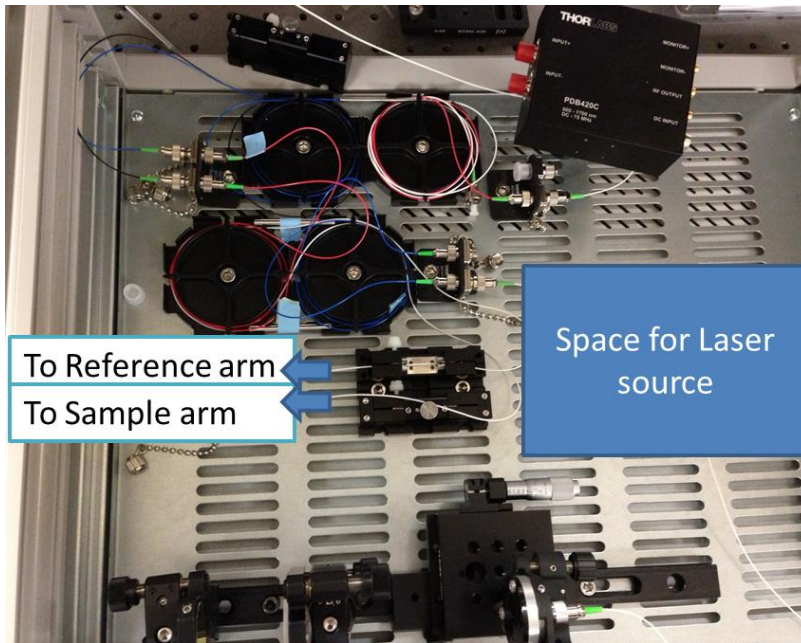
Figure 39 OCT system in box
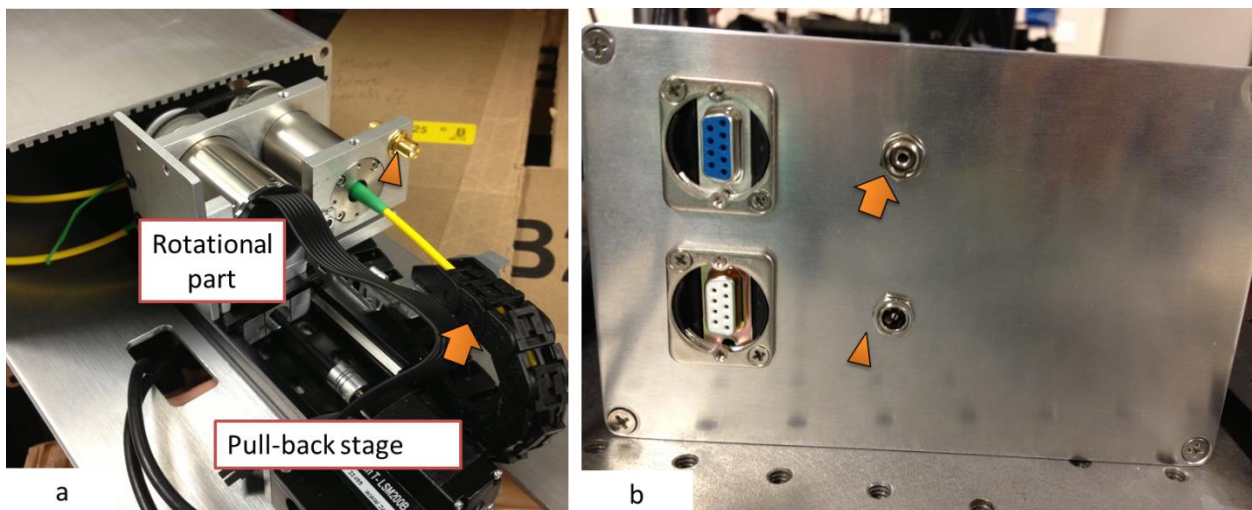
Figure 40 Pull-back device (a) internal design (b) back panel
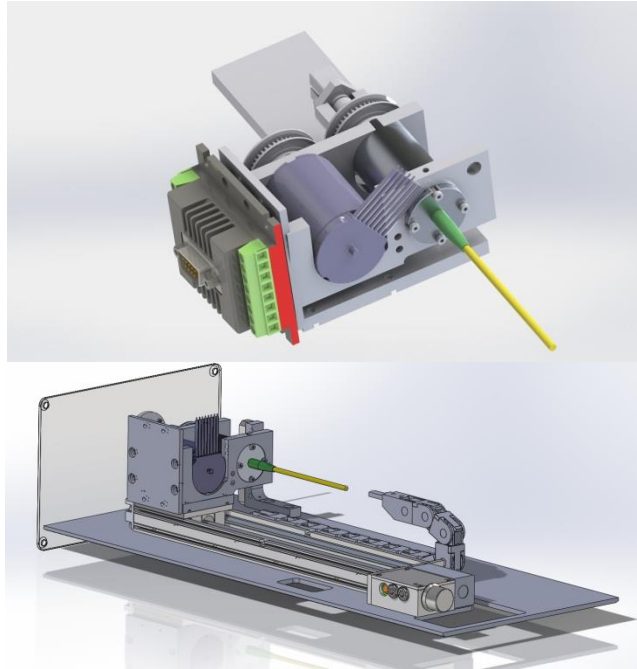
Figure 41 Solid work designed pull-back stage

8.2.2.2 Catheter design

After the OCT probe and US transducer were made separately, they were aligned back-to-back (46) and fixed inside a metal cap. Here, back-to-back design means the sound and light exit at the same axial location and are 180-degree apart. This design ensures that the catheter is very flexible and can be easily delivered into bile duct. Torque coil was then added to protect the electrical wire and optical fiber and thus completed the integrated OCT-US imaging coil. During procedures, the imaging coil will be inserted into a catheter sheath (with a single balloon), which fits in the accessory channel of a duodenoscope. Single balloon design will be used for positioning the imaging probe in the center of the lumen and enable stable rotation (115). Saline will be filled inside the catheter sheath and balloon for ultrasound coupling and reducing optical aberration and reflections. The catheter will be delivered into the duodenum by the duodenoscope and then navigated into the bile duct by the elevator of the duodenoscope.
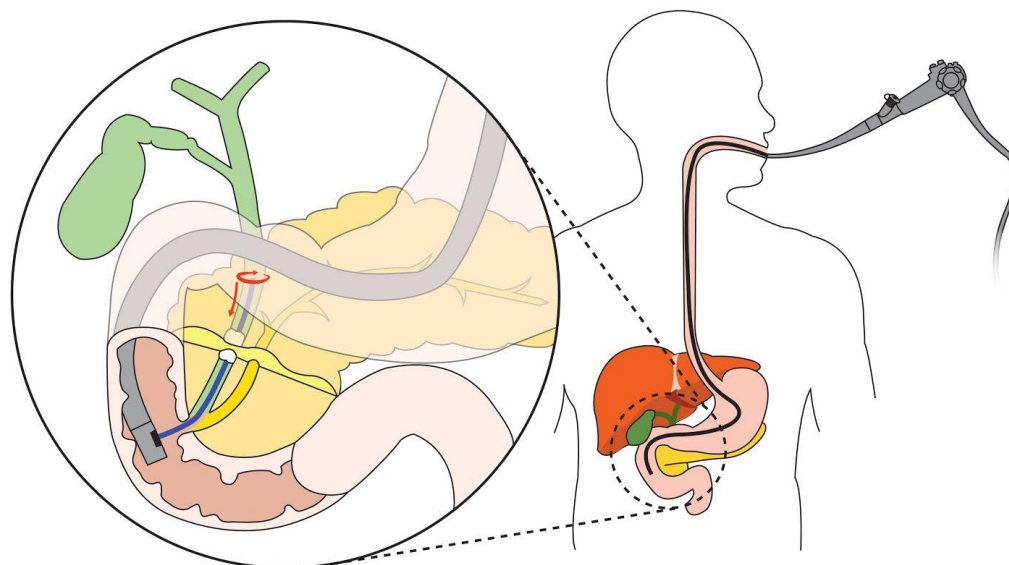
Figure 42 Schematic describes the procedure of dual-modality bile/pancreatic duct imaging.

8.2.3 Results

We first imaged a 10 mm-long healthy common bile duct sample (inner diameter, 6-15mm) with a wire phantom at the side, Figure 43 (b). Our long range OCT system was able to reveal the inner surface of the bile duct but couldn't penetrate deep enough to image the outer contour of the bile duct and the wire phantom. However, the US system, though with very low resolution, provided visualization of the sample beyond 1mm.
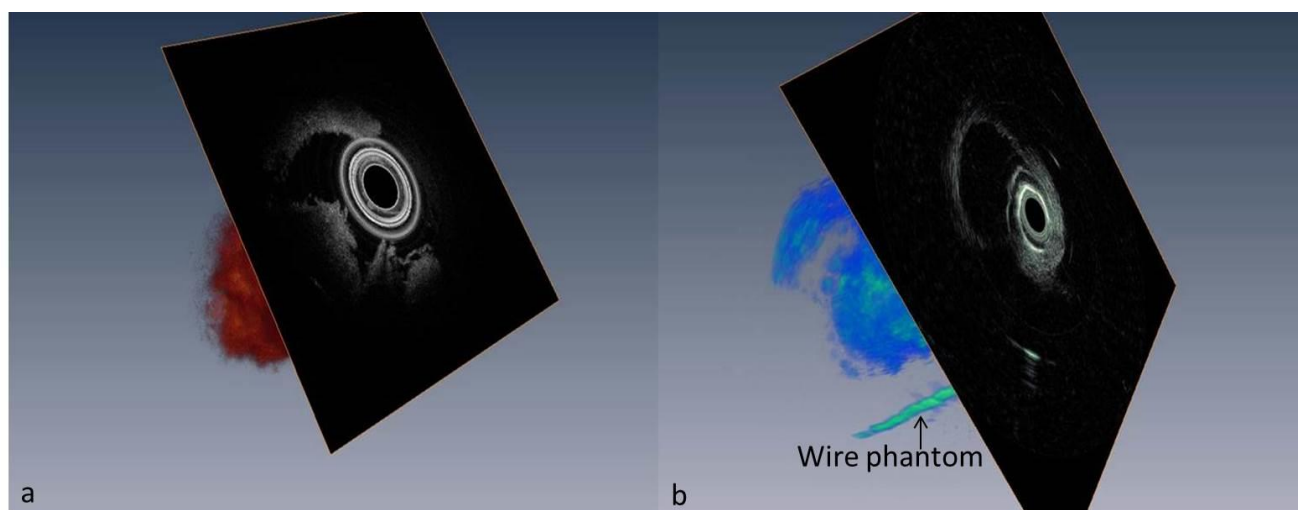
Figure 43 3D reconstructions of OCT-US images of a bile duct: (a) OCT (b) US images.

We also imaged a cadaver CCA sample, see Figure 44. Subverted epithelial cell structure, which gives a heterogeneous back-scattered signal in the OCT image, demonstrated the existence of a tumor (116). Micro-calcification, a sign of mutated liver cells, can be observed in the corresponding US image.
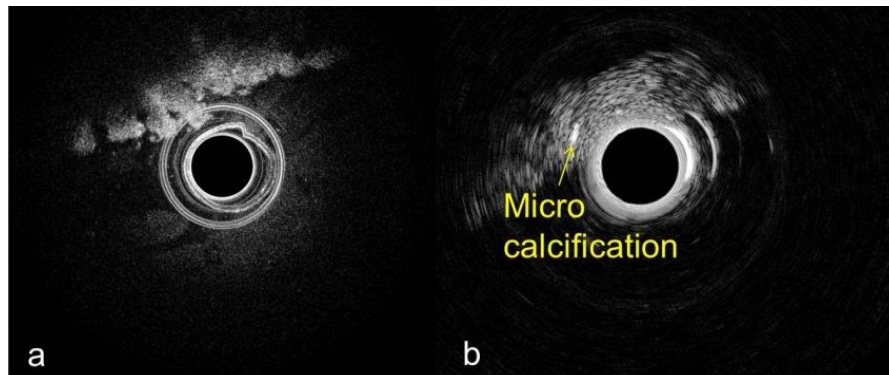
Figure 44 OCT-US images of a CCA sample: (a) OCT image, (b) US image.

8.2.4 Summary

Our integrated system and catheter are capable of imaging the full range of the bile duct and providing detailed visualization of epithelial cells. Ex vivo imaging of a healthy bile duct and CCA sample was successfully performed. These two imaging modalities provide complementary and important information for accurate detection of malignant tissue.

One of the future directions is catheter development, which is similar to the development of IVUS-OCT catheter described in Chapter 4. But this will also focus on providing enough mechanical strength to make the probe go through the duodenoscope channel without breaking optical or electrical sensors. After this catheter is well developed to fit well with clinical standard procedures, we will start in vivo animal experiments to validate the clinical adaptability of our technology.

Another future direction of this research is clinical study, where we will image the biopsied tissue before the tissue is sent for pathological analysis. The image-guided diagnosis will be compared with histopathological diagnosis.

Chapter 9

Self-tracking probe

9.1 Motivation

Inspired by the idea of endoscopy, OCT broadens its application from the surface, eye (117, 118) and skin (119, 120) , into body cavities, such as the vascular network, pulmonary airway and gastrointestinal tract (121). By longitudinally scanning the probe beam, OCT can provide a series of images and quantitative measurements for these inner-body structures. However, sometimes the true 3D anatomy is necessary for diagnosis (122, 123). There are a couple of papers reporting endoscope camera 3D motion reconstruction methods (124, 125). Unfortunately, due to the cross-sectional view characteristic of OCT images, previously reported methods are not applicable for an OCT endoscopic probe. To render 2D OCT datasets to true 3D anatomy, additional tools have to be applied, such as X-ray guidance and magnetic sensor (122, 126). X-ray increases ionizing radiation. Magnetic sensor either increases probe size (122) or requires an additional pull-back of the tracking sensor through the body cavity (126). In addition, the accuracy of magnetic tracking is potentially affected by the metal housing of the probe and the distance between the sensor and imaging window (122). In order to overcome these limitations, we present a pure-optical tracking method using a micro-beamsplitter. The accuracy of this tracking system was validated in a phantom test, and 3D imaging of a trachea by the beamsplitter probe is also demonstrated here.

9.2 Methods and materials

9.2.1 Probe design

Modified from a standard side-view probe design (127), we inserted a 90/10, 1.5 mm×1.5 mm beam splitter between the GRIN lens and the prism (Figure 45). By inserting the beamsplitter, the probe beam is divided into two sub-beams, probing two different positions in a longitudinal direction. Two signals corresponding to these two sub-beams that pass through different path length delays are obtained by an OCT detector simultaneously. The 90% light is used for imaging. The 10% light facilitates calculation of the probe inclination angle.

9.2.2 Dispersion compensation

The refractive index of optical components in the probe, especially the beamsplitter, slows down the light speed of certain optical frequencies to a greater extent more than others, therefore, disperses the light. The dispersion mismatch between the two arms of the OCT system can be compensated for by digitally canceling the frequency dependent nonlinear phase (33). In this design, we compensated for the dispersion of imaging light, the 90% light.
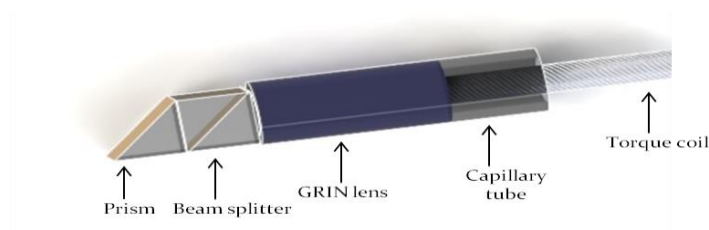
Figure 45 3D drawing of optical-tracking probe design.

9.2.3 Tracking algorithm

When using this probe to image a sample, we first insert this probe into a sheath with a straight gold-coating marker line, Figure 46 (a). After Fourier transform of the acquired signals from the OCT probe, the signals of the marker line obtained by two sub-beams are displayed at different depths, line A and line B, in the same image, Figure 46 (d). If there is no incline of the probe, the distance between line A and line B equals the optical path difference, D. In a situation where this probe inclines downward, the distance will be smaller than D, Figure 46 (c), and vice versa. By calculating the difference between the real distance in the image and D, we can deduce the inclination angle of probe at this time point by the following equations.

$$\theta = \arcsin(\frac{\Delta x - D}{D}) \qquad\qquad (9\text{-}1)$$

$$\text{Real } z = \cos(\theta)*\text{step} \qquad\qquad (9\text{-}2)$$

$$\text{Real } x = \sin(\theta)*\text{step} \qquad\qquad (9\text{-}3)$$

where θ is the inclination angle, Δx is the distance of between line A and line B, and step is the pullback distance between two frames.

By calculating the inclination angle of each frame across the image sequence, deducing the real x step and z step and connecting translational displacements of each step, we can obtain the motion trajectory of probe, Figure 47 (a).
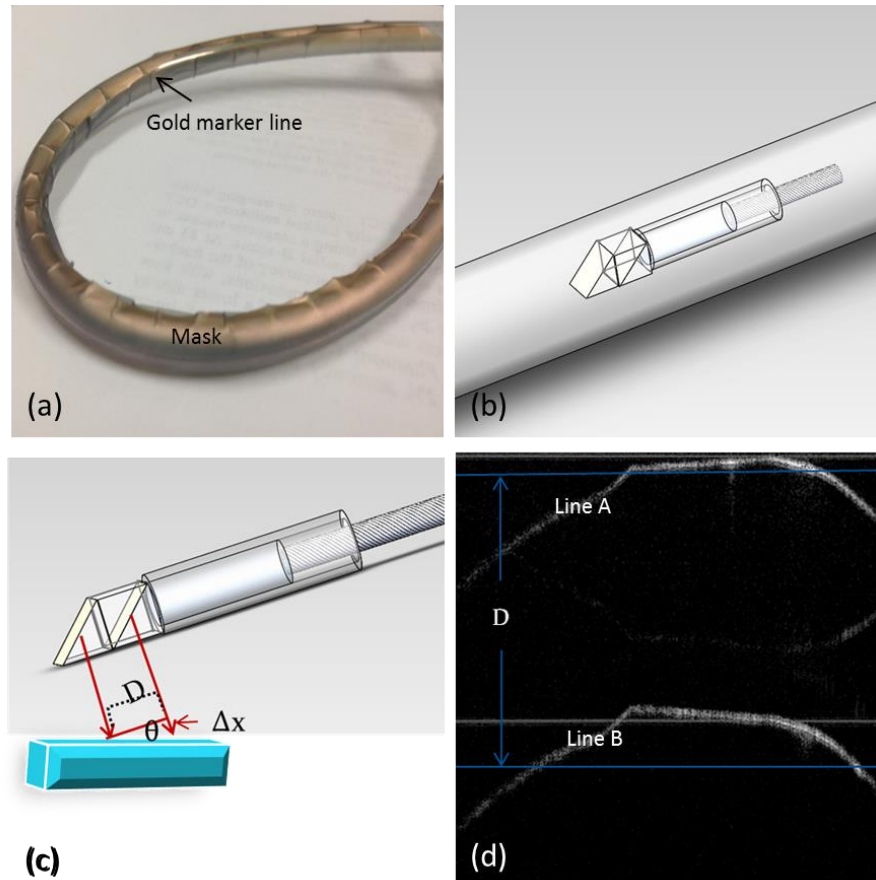
Figure 46 Principle of self-tracking probe (a) Photo showing how to make a gold marker line on Pebax sheath. (b) Schematic of probe inserted into Pebax sheath. (c) Schematic for quantification of the inclination angle. (d) Image obtained by the OCT system, when the probe inclined downward.

This method can be used in a situation where the probe is not only inclined in the X direction but also in the Y direction. That is to say, this method can also deduce the 3D trajectory of probe. To calculate x, y and z all three directions' steps, we coated two gold straight lines (90 degrees apart on the tube surface: one represents the x axis, the other, the y axis) on the surface of a Pebax tube to increase reflection in these two axes.

Similar to the inclined only in the X direction situation, inclination angles can be calculated by the flowing equation:

$$\alpha = \arctan(\frac{\Delta y}{D})$$

$$\beta = \arctan(\frac{\Delta x}{D})$$

(9-4)

Δy and Δx are calculated by the distance between the A line and B line in the marker lines 1 and 2, Figure 47 (c), which represents two different directions. The relationship between real x, real y, real z and Step is shown in Figure 47 (b). Thus,

$$realz = Step * \sin\alpha$$

$$realx = Step * \sin\beta$$

$$realy = \sqrt{step^2 - realx^2 - realz^2}$$

(9-5)

Similar to (9-2) and (9-3), by connecting 2D translational displacements of each step across the image sequence, we can obtain the motion 3D trajectory of probe.

9.2.4 Experiment validation

Experiments were performed to test the accuracy of tracking and capability of simultaneous tracking and imaging by this method. All images were obtained by the previously reported 1310 nm long range swept source OCT system (126). By applying masks on where gold is not needed, 8um gold was coated on to straight lines on the Pebax tube, Figure 46 (a). These two straight lines were used as markers for x and y axis tracking. These two gold marker lines were made for increasing reflection and thus increasing the returned signal for tracking. However, gold coating was not necessary since the usually returned signal from tube was strong enough for the tracking probe's motion.
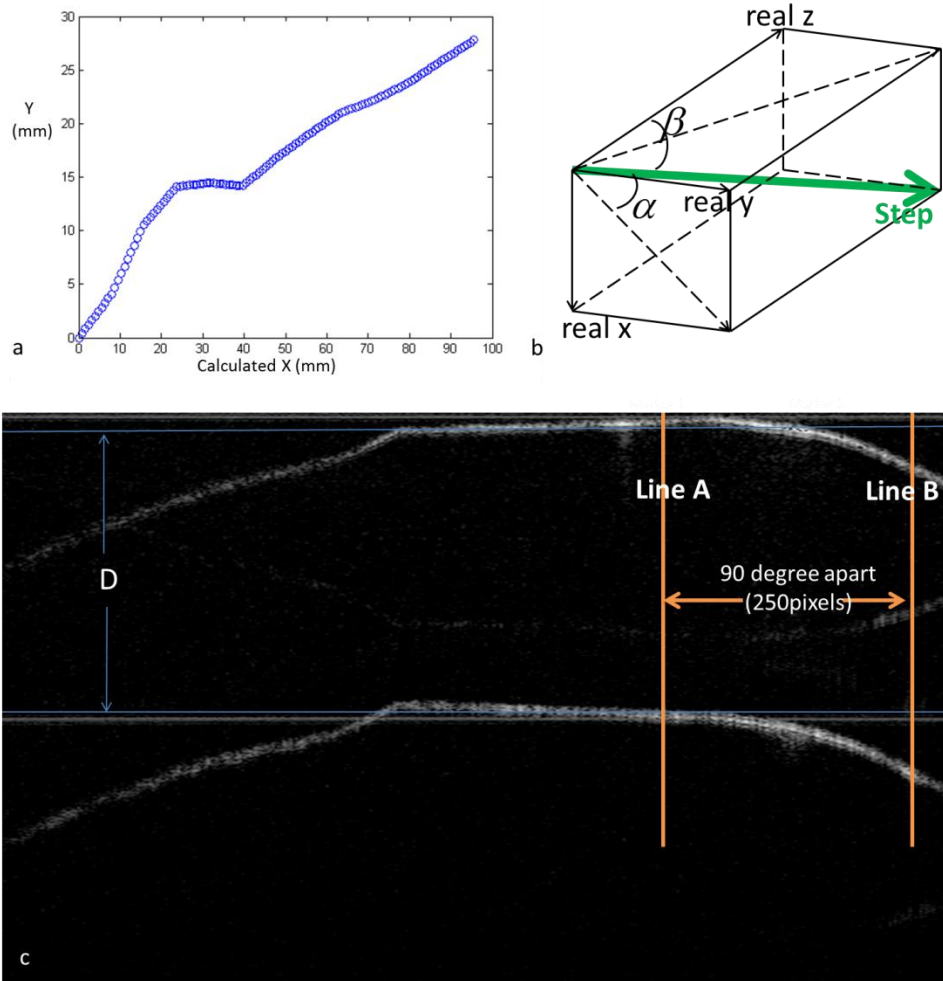
Figure 47 3D trajectory reconstruction. a) Example of reconstructed trajectory. b) Schematics showing the relationship between Δx, Δy, Δz and Step. c) Image for the processing 3D trajectory with 2 markers lines 90-degree apart.

9.3 Results

To measure the accuracy of this method, we first tested the 2D algorithm using a phantom tube.

Results are shown in Table 9. The root mean square (RMS) accuracy is 5.7 mm.

Table 9 Accuracy of trajectory detection by phantom

Angle	real X (mm)	calculated X (mm)	real Z (mm)	calculated Z (mm)	RMS error of x and z (mm)
Positive small	102.5	95.3	34.4	37.2	7.4
Positive big	75.9	73.9	27.0	28.1	2.2
Negative big	104.0	95.7	-24.7	-25.0	8.3
Negative mid	86.7	84.3	-33.4	-34.3	2.5
Negative small	96.0	87.7	-18.6	-19.8	8.3
Average error					5.7
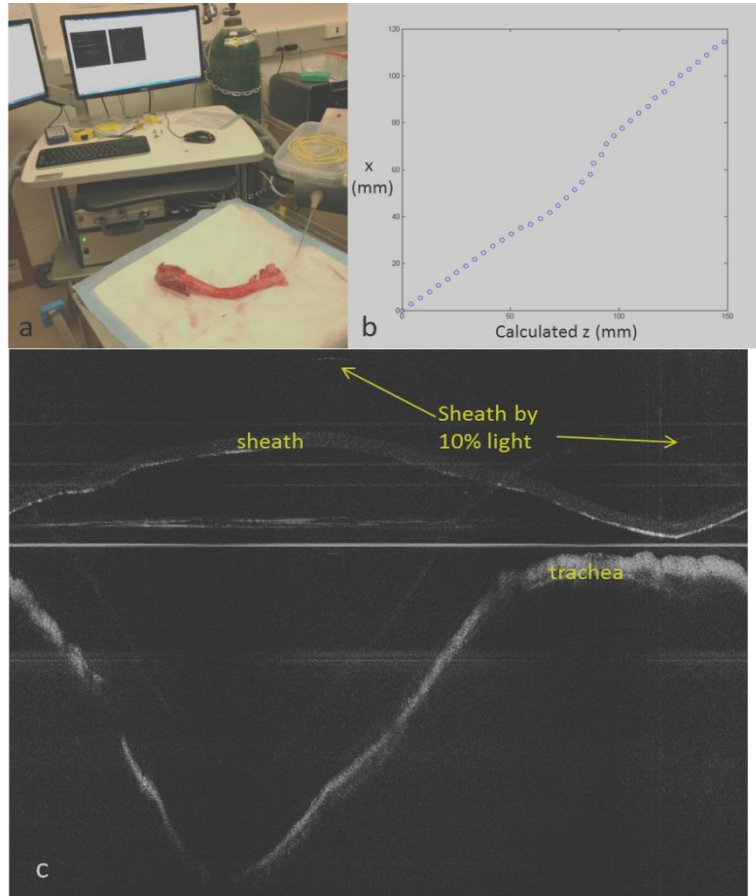
Figure 48 Image and reconstructed trajectory of ex vivo trachea model. a) Experimental setup for trachea imaging; b) Trajectory reconstruction result in this experiment; c) representative image of trachea indicate the sheath and the trachea locations.

To verify the ability of imaging sample and calculating trajectory at the same time, we imaged pig trachea using the beamsplitter probe. Representative images are shown in Figure 48 (c). The preset displacements of trachea from where the probe started imaging to where it ended imaging were 13.0 cm and 15.2 cm in the x and z axes, respectively. The calculated displacements of probe were 11.8 cm and 15.0 cm in the x and z axes, respectively. The reconstruction trajectory is shown in Figure 48 (b).

9.4 Future directions

By the proposed method, probe trajectory can be calculated. However, 3D reconstruction of lumen using the probe trajectory information is still under studied. We are collaborating with a team developing the 3D IVUS-Angio tool, which is a 3D structure reconstruction software. This software is designed for reconstruction of the artery using angiography and IVUS images. In our research, reconstruction of the airway can be achieved by inputting the probe trajectory images and OCT images, Figure 49.
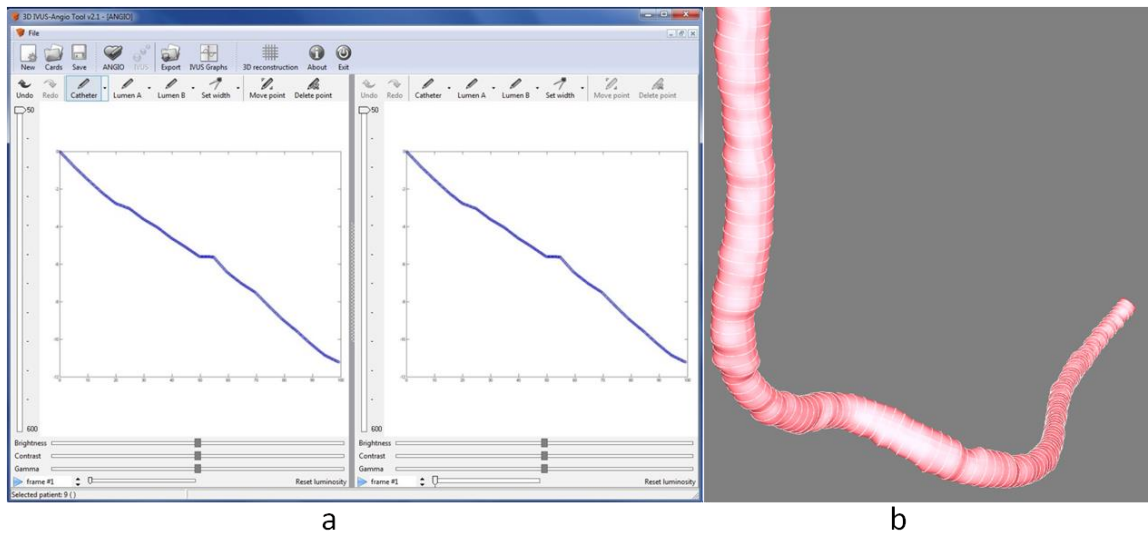
Figure 49 Future direction of self-tracking probe. a) The screenshot of inputting probe trajectory images into 3D IVUS Angio tool software; b) expected reconstruction by the software.

One limitation of our preliminary 2D validation experiment is that the probe may incline not only in the X direction which induces system errors in calculation. This is the main reason for the inaccuracy in calculation. This error will be eliminated after we fully develop the 3D algorithm and apply this modified algorithm.

Optical tracking is more cost-effective and its probe can be made smaller than magnetic tracking. This method can also be used for other optical catheter tracking. The optical company we collaborated with is able to provide 0.7 mm square beamsplitters, which makes the 1 mm outer diameter airway imaging probe possible. This size is safe enough for adult airway imaging with nasal insertion.

9.5 Summary

In summary, we presented a method to quantify a 3D OCT probe trajectory from inclination angles of the probe at each time point. These inclination angles are computed by serial images containing signals of the two split beams. With the guidance of two marker lines, 3D inclination angles can be determined and then used for 3D trajectory reconstruction. From conducted experiments on trajectory estimation at preset orientations, we calculated the accuracy of this method. Calculated trajectories were in good agreement with preset Pebax tube orientations. Trachea imaging demonstrated that the feasibility of using this method in an ex vivo animal test.

Chapter 10

Summary and future directions

10.1 Summary and discussion

Atherosclerotic plaque is susceptible to chronic occlusion or to acute disruption and subsequent complications which lead to death. Current clinical engineered efforts have been focused on improved vulnerable atherosclerotic plaque identification and characterization to aid risk stratification by developing improved diagnostic tools. Many novel imaging methods, such as OCT-molecular imaging, intravascular photoacoustic imaging, resonant acoustic radiation force optical coherence elastography, and laser speckle elastography (93, 128-131), are being developed and may provide new information for physicians regarding vulnerable plaque. Nevertheless, most of these imaging technologies have only been researched for a limited number of years and the clinical evidence proving that such image-derived vulnerable plaque is associated with an increased risk of ACS is still imperfect. In addition, other prospective investigations, including those that study long term outcomes, still need to be performed in a large sample of patients before such technology is widely accepted in clinical practice. The lack of clinical data, long term evaluation and standardized criteria is delaying the adoption of those technologies. However, there are a great number of clinical trials that have verified the effectiveness and promoted the wide use of IVUS and OCT technologies independently (132-134). The conclusions from these trails can be reasonably and logically generalized to an integrated IVUS-OCT technology and also direct its development. Thus, the integrated IVUS-OCT technology is likely to be a most currently accessible and trustworthy approach to provide

accurate identification of vulnerable plaque (19) in clinical practices to meet the burgeoning challenge of ACS morbidity and mortality in the current world.

This dissertation focuses on the development and use of an ultrafast integrated IVUS-OCT system to image and identify vulnerable atherosclerotic plaque in vivo. This integrated system uses a single fully integrated catheter and simultaneously provides real-time IVUS and OCT information. The full integration of two complementary techniques permits evaluation of coronary artery plaque burden, plaque types, the behavior of implanted coronary stents and a lot other traditionally inaccessible information.

A compact IVUS-OCT system and portable pull back console were developed, so as to be moved easily to hospitals. A novel miniature integrated probe which enables real-time co-registered IVUS-OCT imaging was designed and constructed. Catheters with a miniature imaging core and a sheath satisfying the strict requirements for routine clinical procedures were used in vivo in pig experiments. Recently, we further developed the system and made the imaging speed tripled (72 fps). This ultrafast system can significantly reduce the risk of integrated IVUS-OCT imaging and enable the translation of this technology into clinical practice.

In vivo imaging in rabbits and pigs were performed to validate the design of our imaging system and catheters. For the first time, this study shows that an integrated intracoronary IVUS-OCT system is feasible and safe to use in vivo to detect atherosclerotic plaques. Quantitatively evaluation of the diagnostic accuracy of the integrated system were also conducted. The in vivo animal imaging and ex vivo human cadaver diagnostic accuracy test elucidated that this ultrafast IVUS-OCT imaging system can facilitate a more powerful tool to explore the development of plaques and holds great hope for a more accurate assessment of vulnerable plaque in patients.

10.2 Future directions

10.2.1 Pig atherosclerotic model

We used a rabbit atherosclerotic model in our experiment to validate the ability of our system to image plaques in vivo. However, there are some drawbacks to this model: 1) the rabbit model only develop stable plaques but does not develop vulnerable plaques, which are what we intended to identify using the integrated IVUS-OCT system; 2) the development of this model requires feeding the rabbits a high-fat diet, and also involves a very complicated deendothelialization surgery with only a 60% survival rate; 3) a rabbit aorta is of a similar caliber to human coronary artery. However, it does not mimic the torturous path from a human aorta to a coronary artery. The sharp turns in this path is one of the biggest challenges, causing catheter breakage and drops in image quality. To overcome these limitations, a pig atherosclerotic model was researched and will be used in future. This animal model can develop plaques, and even vulnerable plaques, without any surgery or a high-fat diet.

The ExeGen MiniSwineTM LDLR Familial Hypercholesterolemic (FH) model is an ideal atherosclerosis animal model for intravascular imaging. Lesions formed in FH swine models have been shown to closely mimic advanced human atherosclerosis (135) and the ExeGen MiniSwineTM LDLR FH model has been demonstrated to develop atherosclerosis in a consistent and accelerated fashion in comparison to other models. ExeGen MiniSwineTM LDLR pigs weighing about 40-80 kg are available, and the size of the coronary artery is similar to that of a human coronary artery. Therefore, insight gained from intravascular imaging in the model can be translated to the intravascular imaging of human coronary arteries. The ExeGen MiniSwineTM LDLR model has been genetically engineered to contain a disruption of the pig's

endogenous LDLR gene, is available with heterozygous or homozygous disruptions, and the disruption of the LDL receptor has been shown to be inherited in an autosomal fashion. The advantage of using the ExeGen MiniSwineTM LDLR FH model is that it can develop consistent, severe atherosclerosis in a relatively short period of time without high-cholesterol feeding and this model is much less expensive to maintain than normocholesterolemic pigs fed a high-fat diet (136).

We will obtain the ExeGen MiniSwineTM LDLR FH model from Exemplar Genetics, LLC. The model will be purchased at 12 months of age. We will image one FH swine each month between the ages of 12 months and 18 months. We will perform continuous measurement (for full thickness of the cap, thickness of the fibrous cap outer layer, and tissue type determined from tissue strain value) using means and standard deviations.

10.2.2 Improvement of the manufacturing process and quality control of the ball lens

When making the ball lens by splicing an SMF28 and a coreless fiber, we first need to strip off the buffers of the SMF28 and coreless fiber. The stripped region of the fiber is very fragile. Our current solution is to strip as little as possible and then cover the stripped region with a polyimide tube. However, the area with the polyimide tube is not as flexible as it was before. To improve this current design, we could use a fiber recoater to recoat the fiber with a layer of buffer. This way, we can protect the stripped region of the SMF28. A recoater with manual injection enables us to control how much buffer will be recoated. With this function, we can stop the injection of the buffer solution when it gets closer to the ball, so as to recoat only the stripped fiber, but not the ball lens.

Currently, the polished surface of the ball lens has not been evaluated. This surface is not able to be evaluated by a traditional fiber tip microscope. A suitable product (inline video inspection

119

scope, Krell Tech, Morganville, NJ) is shown in Figure 50. This inline inspection scope can monitor the polished surface without disassembling the ball lens from the polisher, which avoids the damage caused by the extra disassembling steps.
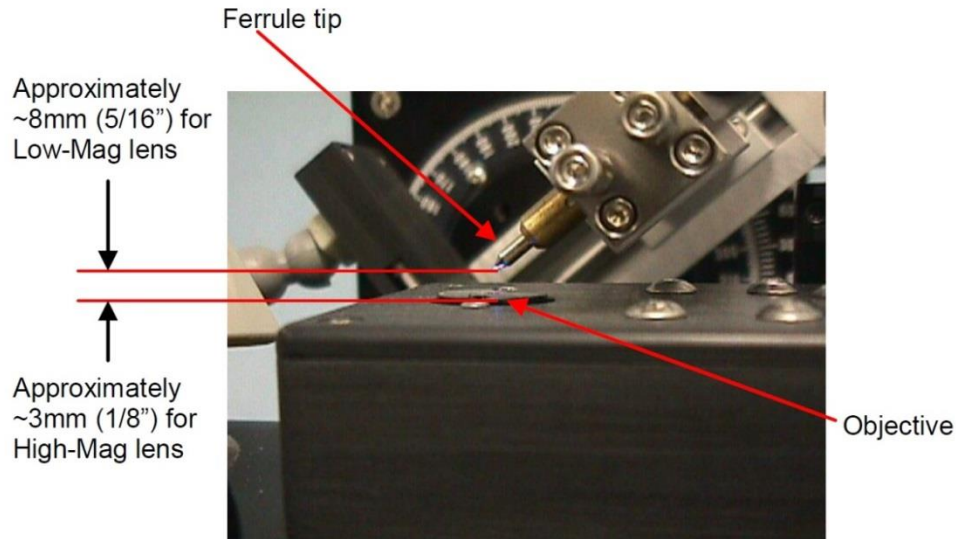
Figure 50 A photo of inline inspection scope to inspect the polished surface of ball lens.

10.2.3 FDA application and human studies

We have already submitted the Pre-IDE application and received feedback from the FDA Center for Devices and Radiological Health (CDRH). In accordance with their feedback, we may write the IDE application and submit it within 3 months of finishing the previously mentioned tests (see Chapter 6), and in vivo studies under good lab practice (GLP) standards. All documents of our bench tests and animal studies will be archived and retained for FDA application.

After the approval of FDA-IDE, we can start pilot human studies. A total of 30 participants will be asked to participate prior to receiving angiogram. Only patients who have consented to the study and need a stent placed in the coronary artery will take part in the study. Approximately 10

patents will participate in the research at UC Irvine. The clinical studies will provide a pathway to translating this technology from bench to bedside.

References

1. Jagat Narula, Strauss HW. The popcorn plaques. Nature Medicine. 2007;13:532-534.
2. Virmani R, Burke AP, Farb A, FD K. Pathology of the vulnerable plaque. J Am Coll Cardiol. 2006;47(8 suppl):C13-8.
3. Libby P. Current Concepts of the Pathogenesis of the Acute Coronary Syndromes. Circulation. 2001;104:365-372.
4. Javier Sanz, A.Fayad Z. Imaging of atherosclerotic cardivascular disease. Nature. 2008;45:953-957.
5. Matthias W. Lorenz, Hugh S. Markus, Michiel L. Bots, Maria Rosvall, Sitzer M. Prediction of Clinical Cardiovascular Events With Carotid Intima-Media Thickness. Circulation. 2007;115:459-467.
6. Greenland P BR, Brundage BH, Budoff MJ, Eisenberg MJ, Grundy SM, et al. clinical expert consensus document on coronary artery calcium scoring by computed tomography in global cardiovascular risk assessment and in evaluation of patients with chest pain: a report of the American College of Cardiology Foundation Clinical Expert Consensus Task Force. Circulation. 2007;115:402-426.
7. Rishi Puri, Matthew I. Worthley, Nicholls SJ. intravascular imaging of vulnerable coronary plaque: current and future concepts. Nature reviews. 2011;8:131-139.
8. Adrian F Low, Guillermo J Tearney, Brett E Bouma, Jang I-K. Technology Insight: optical coherence tomography—current status and future development. Nature clinical practice. 2006;3(3):154-162.
9. Thomas R. Porter, Thomas Sears, Feng Xie, Alan Michels, Jayne Mata, et al. Intravascular ultrasound study of angiographically mildly diseased coronary arteries. Journal of the American College of Cardiology. 1993;22(7):1858-1864.
10. Paul Schoenhagen, Khaled M Ziada, D.Geoffrey Vince, Steven E Nissen, E.Murat Tuzcu. Arterial remodeling and coronary artery disease: the concept of "dilated" versus "obstructive" coronary atherosclerosis. journal of the American College of Cardiology. 2001;38(2):297-306.
11. Sathyanarayana, S. C, S. L, W., Thomas L. Characterisation of atherosclerotic plaque by spectral similarity of radiofrequency intravascular ultrasound signals. . EuroIntervention. 2009;5:133-139.
12. Munenori Okubo, Masanori Kawasaki, Yoshiyuki Ishihara, Urara Takeyama, Shinji Yasuda, et al. Tissue Characterization of Coronary Plaques Comparison of Integrated Backscatter Intravascular Ultrasound With Virtual Histology Intravascular Ultrasound. Circulation Journal. 2008;72(10):1631-1639.
13. Anuja Nair, Barry D Kuban, Nancy Obuchowski, Vince DG. Assessing spectral algorithms to predict atherosclerotic plaque composition with normalized and raw intravascular ultrasound data. Ultrasound in Medicine & Biology. 2001;27(10):1319-1331.
14. Gastón A. Rodriguez-Granillo, Héctor M. García-García, Eugène P. Mc Fadden, Héctor M. García-García, Eugène P. Mc Fadden, et al. In Vivo Intravascular Ultrasound-Derived Thin-Cap Fibroatheroma Detection Using Ultrasound Radiofrequency Data Analysis. Journal of the American College of Cardiology. 2005;46(11):2038-2042.
15. Myeong-Ki Hong, Gary S. Mintz, Cheol Whan Lee, Jeong-Woo Lee, Jae-Hyoung Park, et al. A Three-Vessel Virtual Histology Intravascular Ultrasound Analysis of Frequency and

Distribution of Thin-Cap Fibroatheromas in Patients With Acute Coronary Syndrome or Stable Angina Pectoris The American Journal of Cardiology. 2008;101(5):568-572.

16. Troels Thim, Mette Kallestrup Hagensen, David Wallace-Bradley, Juan F. Granada, Greg L. Kaluza, et al. Unreliable Assessment of Necrotic Core by Virtual Histology Intravascular Ultrasound in Porcine Coronary Artery Disease. Circulation. 2010;3:384-391.

17. Guillermo J. Tearney, Ik-Kyung Jang, Bouma BE. Optical coherence tomography for imaging the vulnerable plaque. Journal of Biomedical Optics. 2006;11(2):021002.

18. Masanori Kawasaki, Brett E. Bouma, Jason Bressner, Stuart L. Houser, Seemantini K. Nadkarni, et al. Diagnostic Accuracy of Optical Coherence Tomography and Integrated Backscatter Intravascular Ultrasound Images for Tissue Characterization of Human Coronary Plaques Journal of the American College of Cardiology. 2006;48(1):81-88.

19. Takahiro Sawada, Junya Shite, Hector M. Garcia-Garcia, Toshiro Shinke, Satoshi Watanabe, et al. Feasibility of combined use of intravascular ultrasound radiofrequency data analysis and optical coherence tomography for detecting thin-cap fibroatheroma. European Heart Journal. 2008;29:1136-1146.

20. Fujii K, Hao H, Shibuya M, Imanaka T, Fukunaga M, Miki K, et al. Accuracy of OCT, Grayscale IVUS, and Their Combination for the Diagnosis of Coronary TCFA. JACC Cardiovasc Imaging. 2015;8(4):451-460.

21. Räber L, Heo JH, Radu MD, Garcia-Garcia HM, Stefanini GG, et al. Offline fusion of co-registered intravascular ultrasound and frequency domain optical coherence tomography images for the analysis of human atherosclerotic plaques. EuroIntervention. 2012;8(1):98-108.

22. Yingli Wang YL, Kuanhong Xu. Signal processing for sidelobe suppression in optical coherence tomography images. J Opt Soc Am A. 2010;27(3):415-421.

23. Linbo Liu JAG, Seemantini K Nadkarni, Jimmy D Toussaint, Yukako Yagi, et al. Imaging the subcellular structure of human coronary atherosclerosis using micro–optical coherence tomography. Nature Medicine. 2011;17.

24. Jing Xu KW, Yifan Jian, and Marinko V. Sarunic. Real-time acquisition and display of flow contrast using speckle variance optical coherence tomography in a graphics processing unit. Journal of Biomedical Optics. 2014;19(2):026001.

25. Alexander Wong AM, Kostadinka Bizheva, David A. Clausi. General Bayesian estimation for speckle noise reduction in optical coherence tomography retinal imagery. Optics Express. 2010;18(8):8338-8352.

26. Zhongping Jian LY, Bin Rao, Bruce J. Tromberg, Zhongping Chen. Three-dimensional speckle suppression in optical coherence tomography based on the curvelet transform. Optics Express. 2010;18(2):1024-1032.

27. Zhongping Jian ZY, Lingfeng Yu, Bin Rao, Zhongping Chen, Bruce J. Tromberg. Speckle attenuation in optical coherence tomography by curvelet shrinkage. Optics Letters. 2009;34(10):1516-1518.

28. Tsung-Han Tsai BP, Yuankai K. Tao, Vijaysekhar Jayaraman, James Jiang, Peter J. S. Heim, et al. Ultrahigh speed endoscopic optical coherence tomography using micromotor imaging catheter and VCSEL technology. Biomedical Optics Express 2013;4(7):1119.

29. R. Huber MW, J. G. Fujimoto. Fourier Domain Mode Locking (FDML): A new laser operating regime and applications for optical coherence tomography. Optics Express. 2006;14(8):3225-3237.

30. R. Huber MW, K. Taira, K. Hsu, J. G. Fujimoto. Amplified, frequency swept lasers for frequency domain reflectometry and OCT imaging: design and scaling principles. Optics Express. 2005;13(9):3513-3528.

31. WooJhon Choi BP, Vijaysekhar Jayaraman, Bernhard Baumann, Ireneusz Grulkowski, Jonathan J. Liu, et al. Phase-sensitive swept source OCT imaging of the human retina with a VCSEL light source. Optics Letters. 2013;38(13):338-340.

32. Zhihua Ding YZ, Hongwu Ren, J. Nelson, Zhongping Chen. Real-time phase-resolved optical coherence tomography and optical Doppler tomography. Optics Express. 2002;10(5):236-245.

33. Maciej Wojtkowski VS, Tony Ko, James Fujimoto, Andrzej Kowalczyk, Jay Duker. Ultrahigh-resolution, high-speed, Fourier domain optical coherence tomography and methods for dispersion compensation. Optics Express. 2004;12(11):2404-2422.

34. Rollins ZHaAM. Fourier domain optical coherence tomography with a linear-in-wavenumber spectrometer. OPTICS LETTERS. 2007;32(24):3525-3527.

35. V. M. Gelikonov GVG, P. A. Shilyagin. Linear-Wavenumber Spectrometer for High-Speed Spectral-Domain Optical Coherence Tomography. GEOMETRICAL AND APPLIED OPTICS. 2009;106(3):459-465.

36. Sang-Won Lee H-WJ, Yeh-Chan Ahn, Woonggyu Jung, Zhongping Chen,Beop-Min Kima. Axial resolution and depth range of high-resolution spectral domain optical coherence tomography at 1.3 μm. Proc of SPIE. 2009;7168:71682L.

37. Jiechen Yin, Hao-Chung Yang, Xiang Li, Jun Zhang, Qifa Zhou, et al. Integrated intravascular optical coherence tomography ultrasound imaging system Journal of biomedical optics. 2010;15(1):010512.

38. Jiechen Yin, Xiang Li, Joe Jing, Jiawen Li, David Mukai, et al. Novel combined miniature optical coherence tomography ultrasound probe for in vivo intravascular imaging. Journal of biomedical optics. 2011;16(6):060505.

39. Xiang Li, Jiechen Yin, Changhong Hu, Qifa Zhou, K. Kirk Shung, Chen Z. High-resolution coregistered intravascular imaging with integrated ultrasound and optical coherence tomography probe. Applied Physics Letters. 2010;97(13):133702.

40. Brian H. Li, Annie S.O. Leung, Alan Soong, Chelsea E. Munding, Hyunggyun Lee, et al. Hybrid intravascular ultrasound and optical coherence tomography catheter for imaging of coronary atherosclerosis. Catheterization and Cardiovascular Interventions. 2013.

41. McCullough PA. Contrast-Induced Acute Kidney Injury. Journal of the American College of Cardiology. 2008;51(15):1419-1428.

42. Xiang Li, Jiawen Li, Joe Jing, Teng Ma, Shanshan Liang, et al. Integrated IVUS-OCT Imaging for Atherosclerotic Plaque Characterization. IEEE Journal of Selected Topics in Quantum Electronics. 2014;20(2):1-8.

43. Youxin Mao SC, Costel Flueraru. Fiber lenses for ultra-small probes used in optical coherent tomography. J Biomedical Science and Engineering. 2010;3:27-34.

44. R. Andrew Wall GTB, Jennifer K. Barton. Novel focused OCT-LIF endoscope. Biomed Opt Express. 2011;2(3):421-430.

45. Van Soest G BJ, van der Steen AF. Azimuthal registration of image sequences affected by nonuniform rotation distortion. 12. 2008;3:348-354.

46. Jiawen Li, Teng Ma, Joseph Jing, Jun Zhang, Pranav M. Patel, et al. Miniature optical coherence tomography-ultrasound probe for automatically coregistered three-dimensional intracoronary imaging with real-time display. J Biomed Opt 2013;18(10):100502.

47. Jiawen Li, Xiang Li, Dilbahar Mohar, Aidan Raney, Joseph Jing, Jet al. Integrated IVUS-OCT for Real-Time Imaging of Coronary Atherosclerosis. JACC cardiovascular imaging. 2014;7(1):102.

48. Jiawen Li, Teng Ma, Dilbahar Mohar, Adrian Correa, Hataka Minami, et al. Diagnostic accuracy of integrated intravascular ultrasound and optical coherence tomography (IVUS-OCT) system for coronary plaque characterization. Proc SPIE 8926, Photonic Therapeutics and Diagnostics X, 892635. 2014.

49. Eric M. Strohm, Kolios MC. Sound velocity and attenuation measurements of perfluorocarbon liquids using photoacoustic methods. IEEE International Ultrasonics Symposium Proceedings. 2011:2368-2371.

50. Hiram G. Bezerra, Marco A. Costa, Giulio Guagliumi, Andrew M. Rollins, Simon DI. Intracoronary Optical Coherence Tomography: A Comprehensive Review: Clinical and Research Applications. J Am Coll Cardiol Intv. 2009;2(11):1035-1046.

51. Dawson P. Cardiovascular effects of contrast agents. The American Journal of Cardiology. 1989;64(9):E2-E9.

52. Ron Waksman, Hironori Kitabata, Francesco Prati, Mario Albertucci, Mintz GS. Intravascular Ultrasound Versus Optical Coherence Tomography Guidance. Journal of the American College of Cardiology. 2013;62(17):S32-40.

53. M. Brezinski, K. Saunders, C. Jesser, X. Li, Fujimoto J. Index Matching to Improve Optical Coherence Tomography Imaging Through Blood Circulation. 2001:103.

54. Ozaki Y, Kitabata H, Tsujioka H, Hosokawa S, Kashiwagi M, et al. Comparison of contrast media and low-molecular-weight dextran for frequency-domain optical coherence tomography. Circulation journal. 2012;76(4):922-927.

55. Hoang KC, Edris A, Su J, Mukai DS, Mahon S, et al. Use of an oxygen-carrying blood substitute to improve intravascular optical coherence tomography imaging. Journal of Biomedical Optics. 2009;14(3):034028.

56. X. Xu, R. K. Wang, J. B. Elder, Tuchin VV. Effect of dextran-induced changes in refractive index and aggregation on optical properties of whole blood. PHYSICS IN MEDICINE AND BIOLOGY. 2003;48:1205-1221.

57. Henkel-Honke T, M. O. Artificial Oxygen Carriers: A current review. American Association of Nurse Anesthetists. 2007;75(3):205-211.

58. Thomson K, Varma D. Safe use of radiographic contrast media. Australian Prescriber. 2010;33:19-22.

59. Tuchin VV, Xu X, RK. W. Dynamic optical coherence tomography in studies of optical clearing, sedimentation, and aggregation of immersed blood. Applied Optics. 2002;14(1):258-71.

60. Tuchin VV. Optical clearing of tissues and blood using the immersion method. Journal of Physics D: Applied Physics. 2005;38(15):2497.

61. Bouma BE, Tearney GJ, Yabushita H, Shishkov M, Kauffman CR, et al. Evaluation of intracoronary stenting by intravascular optical coherence tomography. Heart. 2003;89(3):317-320.

62. Xu X, Yu L, Z C. Optical clearing of flowing blood using dextrans with spectral domain optical coherence tomography. Journal of Biomedical Optics. 2008;13(2):021107.

63. Loftsson T. Phusocochemical Properties and Pharmacokinetics. Essential Pharmacokinetics: A Primer for Pharmaceutical Scientists: Academic Press; 2015. p. 101.

64. Nieves Gonzalo, Guillermo J. Tearney, Patrick W. Serruys, Gijs van Soest, Takayuki Okamura, et al. Second-Generation Optical Coherence Tomography in Clinical Practice. High-Speed Data Acquisition Is Highly Reproducible in Patients Undergoing Percutaneous Coronary Intervention. Rev Esp Cardiol. 2010;63:893-903.

65. R. K. Wang, Tuchin VV. Optical coherence tomography. Light scattering and imaging enhancement. In: Tuchin VV, editor. Coherent-Domain Optical Methods: Biomedical Diagnostics, Environmental Monitoring and Material Science 2: Springer-Verlag; 2013. p. 665-742.

66. Hoang KC, EA, Su J, Mukai DS, Mahon S, et al. Use of an oxygen-carrying blood substitute to improve intravascular optical coherence tomography imaging. J Biomed Opt. 2009;14(3):034028.

67. Treeby BE, Zhang EZ, Thomas AS, BT. C. Measurement of the Ultrasound Attenuation and Dispersion in Whole Human Blood and its Components from 0-70 MHz. Ultrasound in Medicine & Biology. 2011;3(7):289-300.

68. Y.-H. Zhang, Y.-F. Hu, Zhang Z-X. Viscosity and Density of the Nonelectrolyte System Mannitol + Sorbitol + Sucrose + H_2O and Its Binary and Ternary Subsystems at 298.15K. J Chem Eng Data. 2006;51:438-442.

69. A.N. Bashkatov, E.A. Genina, Y.P. Sinichkin, V.I. Kochubuey, N.A. Lakodina, Tuchin VV. Glucose and mannitol diffusion in human dura mater. Biophysical Journal. 2003;85(5):3310-3318.

70. A. J. Tatham, Prydal J. Do Non-Ionic Contrast Media Temporarily Improve Corneal Transparency?. J Ophthalmic Vis Res. 2013;8(4).

71. Cinar Y, Senyol AM, K. D. Blood viscosity and blood pressure: role of temperature and hyperglycemia. Am J Hypertens. 2001;14:433-438.

72. Késmárky G, Kenyeres P, Rábai M, K. T. Plasma viscosity: a forgotten variable. Clin Hemorheol Microcirc. 2008;39(1-4):243-246.

73. O. Sydoruk, O.Zhernovaya, V. Tuchin, Douplik A. Refractive index of solutions of human hemoglobin from the near-infrared to the ultraviolet range: Kramers-Kronig analysis. Journal of Biomedical Optics. 2012;17(11):115002-1-6.

74. D.H. Tycko, M.H. Metz, E.A. Epstein, Grinbaum A. Flow-cytometric light scattering measurement of red blood cell volume and hemoglobin concentration. Applied Optics. 1985;24(9):1355-1365.

75. Y. Park, M. Diez-Silva, G. Popescu, G. Lykotrafitis, W. Choi, et al. Refractive index maps and membrane dynamics of human red blood cells parasitized by Plasmodium falciparum. PNAS. 2008;105(37):13730-5.

76. Lin Chen, Steven Revel, Kyle Morris, David G. Spiller, Louise C. Serpell, Adams DJ. Low Molecular Weight Gelator – Dextran Composites. Chemical Communication. 2010;36.

77. C.F. Snyder, H.S. Isbell, M.R. Dryden, Holt NB. Optical rotations, refractive indices, and densities of dextran solutions. Journal of Research of the National Bureau of Standards. 1954;53(3):131-137.

78. Stokes GG. On the theories of the internal friction in fluids in motion, and of the equilibrium and motion of elastic solids. Transactions of the Cambridge Philosophical Society. 1849;8(22):287-342.

79. H. Schmid-Schönbein, P. Gaehtgens, Hirsch H. On the shear rate dependence of red cell aggregation in vitro. J Clin Invest 1968;47(6):1447–1454.

80. Wang LV. Photoacoustic Imaging and Spectroscopy: CRC press; 2009.

81. Yeager D, Karpiouk A, Wang B, Amirian J, Sokolov K, et al. Intravascular photoacoustic imaging of exogenously labeled atherosclerotic plaque through luminal blood. J Biomed Opt. 2012;17(10):106016.
82. Y. Zhou, J. Yao, Wang LV. Optical clearing-aided photoacoustic microscopy with enhanced resolution and imaging depth. Opt Lett. 2013;38(14):2592-2595.
83. Y. Liu, X. Yang, D. Zhu, R. Shi, Luo Q. Optical clearing agents improve photoacoustic imaging in the optical diffusive regime. Opt Lett. 2013;38(20):4236-4239.
84. Yulian A. Menyaev, Dmitry A. Nedosekin, Mustafa Sarimollaoglu, Mazen A. Juratli, Ekaterina I. Galanzha, et al. Skin optical clearing for in vivo photoacoustic flow cytometry. Biomedical Opt Express. 2013;4(12):3030-3041.
85. Shigemitsu Tanaka KS, Ryotaro Yamada, Kaori Nakagawa, Paul G Yock, Peter J Fitzgerald, et al. plaque assessment with a novel high-definition 60-MHz IVUS imaging system: comparison with conventinal 40MHz IVUS and Optical coherence tomography. J Am Coll Cardiol 2013;61(10_S):61878.
86. Yuhei Kobayashi HK, Shigemitsu Tanaka, Kaori Nakagawa, Kozo Okada, Kyuhachi Otagiri, et al. Precision of a Novel High-Definition 60MHz IVUS in Quantitative Measurement: Comparison with Conventional 40MHz IVUS and Optical Coherence Tomography. J Am Coll Cardiol. 2014;64(11_S).
87. Teng Ma, Mingyue Yu, Jiawen Li, Munding CE, Zeyu Chen, et al. Multi-frequency intravascular ultrasound (IVUS) imaging. IEEE Transactions on Ultrasonics, Ferroelectrics, and Frequency Control. 2015;62(1):97-107.
88. V.V. Tuchin, D.M. Zhestkov, A.N. Bashkatov, Genina EA. Theoretical Study of Immersion Optical Clearing of Blood in Vessels at Local Hemolysis. Optics Express 2004;12:2966-2971.
89. Olga Zhernovaya, Valery V. Tuchin, Leahy MJ. Blood optical clearing studied by optical coherence tomography. J Biomed Opt 2013;18(2):026014-1-8.
90. G. Popescu, T. Ikeda, C. Best, K. Badizadegan, R. R. Dasari, Feld MS. J. Biomed. Opt. . Erythrocyte structure and dynamics quantified by Hilbert phase microscopy. 2005;10(6):060503-1-3
91. Katsuichi Ohtsuki MH, Koichi Akashi, Susan Kopiwoda, H. William Strauss. Detection of Monocyte Chemoattractant Protein-1 Receptor Expression in Experimental Atherosclerotic Lesions An Autoradiographic Study. Circulation. 2001;104:203-208.
92. Frank D. Kolodgie AP, Renu Virmani, Navneet Narula, Johan W. Verjans,Deena K. Weber, et al. Targeting of Apoptotic Macrophages and Experimental Atheroma With Radiolabeled Annexin V. Circulation. 2003;108:3134-3139.
93. Hongki Yoo, Jin Won Kim, Milen Shishkov, Eman Namati, Theodore Morse, et al. Intra-arterial catheter for simultaneous microstructural and molecular imaging in vivo. Nature Medicine. 2011;17:1680-1684.
94. Francesco Prati, Giulio Guagliumi, Gary S. Mintz, Marco Costa , Evelyn Regar, et al. Expert review document on methodology, terminology and clinical applications of optical coherence tomography for the assessment of interventional procedures. Eur Heart J. 2012;33(20):2513-20.
95. Tjeerd J. Römer, James F. Brennan III, Gerwin J. Puppels, Aailko H. Zwinderman, Sjoerd G. van Duinen, et al. Intravascular Ultrasound Combined With Raman Spectroscopy to Localize and Quantify Cholesterol and Calcium Salts in Atherosclerotic Coronary Arteries. Arteriosclerosis, Thrombosis, and Vascular Biology. 2000;20:478-483.

96. Narula J, Garg P, Achenbach S, Motoyama S, Virmani R, HW. S. Arithmetic of vulnerable plaques for noninvasive imaging. Nature Clinical Practice Cardiovasc Med. 2008;5 S2-10.

97. Rieber J, Meissner O, Babaryka G, Reim S, Oswald M, et al. Diagnostic accuracy of optical coherence tomography and intravascular ultrasound for the detection and characterization of atherosclerotic plaque composition in ex-vivo coronary specimens: a comparison with histology. Diagnostic Methods. 2006;17(5):425-430.

98. Kume T AT, Kawamoto T, Watanabe N, Toyota E, Neishi Y, et al. Assessment of coronary arterial plaque by optical coherence tomography. Am J Cardiol. 2006;97(8):1172-1175.

99. Kawasaki M BB, Bressner J, Houser SL, Nadkarni SK, MacNeill BD, et al. Diagnostic accuracy of optical coherence tomography and integrated backscatter intravascular ultrasound images for tissue characterization of human coronary plaques. J Am Coll Cardiol. 2006;48(1):81-88.

100. Hiroshi Yabushita, Brett E. Bouma, Stuart L. Houser, H. Thomas Aretz, Ik-Kyung Jang, et al. Characterization of Human Atherosclerosis by Optical Coherence Tomography. Circulation. 2002;106:1640-1645.

101. Gary S Mintz SEN, William D Anderson, Steven R Bailey, Raimund Erbel, Peter J Fitzgerald, et al. American College of Cardiology clinical expert consensus document on standards for acquisition, measurement and reporting of intravascular ultrasound studies (ivus). A report of the american college of cardiology task force on clinical expert consensus documents developed in collaboration with the european society of cardiology endorsed by the society of cardiac angiography and interventions. J Am Coll Cardiol. 2001;37(5):1478-1492.

102. Jang IK, Bouma BE, Kang DH, Park SJ, Park SW, et al. Visualization of coronary atherosclerotic plaques in patients using optical coherence tomography: comparison with intravascular ultrasound. J Am Coll Cardiol. 2002;39(4):604-9. PubMed PMID: 11849858.

103. Ron Waksman HK, Francesco Prati, Mario Albertucci, Gary S. Mintz. Intravascular Ultrasound Versus Optical Coherence Tomography Guidance. Journal of the American College of Cardiology. 2013;62(17 suppl S):S32-S40.

104. Prati F DVL, Biondi-Zoccai G, Occhipinti M, La Manna A, Tamburino C, et al. Angiography alone versus angiography plus optical coherence tomography to guide decision-making during percutaneous coronary intervention: the Centro per la Lotta contro l'Infarto-Optimisation of Percutaneous Coronary Intervention (CLI-OPCI) study. EuroIntervention. 2012;8(7):823-829.

105. Masamichi Takano SI, Ik-Kyung Jang, Masanori Yamamoto, Daisuke Murakami, Koji Seimiya, Takayoshi Ohba. Evaluation by Optical Coherence Tomography of Neointimal Coverage of Sirolimus-Eluting Stent Three Months After Implantation. The American Journal of Cardiology. 2007;99(8):1033-1038.

106. Yoriyasu Suzuki FI, Tomomi Koizumi, Fermin Tio, Alan C. Yeung MD, Paul G. Yock, et al. In Vivo Comparison Between Optical Coherence Tomography and Intravascular Ultrasound for Detecting Small Degrees of In-Stent Neointima After Stent Implantation. JACC. 2008;1(2):168-173.

107. Bouma BE TG, Yabushita H, Shishkov M, Kauffman CR, DeJoseph Gauthier D, et al. Evaluation of intracoronary stenting by intravascular optical coherence tomography. Heart. 2003;89(3):317-320.

108. Fitzgerald YHaPJ. Frontiers in Intravascular Imaging Technologies. Circulation. 2008;117:2024-2037.

109. Domagk D PC, Dietl KH, Senninger N, Heinecke A, Domschke W, Menzel J. Endoscopic transpapillary biopsies and intraductal ultrasonography in the diagnostics of bile duct strictures: a prospective study. Gut. 2002;51(2):240-244.

110. Domagk D WJ, Reimer P, Hertel L, Poremba C, Senninger N, et al. Endoscopic retrograde cholangiopancreatography, intraductal ultrasonography, and magnetic resonance cholangiopancreatography in bile duct strictures: a prospective comparison of imaging diagnostics with histopathological correlation. Am J Gastroenterol. 2004;99(9):1684-9.

111. Seitz. U. FJ, Jaeckle. S., Feldchtein. F., Bohnacker. S., Thonke. F., et al. First in vivo optical coherence tomography in the human bile duct. Endoscopy. 2001;33:1018-1021.

112. Poneros J.M. TGJ, Shiskov M., Kelsey P.B., Lauwers G.Y., et al. Optical coherence tomography of the biliary tree during ercp. Gastrointest Endoscop. 2002;55:84-88.

113. B. J. Vakoc SHY, G. J. Tearney, B. E. Bouma. Elimination of depth degeneracy in optical frequency-domain imaging through polarization-based optical demodulation. Optics Letters. 2006;31(3):362-364.

114. Jun Zhang WJ, J. Stuart Nelson, Zhongping Chen. Full range polarization-sensitive Fourier domain optical coherence tomography. Optics Express. 2004;12(24):6033-6039.

115. Tsung-Han Tsai JGFaHM. Endoscopic Optical Coherence Tomography for Clinical Gastroenterology. diagnostics. 2014;4:57-93.

116. Pier Alberto Testoni BM, Alberto Mariani. Optical Coherence Tomography for Investigation of the Pancreatico-Biliary System: Still Experimental? JOP J Pancreas. 2007;8(2):156-165.

117. M. Wojtkowski AK, R. Leitgeb, A. F. Fercher. Full range complex spectral optical coherence tomography technique in eye imaging. Optics Letters. 2002;27(16):1415-1417

118. Michael R. Hee CAP, Jay S. Duker, Elias Reichel, Jeffrey G. Coker, Jason R. Wilkins, et al. Topography of diabetic macular edema with optical coherence tomography Ophthalmology. 1998;105(2):360-370.

119. Welzel J. Optical coherence tomography in dermatology: a review. Skin Research and Technology. 2001;7(1):1-9.

120. Yonghua Zhao ZC, Christopher Saxer, Shaohua Xiang, Johannes F. de Boer, J. Stuart Nelson. Phase-resolved optical coherence tomography and optical Doppler tomography for imaging blood flow in human skin with fast scanning speed and high velocity sensitivity. Optics Letters. 2000;25(2):114-116.

121. Seok H Yun GJT, Benjamin J Vakoc, Milen Shishkov, Wang Y Oh, Adrien E Desjardins, et al. Comprehensive volumetric optical microscopy in vivo. Nature Medcine. 2006;12(12):1429-1433.

122. Brandon Lau RAM, Andrea Curatolo, Rodney W. Kirk, Derek K. Gerstmann, David D. Sampson. Imaging true 3D endoscopic anatomy by incorporating magnetic tracking with optical coherence tomography: proof-of-principle for airways. Optics Express. 2010;18(26):27173-27180.

123. Jennifer Walsh MSL, Alexander Paduch, Kathleen Maddison, Danielle Philippee, Julian Armstrong, et al. Evaluation of pharyngeal shape and size using anatomical optical coherence tomography in individuals with and without obstructive sleep apnoea. Journal of Sleep Research. 2008;17(2):230-238.

124. Christian Wengert PC, John M. Du Charles Baur, Gabor Szekely. Markerless Endoscopic Registration and Referencing. Med Image Comput Comput Assist Interv. 2006;9(Pt 1):816-823.

125. Kensaku Mori DD, Jun-ichi Hasegawa, Yasuhito Suenaga, Jun-ichiro Toriwaki, Hirotsugu Takabatake, Hiroshi Natori. A Method for Tracking the Camera Motion of Real Endoscope by Epipolar Geometry Analysis and Virtual Endoscopy System. Medical Image Computing and Computer-Assisted Intervention. 2001;Lecture Notes in Computer Science Volume 2208:1-8.
126. Joseph Jing JZ, Anthony Chin Loy, Brian J. F. Wong, Zhongping Chen. High-speed upper-airway imaging using full-range optical coherence tomography. Journal of Biomedical Optics. 2012;17(11):110507.
127. Guillermo J. Tearney MEB, Brett E. Bouma, Stephen A. Boppart, Costas Pitris, James F. Southern, James G. Fujimoto. In Vivo Endoscopic Optical Biopsy with Optical Coherence Tomography. Science. 1997;276:2037-2039.
128. Hajjarian Z XJ, Jaffer FA, Tearney GJ, Nadkarni SK. Intravascular laser speckle imaging catheter for the mechanical evaluation of the arterial wall. Journal of Biomedical Optics. 2011;16(2):026005.
129. Christine P. Fleming JE, Elkan F. Halpern, Joseph A. Gardecki, Guillermo J. Tearney. Depth resolved detection of lipid using spectroscopic optical coherence tomography. Biomedical Optics Express. 2013;4(8):1269-1284.
130. Wenjuan Qi RL, Teng Ma, Jiawen Li, Kirk Shung, Qifa Zhou, Zhongping Chen. Resonant Acoustic Radiation Force Optical Coherence Elastography. Applied Physics Letters. 2013;103(10).
131. Krista Jansen, GvS, Antonius F.W. van der Steen. Intravascular Photoacoustic Imaging: A New Tool for Vulnerable Plaque Identification. Ultrasound in Medicine & Biology. 2014;40(6):1037-1048.
132. Jia H AF, Aguirre AD, Lee S, Chia S, Lowe H, et al. In vivo diagnosis of plaque erosion and calcified nodule in patients with acute coronary syndrome by intravascular optical coherence tomography. Journal of the American College of Cardiology. 2013;62(19):1748-1758.
133. Uemura S IK, Soeda T, Okayama S, Sung JH, Nakagawa H, et al. Thin-cap fibroatheroma and microchannel findings in optical coherence tomography correlate with subsequent progression of coronary atheromatous plaques. European Heart Journal. 2012;33(1):78-85.
134. Gregg W. Stone AM, Alexandra J. Lansky, Bernard de Bruyne, Ecaterina Cristea, Gary S. Mintz, et al. A Prospective Natural-History Study of Coronary Atherosclerosis. The New England Journal of Medicine. 2011;364:226-235.
135. Prescott MF H-RJ, von Linden-Reed J, Rapacz J. Familial hypercholesterolemia associated with coronary atherosclerosis in swine bearing different alleles for apolipoprotein B. Annals of the New York Academy of Sciences. 1995.
136. Dwight A. Bellinger EPM, Timothy C. Nichols. Swine Models of Type 2 Diabetes Mellitus: Insulin Resistance, Glucose Tolerance, and Cardiovascular Complications. Institute of laboratory Animal research. 2006;47(3):243-258.